Université
de Montréal

Conventional and Reciprocal Approaches to the Forward and Inverse Problems of Electroencephalography

by

Stefan FINKE

Institut de génie biomédical

Faculté de médecine

A thesis submitted in partial fulfillment of the requirements for the degree of
Doctor of Philosophy in the Faculty of Graduate Studies
(Biomedical Engineering)

March, 2012

Université de Montréal
Faculté des études supérieures et postdoctorales

Cette thèse intitulée :

L'approche conventionnelle et réciproque aux problèmes direct et inverse de l'électroencéphalographie

présenté par :
Stefan FINKE

a été évalué par un jury composé des personnes suivantes :

Frédéric LESAGE, président-rapporteur
Ramesh M. GULRAJANI, directeur de recherche[1]
Pierre SAVARD, directeur de recherche
Jean GOTMAN, codirecteur
Vincent JACQUEMET, membre du jury
André ACHIM, examinateur externe

---

[1] Décédé

Abstract

The inverse problem of electroencephalography (EEG) is the localization of current sources within the brain using surface potentials on the scalp generated by these sources. An inverse solution typically involves multiple calculations of scalp surface potentials, i.e., the EEG forward problem. To solve the forward problem, models are needed for both the underlying source configuration, the source model, and the surrounding tissues, the head model. This thesis treats two distinct approaches for the resolution of the EEG forward and inverse problems using the boundary-element method (BEM): the conventional approach and the reciprocal approach.

The conventional approach to the forward problem entails calculating the surface potentials starting from source current dipoles. The reciprocal approach, on the other hand, first solves for the electric field at the source dipole locations when the surface electrodes are reciprocally energized with a unit current. A scalar product of this electric field with the source dipoles then yields the surface potentials. The reciprocal approach promises a number of advantages over the conventional approach, including the possibility of increased surface potential accuracy and decreased computational requirements for inverse solutions.

In this thesis, the BEM equations for the conventional and reciprocal approaches are developed using a common weighted-residual formulation. The numerical implementation of both approaches to the forward problem is described for a single-dipole source model. A three-concentric-spheres head model is used for which analytic solutions are available. Scalp potentials are calculated at either the centroids or the vertices of the BEM discretization elements used. The performance of the conventional and reciprocal approaches to the forward problem is evaluated for radial and tangential dipoles of varying eccentricities and two widely different skull conductivities.

We then determine whether the potential advantages of the reciprocal approach suggested by forward problem simulations can be exploited to yield more accurate inverse solutions. Single-dipole inverse solutions are obtained using simplex minimization for both the conventional and reciprocal approaches, each with centroid and vertex options. Again, numerical simulations are performed on a three-concentric-spheres model for radial and tangential dipoles of varying eccentricities. The inverse solution accuracy of both approaches is compared for the two different skull conductivities and their relative sensitivity to skull conductivity errors and noise is assessed.

While the conventional vertex approach yields the most accurate forward solutions for a presumably more realistic skull conductivity value, both conventional and reciprocal approaches exhibit large errors in scalp potentials for highly eccentric dipoles. The reciprocal approaches produce the least variation in forward solution accuracy for different skull conductivity values. In terms of single-dipole inverse solutions, conventional and reciprocal approaches demonstrate comparable accuracy. Localization errors are low even for highly eccentric dipoles that produce large errors in scalp potentials on account of the nonlinear nature of the single-dipole inverse solution. Both approaches are also found to be equally robust to skull conductivity errors in the presence of noise.

Finally, a more realistic head model is obtained using magnetic resonance imaging (MRI) from which the scalp, skull, and brain/cerebrospinal fluid (CSF) surfaces are extracted. The two approaches are validated on this type of model using actual somatosensory evoked potentials (SEPs) recorded following median nerve stimulation in healthy subjects. The inverse solution accuracy of the conventional and reciprocal approaches and their variants, when compared to known anatomical landmarks on MRI, is again evaluated for the two different skull conductivities. Their respective advantages and disadvantages including computational requirements are also assessed.

Once again, conventional and reciprocal approaches produce similarly small dipole position errors. Indeed, position errors for single-dipole inverse solutions are inherently robust to inaccuracies in forward solutions, but dependent on the overlapping activity of other neural sources. Against expectations, the reciprocal approaches do not improve dipole position accuracy when compared to the conventional approaches. However, significantly smaller time and storage requirements are the principal advantages of the reciprocal approaches. This type of localization is potentially useful in the planning of neurosurgical interventions, for example, in patients with refractory focal epilepsy in whom EEG and MRI are often already performed.

Keywords: Electroencephalography, weighted-residual formulation, boundary-element method, equivalent current dipole, forward problem, reciprocity, inverse problem, source localization, somatosensory evoked potential.

Résumé

Le problème inverse en électroencéphalographie (EEG) est la localisation de sources de courant dans le cerveau utilisant les potentiels de surface sur le cuir chevelu générés par ces sources. Une solution inverse implique typiquement de multiples calculs de potentiels de surface sur le cuir chevelu, soit le problème direct en EEG. Pour résoudre le problème direct, des modèles sont requis à la fois pour la configuration de source sous-jacente, soit le modèle de source, et pour les tissues environnants, soit le modèle de la tête. Cette thèse traite deux approches bien distinctes pour la résolution du problème direct et inverse en EEG en utilisant la méthode des éléments de frontières (BEM): l'approche conventionnelle et l'approche réciproque.

L'approche conventionnelle pour le problème direct comporte le calcul des potentiels de surface en partant de sources de courant dipolaires. D'un autre côté, l'approche réciproque détermine d'abord le champ électrique aux sites des sources dipolaires quand les électrodes de surfaces sont utilisées pour injecter et retirer un courant unitaire. Le produit scalaire de ce champ électrique avec les sources dipolaires donne ensuite les potentiels de surface. L'approche réciproque promet un nombre d'avantages par rapport à l'approche conventionnelle dont la possibilité d'augmenter la précision des potentiels de surface et de réduire les exigences informatiques pour les solutions inverses.

Dans cette thèse, les équations BEM pour les approches conventionnelle et réciproque sont développées en utilisant une formulation courante, la méthode des résidus pondérés. La réalisation numérique des deux approches pour le problème direct est décrite pour un seul modèle de source dipolaire. Un modèle de tête de trois sphères concentriques pour lequel des solutions analytiques sont disponibles est utilisé. Les potentiels de surfaces sont calculés aux centroïdes ou aux sommets des éléments de discrétisation BEM utilisés. La performance des approches conventionnelle et réciproque pour le problème direct est évaluée pour des dipôles radiaux et tangentiels d'excentricité variable et deux valeurs très différentes pour la conductivité du crâne.

On détermine ensuite si les avantages potentiels de l'approche réciproque *suggérés par les simulations du problème direct peuvent êtres exploités pour donner des solutions inverses plus précises. Des solutions inverses à un seul dipôle sont obtenues en utilisant la minimisation par méthode du simplexe pour à la fois l'approche conventionnelle et réciproque, chacun avec des versions aux centroïdes et aux sommets. Encore une fois, les simulations numériques sont effectuées sur un modèle à trois sphères concentriques pour des dipôles radiaux et tangentiels d'excentricité variable. La précision des solutions inverses des deux approches est comparée pour les deux conductivités différentes du crâne, et leurs sensibilités relatives aux erreurs de conductivité du crâne et au bruit sont évaluées.*

Tandis que l'approche conventionnelle aux sommets donne les solutions directes les plus précises pour une conductivité du crâne supposément plus réaliste, les deux approches, conventionnelle et réciproque, produisent de grandes erreurs dans les potentiels du cuir chevelu pour des dipôles très excentriques. Les approches réciproques produisent le moins de variations en précision des solutions directes pour différentes valeurs de conductivité du crâne. En termes de solutions inverses pour un seul dipôle, les approches conventionnelle et réciproque sont de précision semblable. Les erreurs de localisation sont petites, même pour des dipôles très excentriques qui produisent des grandes erreurs dans les potentiels du cuir chevelu, à cause de la nature non linéaire des solutions inverses pour un dipôle. Les deux approches se sont démontrées également robustes aux erreurs de conductivité du crâne quand du bruit est présent.

Finalement, un modèle plus réaliste de la tête est obtenu en utilisant des images par resonace magnétique (IRM) à partir desquelles les surfaces du cuir chevelu, du crâne et du cerveau/liquide céphalorachidien (LCR) sont extraites. Les deux approches sont validées sur ce type de modèle en utilisant des véritables potentiels évoqués somatosensoriels enregistrés à la suite de stimulation du nerf médian chez des sujets sains. La précision des solutions inverses pour les approches conventionnelle et réciproque et leurs variantes, en les comparant à des sites anatomiques connus sur IRM, est encore une fois évaluée pour les deux conductivités différentes du crâne. Leurs avantages et inconvénients incluant leurs exigences informatiques sont également évalués.

Encore une fois, les approches conventionnelle et réciproque produisent des petites erreurs de position dipolaire. En effet, les erreurs de position pour des solutions inverses à un seul dipôle sont robustes de manière inhérente au manque de précision dans les solutions directes, mais dépendent de l'activité superposée d'autres sources neurales. Contrairement aux attentes, les approches réciproques n'améliorent pas la précision des positions dipolaires comparativement aux approches conventionnelles. Cependant, des exigences informatiques réduites en temps et en espace sont les avantages principaux des approches réciproques. Ce type de localisation est potentiellement utile dans la planification d'interventions neurochirurgicales, par exemple, chez des patients souffrant d'épilepsie focale réfractaire qui ont souvent déjà fait un EEG et IRM.

Mots-clés: *Électroencéphalographie, méthode des résidus pondérés, méthode des éléments de frontières, dipôle de courant équivalent, problème direct, réciprocité, problème inverse, localisation de source, potentiel évoqué somatosensoriel.*

Table of Contents

List of Tables

List of Figures

List of Symbols and Acronyms

3D	Three-dimensional
AEP	Auditory evoked potential
BEM	Boundary-element method
BESA	Brain Electrical Source Analysis
CC	Conventional centroid
CIHR	Canadian Institutes of Health Research
CRIUGM	*Centre de recherche de l'Institut universitaire de gériatrie de Montréal*
CSF	Cerebrospinal fluid
CSSD	Common spatial subspace decomposition
CT	Computed tomography
CURRY	Current Reconstruction and Imaging
CV	Conventional vertex
DSL	Dipole source localization
ECD	Equivalent current dipole

EEG	Electroencephalography
EEGLAB	Electroencephalography Laboratory
EGI	Electrical Geodesics Incorporated
EP	Evoked potential
ERP	Event-related potential
FDM	Finite-difference method
FEM	Finite-element method
FLASH	Fast low-angle shot
fMRI	Functional magnetic resonance imaging
FOV	Field of view
FRQS	*Fonds de recherche du Québec – Santé*
FS	Fat suppression
GFP	Global field power
HPC	High-performance computing
ICA	Independent component analysis
IRM	*Imagerie par résonance magnétique*

LCR	*Liquide céphalorachidien*
LORETA	Low-resolution electromagnetic tomography
MATLAB	Matrix Laboratory
MEG	Magnetoencephalography
MNI	Montreal Neurological Institute
MRI	Magnetic resonance imaging
MUSIC	Multiple signal classification
N_{20}-P_{20}	Negative and positive potential peaks measured at 20 ms post median nerve stimulation
NSERC	Natural Sciences and Engineering Research Council of Canada
PAL	Pre-auricular left
PAR	Pre-auricular right
PCA	Principal-component analysis
PET	Position emission tomography
RC	Reciprocal centroid
RDM	Relative-difference measure

R-MUSIC	Recursive multiple signal classification
RQCHP	*Réseau québécois de calcul de haute performance*
RV	Reciprocal vertex
SEP	Somatosensory evoked potentials
SI	Primary somatosensory cortex
SNR	Signal-to-noise ratio
SPECT	Single-position emission tomography
STDM	Spatio-temporal dipole modeling
SVD	Singular value decomposition
TE	Echo time
TR	Repetition time
VEP	Visual evoked potential

À Ramesh

Acknowledgements

Special thanks to the following individuals for all their invaluable assistance:

Marie-Claire ALBANESE
Andrew BAGSHAW
Michel BÉLAND
Louise BÉLANGER
Christian BÉNAR
André BLEAU
Natalie CHANG
Philippe COMTOIS
Laurent DESCARRIES
Anne-Sophie DUBARRY
Bruno DUBÉ
Emma DUERDEN
Michael FERREIRA
Sukhi GREWAL
Christophe GROVA
Colin HAWCO
Yann HENZEL
Peter JOHNSTON
Syma KHAN
Ping Hei LAM
Nadine LEBLANC
Robert LEBLANC
Richard LEFEBVRE
Frédéric LESAGE
Jean-Marc LINA
Bernard LORAZO

Kristina MARTINU
Pierre MATHIEU
Sylvain MILOT
Tomáš PAUS
Linda PELLETIER
Pierre RAINVILLE
Gonzalo REYES
Bart VANRUMSTE
Alain VINET

Chapter 1 Introduction

1.1 Reciprocity

The well-known theorem of reciprocity in electromagnetics was introduced by Helmholtz in 1853 (Helmholtz, 1853) and applied to electroencephalography (EEG) by Rush and Driscoll (1969) and Nunez (1981) for electrode sensitivity. It has since been used to compare sensitivity distributions for EEG and magnetoencephalography (MEG) (Malmivuo and Plonsey, 1995; Malmivuo et al., 1997). The reciprocity theorem has also been invoked to calculate potentials on a homogenous sphere (Brody et al., 1973), and on numerical head models employing the boundary-element method (BEM) (Fletcher et al., 1995; Finke, 1998), the finite-difference method (FDM) (Laarne, 2000; Laarne et al., 2000; Vanrumste et al., 2000; Vanrumste, 2001; Vanrumste et al., 2001; Hallez et al., 2005), and the finite-element method (FEM) (Weinstein et al., 2000). Riera and Fuentes (1998) presented an alternative reciprocal formulation for the BEM in terms of current fluxes.

The lead field is the electric field in a volume conductor generated by injecting unit current into a lead (i.e., an electrode pair on that volume conductor). According to the theorem of reciprocity, the electric field produced in this manner entirely determines the sensitivity distribution of the lead in question. This lead field therefore characterizes a type of electrical access of an electrode pair to any point in the volume conductor. It is only dependent on the geometric and electrical properties of the volume conductor, which is assumed passive in this case (i.e., containing no current sources), in addition to the position of the lead or electrode pair. Note that the electric field is the current density divided by the local conductivity (i.e., the electric field is directly proportional to the current density in a homogenous volume conductor model) and the lead field is the electric field normalized by the amplitude of the injected current (i.e., the lead field is equal to the electric field when unit current is injected).

The lead field defines the sensitivity of the electrode pair used for current injection and withdrawal to sources at a particular location in the volume conductor. In other words, knowledge of the electric field (or current density) throughout a volume conductor due to current injection across two stimulating electrodes fully describes how those same electrodes measure potentials due to sources anywhere in the volume conductor when they are used as EEG recording electrodes. The potential difference between these two electrodes generated by a current dipole (see Section 1.4) at the source location can be obtained by forming the scalar product of this electric field and the dipole moment. Calculating scalp potentials in this manner is called the lead-field or reciprocal approach and represents an alternative formulation for solving the EEG forward problem.

1.2 Forward Solutions

EEG deals with potentials recorded on the scalp resulting from the electrical activity of brain cells or neurons (see Section 1.4). The EEG forward problem generally refers to the determination of potential distributions resulting from known neural sources in a given volume conductor head model (Hallez et al., 2007). The mathematical formulation of the forward problem is obtained from Poisson's equation (Plonsey, 1969; Johnson, 1995; Gulrajani, 1998). Forward solutions can be used to compare scalp potentials (e.g., for different approaches to the forward problem or for calculated and measured potentials) (Fletcher et al., 1995, Finke, 1998) and for source imaging (e.g., cortical potential calculations) (Gevins et al., 1994; He et al., 1999). They are also usually required for EEG inverse solutions (Mosher et al., 1999b) and their validity is therefore presumed critical for accurate source localization (see Section 1.3).

Potential distributions can be calculated using analytic equations when volume conductors consisting of simple geometrical shapes such as spheres are considered (Rush and Driscoll, 1969; Ary et al., 1981). These analytical approaches were mostly used when computational capacity was more restricted (Gaumond et al., 1983; Gulrajani et al., 1984; Cuffin et al., 1985), but they are still currently employed especially as a reference for validation of numerical approaches (Thevenet et al., 1991; Yan et al., 1991; Eshel et al., 1995; Finke, 1998; Vanrumste et al., 2000) that may also be used on more realistically-shaped head models (see Section 1.5).

With the boundary-element method (BEM) for solving Poisson's equation numerically, only tissue boundaries between regions of differing conductivity are modeled (Barnard et al., 1967; Geselowitz, 1967; Meijs et al, 1989; Heller, 1990; de Munck, 1992; Fletcher et al., 1995; Schlitt et al., 1995; Ferguson and Stroink, 1997; Finke, 1998; Mosher et al., 1999b). The boundaries or surfaces are discretized into a finite number of surface elements and each region is allocated a conductivity that is assumed homogeneous and isotropic (i.e., identical throughout the region and in every direction (see Section 1.6)). The BEM is not capable of modeling anisotropic conductivities or discontinuous boundaries (e.g., holes in the skull) (see Section 1.5). Surface potentials are typically calculated at the vertices or centroids of the discretization elements (e.g., triangles or quadrilaterals). Numerical approaches for solving the integral equations assigned to the discretization elements are available (van Oosterom and Strackee, 1983; Meijs et al., 1987; Meijs et al., 1989; Heller, 1990; Oostendorp and van Oosterom, 1991; de Munck, 1992; Nishijo et al., 1994; Cuffin, 1995; Fletcher et al., 1995; Wischmann et al., 1996; Leahy et al., 1998; Mosher et al., 1999b) and allow faster calculations when compared to iterative methods. Further refinement of the discretization has been found to improve forward solution accuracy in certain cases (Meijs et al., 1989; Fletcher et al., 1995; Schlitt et al., 1995; Yvert et al., 1995; Finke et al., 1998; Fuchs et al., 1998a).

The BEM uses Green's Theorem to transform the differential equation describing the potential distribution within a volume conductor into an integral equation over the boundary surfaces between regions with different electrical properties (Brebbia and Dominguez, 1992). With the finite-element method (FEM) (Sepulveda et al., 1983; Thevenet et al., 1991; Yan et al., 1991; Awada et al., 1997; Buchner et al., 1997; Haueisen et al., 1997; van den Broek et al., 1998; Ollikainen et al., 1999; Weinstein et al., 2000), the finite-difference method (FDM) (Witwer et al., 1972; Stok and Wognum, 1988; Johnson, 1995; Lemieux et al., 1996; Saleheen and Ng, 1997; Laarne, 2000; Vanrumste, 2001; Hallez et al., 2005), and the finite-volume method (FVM) (Abboud et al., 1994; Rosenfeld et al., 1996), the potential is calculated throughout the entire volume, which leads to a larger number of calculations than with the BEM. This limited computational cost for the BEM is especially interesting when solving the inverse problem that consists of a large number of forward calculations. The advantages of the volume-based methods include the possibility of introducing a nearly unlimited number of conducting regions and potentially incorporating anisotropy.

Errors in forward solutions tend to be the largest for sources near the boundaries between regions of differing conductivity. Unfortunately, many EEG sources are assumed to lie in the cortex near the skull where a considerable difference in electrical properties exists (see Section 1.6). As mentioned above, the discretization in the vicinity of these cortical sources can sometimes be refined to improve scalp potential accuracy. In EEG inverse calculations (see Section 1.3), however, the location of the neural generators is not known in advance and discretization refinement is therefore required throughout the head model if more accurate forward solutions are required. The conventional approach to the EEG forward problem entails calculating the scalp surface potentials starting from neural sources. The reciprocal approach, on the other hand, first solves for the electric field at the source location when the surface electrodes are reciprocally energized with a unit current. A scalar product of this electric field with the source dipole then yields the surface potential (see Section 1.1). In effect, the reciprocal approach transfers the source currents from unknown source locations to the known positions of the current injecting electrodes, and the area around these electrodes can be selectively discretized for improved forward solution accuracy. These electrode locations are unchanging and hence this discretization refinement can be used to calculate scalp potentials due to sources at any location within the volume conductor.

Fletcher et al. (1995), in a simulation study employing a BEM three-concentric-spheres model for the head with selective discretization refinement around the electrode sites, found that the reciprocal approach indeed yielded more stable and accurate values for the surface potentials than did the conventional approach when sources near the skull were considered. A similar conclusion was reached in our previous work (Finke, 1998). An alternative reciprocal formulation for a vector version of the BEM (Riera and Fuentes, 1998) also produced more accurate forward solutions than the conventional approach. It remains to be seen whether this improved forward solution accuracy with the reciprocal approach translates into improved inverse solution accuracy (see Section 1.3). Further details on the computational requirements for the conventional and reciprocal approaches to the EEG forward problem are discussed in Section 1.7.

1.3 Inverse Solutions

The EEG is recorded at a limited number of locations on the scalp and the resulting signals are blurred by the volume conductor effects between source and electrode locations, most notably the relatively low skull conductivity, thereby limiting interpretation of the underlying sources that generate the measured potentials. EEG inverse solutions attempt to compensate for the low spatial resolution of the scalp-recorded potentials and the smearing effect of the skull in order to obtain more accurate information on these neural sources. Broadly speaking, these approaches can be divided into two categories, source imaging and source localization (Scherg, 1994; Grech et al., 2008). Source imaging aims at representing the scalp recorded EEG as an enhanced topographic map typically on either scalp or cortex that takes into account the volume conductor effects. Source localization or source analysis is used to determine the exact characteristics of the actual sources generating the scalp potentials. A combination of these two approaches is also possible (Kobayashi et al., 2000), for example, by incorporating the results of source imaging as a starting point for source localization (Gevins, 1998). Examples of source imaging include surface Laplacian derivations (Hjorth, 1975; Perrin et al., 1987; Hjorth, 1991; Nunez and Pilgreen, 1991; Law et al., 1993; Le et al., 1994; Babiloni et al., 1998), spatial deconvolution (e.g., software lens (Freeman, 1980), spatial deblurring (Le and Gevins, 1993; Gevins et al., 1994), cortical imaging (Kearfott et al., 1991; Sidman, 1991; Babiloni et al., 1997; Baillet and Garnero, 1997; Wang and He, 1998; He and al., 2002)), distributed source reconstruction (Nicolas and Deloche, 1976; Greenblatt, 1993; Gorodnitsky et al., 1995; Phillips et al., 1997; Russell et al., 1998; Fuchs et al., 1999; Michel et al., 1999), and low-resolution electromagnetic tomography (LORETA) (Pascual-Marqui et al., 1994).

The source localization approach to the EEG inverse problem therefore consists of locating electrical sources starting from measured potentials on the scalp (i.e., the EEG). Whereas the source model and volume conductor model are known in the forward problem and the scalp potentials are calculated, the head model and the surface potentials are given in the inverse problem and the sources are determined. Contrary to source imaging that generally makes no assumptions as to the number or even in some cases the types of sources generating the scalp potentials, the source localization approach to the EEG inverse problem requires specification of the source model(s) in order to be solvable (see Section 1.4). Source imaging approaches are therefore described as underdetermined (i.e., the number of sources is greater than the number of recording channels), while source localization approaches are typically described as overdetermined (i.e., the number of sources is less than the number of recording channels) (Simpson et al., 1995). The difficulty in the latter approach is determining the exact number of active sources.

As the inverse problem is ill posed and cannot be directly calculated, multiple forward iterations and linear and non-linear optimization procedures are usually required to obtain an inverse solution (see Section 1.7). Typically, a set of source parameters is initially assumed and then recursively modified (Scherg and Picton, 1991; Le and Gevins, 1993). The resulting source parameters correspond to those that best reproduce the measured potential distribution on the scalp for a given volume conductor (i.e. geometry (see Section 1.5) and electrical properties (see Section 1.6)). Least-squares-error fitting, where the sum-squared residual between the measured and calculated potentials is minimized, is probably the most widely used method in source localization (Stok, 1987; Srebro et al., 1993; Tseng et al., 1995). In practice, the square root of the normalized squared potential differences or relative-difference measure (RDM) is often employed since it not only renders the function to be minimized dimensionless, but it also reduces the magnitude range of this function for different source locations. As an extension, the minimum-norm least-squares method, also known as the Moore-Penrose generalized inverse, has also been used (He et al., 1987; Wang et al., 1992; Fuchs et al., 1999).

Alternatively, a scanning strategy approach can be used (Simpson et al., 1995) where multiple solutions are calculated at different locations to scan the source space in order to establish the best fitting solution. Multiple-signal classification (MUSIC) (Mosher et al., 1992) is such an approach as is its extension, recursive MUSIC (R-MUSIC) (Leahy et al., 1998; Mosher and Leahy, 1998). In a way, principal-component analysis (PCA) for spatio-temporal source modeling (see Section 1.4) can be considered a special case of the MUSIC algorithm (Soong and Koles, 1995; Schwartz et al., 1999). The EEG signal is decomposed into basic waveforms, namely into principal components, the number of which is taken to be the number of active sources (Mosher et al., 1992), although this does not hold for correlated EEG sources (Soong and Koles, 1995). Independent-component analysis (ICA) (Richards, 2004), an alternative decomposition method, may also be used in this manner. Singular value decomposition (SVD) has also been employed for estimating the properties of neural sources (Cardenas et al., 1995; Gençer and Williamson, 1998). Wang et al. (1999) applied common spatial subspace decomposition (CSSD) to extract EEG components specific to multiple stimuli conditions according to their spatial patterns. However, the efficacy of these approaches in clinical applications is largely dependent on how well the decomposed EEG components represent the phenomena being analyzed. Other approaches for source localization decompose EEG signals using wavelets (Geva et al., 1995) or are probability based (Raz et al., 1993; Scholz and Schwierz, 1994; Baillet and Garnero, 1997; Lütkenhöner, 1998; Bénar et al.; 2005).

1.4 Source Models

To solve the forward problem, models are needed for both the underlying source configuration, the source model, and the surrounding tissues, the volume conductor (see Section 1.5). Solving the inverse problem in terms of source localization is designed to produce exact parameters (e.g., position, orientation, and amplitude either at one instant or over time) for the source or sources generating the scalp potentials. For a given potential distribution on the scalp, there are an infinite number of different source configurations that can generate that potential distribution. In other words, there is no unique inverse solution (i.e., the inverse problem is ill-posed) (Helmholtz, 1853). Selecting a particular source model reduces the number of possible solutions allowing the inverse problem to be solved. The source model defines the assumed nature of the EEG generators, for example, the number of active areas, their size and type, as well as the temporal evolution of their activity, and depends on the particular phenomena under consideration. The validity of a given source model is therefore intimately related to the particular application it is being used for.

The equivalent current dipole (ECD) is a convenient and commonly used source model in both simulation studies (Stok, 1987; de Munck et al., 1988b; Homma et al., 1994; Tseng et al., 1995; Yvert et al., 1996; Awada et al., 1997; Ferguson and Stroink, 1997; Haueisen et al., 1997; Leahy et al., 1998; Huiskamp et al., 1999; Khosla et al., 1999; Krings et al., 1999) and clinical studies (Meijs and Peters, 1987; Lemieux and Leduc, 1992; Brigell et al., 1993; Gerson et al., 1994; Lantz et al., 1996; Diekmann et al., 1998; Yamazaki et al., 1998; Mosher et al., 1999b; Kobayashi et al., 2000). Each dipole represents a current source and sink of equal amplitude separated by a small distance. Macroscopically, this may be an adequate albeit simplified approximation for a focal area of the cortex (i.e., a few square centimeters or less) with a large number of parallel oriented pyramidal neurons that are simultaneously active (i.e., at least 10^5 cells). The superposition of the synchronized, individual electrical activity of these neurons generates a signal large enough to be measured on the scalp (Fender, 1987; Nunez, 1981; Nunez, 1990; Nunez, 1995; Gulrajani, 1998; Hara et al., 1999). The ECD represents the sum of these currents and is located at the center of mass of the region in question. This may be the case for certain epileptic spikes (Scherg et al., 1999; Lantz et al., 2003; Fuchs et al. 2007), early stages of an epileptic seizure (Ebersole and Wade, 1990; Boon and D'Havé, 1995; Boon et al., 1996), and evoked potentials (Lopes da Silva, 2004). If, however, diffuse or multiple regions of the brain are responsible for the EEG signal then a single dipole may be an oversimplified and inadequate source model (Snyder, 1991; Niedermeyer, 1996; Merlet and Gotman, 1999; Fuchs et al., 2004; Kobayashi et al., 2005) and any resulting inverse solutions should be interpreted with caution as they may not be physiologically meaningful. Note that it is theoretically possible for the folded geometry of the cortex to produce a zero net current if dipolar fields cancel each other out (Simpson et al., 1995).

In general, source localization can be divided into static and spatio-temporal approaches (Scherg, 1992). In the static approach, dipole position, orientation, and amplitude is determined from a single time point, for example, the peak of an EEG potential, or over a time interval or epoch of consecutive time points forming a trajectory of independent dipole locations and moments, i.e., moving-dipole solutions (Gulrajani et al., 1984; Cuffin, 1985; Cohen et al., 1990; Fuchs et al., 1998b; Krings et al., 1999). The spatio-temporal approach typically assumes dipoles with fixed positions and orientations and varying activity at different time points taking into account the temporal evolution of the potentials, i.e., fixed-dipole solutions (Scherg and von Cramon, 1985a; Scherg and von Cramon, 1985b; Scherg and von Cramon, 1986; de Munck, 1990; Scherg and Berg, 1991; Mosher et al, 1992). This reflects the assumption that the dipole represents a focal group of neurons oriented perpendicular to the cortical surface with unchanging position and orientation, and that variations in scalp potentials are exclusively due to variations in dipole amplitude. Dipoles with fixed positions but variable orientations as well as amplitudes are also possible (i.e., rotating-dipole solutions) as are combinations of both fixed and variable orientation dipoles. Multiple-dipole solutions, which assume more than one simultaneously active dipole, is designed to separate several different neural sources with overlapping EEG activity (Achim et al., 1991; Scherg, 1992; Mosher et al., 1993; Scherg et al., 1999) and can also be static or spatio-temporal. However, a greater number of dipoles can be located with a spatio-temporal approach than with the static approach for the same time interval because of the numerical instability in the inverse problem and smaller number of parameters to be determined with the spatio-temporal approach. The multipole is an extension of the dipole that includes higher-order components (Gulrajani, 1998). Other source models also exist (Malmivuo and Plonsey, 1995) but are rarely used in EEG forward and inverse problems.

Alternatively, in distributed source models the amplitudes of a fixed layer or patch of adjacent cortical dipoles are typically determined. The electrical activity is therefore not confined to one focal region but can correspond to a relatively large area of the cortex or multiple areas that can be active simultaneously (Koles, 1998; Pascual-Marqui, 1999). However, as the location of these dipoles is fixed, this type of model is classified more as a source imaging approach rather than a source localization approach to the EEG inverse problem (see Section 1.3).

Finally, note that as the complexity of the source model increases (e.g., number of sources), so does the solution parameter space and, potentially, the inverse solution times.

1.5 Head Models

Source localization relies on models of the geometric and electrical properties (see Section 1.6) of the head as well models of the current sources responsible for potentials on the scalp (Section 1.4). Relatively simple head models are often used, such as a single homogenous sphere (Frank, 1952; Schneider, 1972; Henderson et al., 1975; Gaumond et al., 1983; Cuffin, 1985; Kearfott et al., 1991; Gerson et al., 1994; Geva et al., 1995) or multilayer, spherical models (Rush and Driscoll, 1969; Schneider, 1974; Hosek et al., 1978; Butler et al., 1987; de Munck et al., 1988a; Salu et al., 1990; Cuffin, 1993; Schlitt et al., 1995), since analytic expressions for surface potentials resulting from source dipoles in the brain exist for these models. In experimental studies, including patients with implanted stimulating electrodes, single-dipole localization errors of 1-2 cm using three- or four-concentric-spheres head models have been found (Smith et al., 1985; Cuffin et al., 1991). However, spherical volume conductor models do not take into account individual differences in head shape, other than when possibly adapting the sphere radii, and are generally relatively poor approximation of the human head in regions other than the vertex and occiput. Realistic head models require more computationally expensive numerical calculations involving, for example, BEM discretization of the volume conductor surfaces. Therefore, the complexity of the head model determines the method of calculation and hence the computational requirements for both the forward and inverse problem, as well as the time and effort required to generate a more realistic head model in the first place (Johnson, 1995).

Several studies have shown that the use of spherical approximations for the human head can cause significant errors in source dipole localization (Ebersole, 2000; Herrendorf et al., 2000; Fuchs et al., 2001; Ebersole and Hawes-Ebersole, 2007). Using a homogeneous sphere, He and Musha (1989) demonstrated that inhomogeneities in the human head could lead to significant errors in dipole parameter estimation, especially when the sources were located close to those inhomogeneities and radially oriented towards them. Calculating scalp potentials on a three-shell, realistically-shaped head model and using three-shell, spherical models for inverse solutions, Roth et al. (1993) found dipole localization errors averaging 2 cm. Numerous attempts have been made to try and compensate for the effects of using a homogenous instead of a inhomogeneous volume conductor model (Ary et al., 1981; Nunez, 1981; Scherg and Von Cramon, 1986), and for using a spherical instead of a realistically-shaped volume conductor (Homma et al, 1995). Examples of the latter include the addition of a cerebrospinal fluid (CSF) layer between the skull and brain in the spherical models (Stok, 1987; Cuffin et al., 1991; Zhou and van Ooosterom, 1992; Mosher et al., 1993; Abboud et al., 1994, Tseng et al., 1995, Eshel et al., 1995; Radich and Buckley, 1995; Malmivuo et al., 1997, Diekmann et al., 1998; Suihko, 1998; Krings et al., 1999) and the inclusion of adjustable eccentric spheres (Meijs and Peters, 1987; Cuffin, 1991).

Head model accuracy was found to be even more critical if multiple simultaneously active sources were considered. Inverse solutions using a single homogenous sphere or a misspecified multiple-shell, spherical model led to large errors in dipole parameters when potentials were generated using a multiple-shell, spherical model and two dipole sources (Zhang and Jewett, 1993; Zhang et al., 1994). When a single-shell, realistically-shaped head model was used for potential calculations and a single homogenous sphere for inverse calculations, localization errors of up to 2.5 cm were found with some pairs of source dipoles (Fletcher et al., 1993). Other researchers have also studied localization errors due to misspecified head geometry (Srebro et al., 1993; Yvert et al., 1997; Fuchs et al., 1998a; Leahy et al., 1998; Silva et al., 1999). Another factor is the thickness of the respective layers used in the spherical models, as these are somewhat variable in the literature (Rush and Driscoll, 1969; Meijs et al., 1987; Cuffin et al., 1991; Zhang and Jewett, 1993; Eshel et al., 1995; Fletcher et al., 1995; Gençer and Williamson, 1998). However, localization errors remained below 1 cm in a study employing several tissue thicknesses as well as local variations in scalp and skull thickness (Cuffin, 1993).

Computational requirements associated with realistically-shaped head models requiring BEM implementation have become much less of a limitation with the current state of technology. He et al. (1987) used a single-shell, realistically-shaped head model with 682 elements for the localization of an epileptic focus. Balish et al. (1993) performed source localization using a three-shell, realistically-shaped head model consisting of 1600 elements per surface. Using a similar head model with a discretization consisting of approximately 3000 elements per surface, Buchner et al. (1995b) conducted source localization of somatosensory evoked potentials (SEPs) (see Section 1.8). The use of individual or standard realistically-shaped, inhomogeneous head models has now become commonplace (Hämäläinen and Sarvas, 1989; Srebro et al., 1993; Wieringa and Peters, 1993; Gevins et al., 1994; Homma et al., 1994; Yvert et al., 1995; Zanow and Peters, 1995; Abboud et al., 1996; Yamazaki et al., 1998; Ollikainen et al., 1999; Herrendorf et al., 2000; Kobayashi et al., 2000; Fuchs et al., 2002; Kobayashi et al., 2003; Fuchs et al. 2007). Comparing spherical, individual realistic, and standard realistic head models for localizing the source of epileptic signals (Silva et al., 1999), realistic head models increased dipole localization accuracy but the difference between individual and standard models was less than 1 cm. Buchner et al. (1995b) found an average difference in source location of 4 mm when comparing early SEP inverse solutions for realistic and spherical head models. However Cuffin et al. (2001) found no improvement in source localization accuracy when comparing realistically-shaped head models to spherical head models using implanted depth electrodes.

With the boundary-element method (BEM), the scalp, skull, brain, and CSF are most often represented (Fender, 1991). However, neglecting lesions, ventricles, and especially holes in the skull in volume conductor models has been shown to impact source localization in certain cases (van den Broek et al., 1998; Vanrumste, 2001). Compartment surfaces are typically described by averaged or individual anatomy obtained from surface digitization (Huppertz et al., 1998) or anatomical imaging such as magnetic resonance imaging (MRI) (Heinonen et al., 1997) and, to a lesser extent, computed tomography (CT). Skull geometry may be difficult to extract using standard MRI (Huiscamp et al., 1999), which is usually optimized for soft tissue separation (e.g., grey and white matter). CT may be better adapted for the extraction of a more realistic skull region, which is critical for accurate forward and inverse solutions (see Section 1.6), but soft tissues cannot be well separated. Although a combination of the two imaging modalities is possible via co-registration of the images and might yield the most accurate anatomical information, the radiation dose associated with CT scanning constitutes a limiting factor. Note that it is also possible to develop MRI sequences that are better adapted at separating tissues such as bone.

1.6 Skull Conductivity

In volume conductor modeling, each compartment is commonly assumed to be of homogenous and isotropic conductivity (Plonsey, 1995), that is to say the conductivity is the same throughout the compartment and in every direction (i.e., it is independent of the direction of current flow in the tissues). However, the human head is constituted of multiple tissue types with different conductivities, several of which are anisotropic (e.g., white matter, cortex, scalp, blood) (Robillard and Poussart, 1977; Rosell et al., 1988; Law, 1993; de Munck, 1988). For example, the conductivity differs in directions parallel and perpendicular to tissue fibers or the axons of neurons. Even the skull can be considered anisotropic since its conductivity is higher tangentially than perpendicularly to the skull surface (van den Broek et al., 1998). For anisotropic conductivity, methods have been suggested to calculate potentials analytically in multilayer spherical and spheroidal volume conductor models (de Munck et al., 1988a; Zhou and van Oosterom, 1992), and numerically in homogeneous (Wang and Eisenberg, 1994) and inhomogeneous (Saleheen and Ng, 1997; Marin et al., 1998) volume conductor models. However, the anisotropy of some tissues remains difficult to model in practice because of the complex geometry in, for example, the cortex (van Oosterom, 1991). Furthermore, although the BEM forward equations employ a quasi-static formulation where the potential distribution is assumed to be instantaneous and independent of frequency (i.e., the capacitive, inductive, and propagation effects can be neglected), the frequency dependence of the conductivity may in fact affect the EEG (Stinstra and Peters, 1998).

Both in spherical and realistically-shaped multilayer head models, the conductivities of the scalp, the skull, the brain and possibly the CSF compartments have to be specified. Advances in numerical approaches have allowed the inclusion of a greater number of tissue compartments in volume conductor modeling (e.g., grey and white matter, eyes, fat, muscle, and veins) (Law, 1993; Haueisen et al, 1997). However, even in realistically-shaped volume conductors, a given compartment will typically consist of more than one type of tissue. For example, the scalp actually consists of skin and muscles, and the CSF is often assigned to the brain compartment. There is, therefore, no guarantee that the effective compartment conductivities (i.e., those values that minimize the differences between the recorded and calculated EEG) correspond to the actual tissue conductivities of the brain, skull, and scalp (Peters, et al. (2004). Furthermore, there is inter-subject variability making any general conductivity assignment an approximation at best. In order to take into account the individual differences in effective conductivities, implanted electrodes [Homma et al., 1994], combined EEG and MEG (Cohen and Cuffin, 1983; Gonçalves et al., 2000), or impedance tomography (Oostendorp et al., 2000; Gonçalves et al., 2000) may be included as part of the EEG study. Using a spherical head model, Nunez (1987) also suggested a method of estimating local skull conductivity when both the source and scalp potentials are known. Another method for determining individual tissue conductivities in vivo as part of an EEG study was given by Ferree and Tucker (1999).

In many studies only conductivity ratios are considered rather than the absolute values (Zhang and Jewett, 1993; Fletcher et al., 1995; van Veen et al., 1997). If only the relative strength of the source is of interest, as is commonly the case in source localization, or only simulated potentials are being studied, as when comparing numerical and analytical solutions in a spherical volume conductor, then absolute conductivities are not important and it is sufficient to specify the ratio of the conductivities of the scalp, the skull, and the brain/CSF compartments. The skull conductivity has long been accepted as 1/80 times that of the scalp or of the brain and CSF (Rush and Driscoll, 1969). This was largely based on extrapolations of measurements by Rush and Driscoll (1968) demonstrating that the skull conductivity was 1/80 times that of saline. Other work also supported this conductivity ratio (Cohen and Cuffin, 1983; Homma et al., 1994). Recent skull conductivity measurements and simulations carried out by Oostendorp et al. (2000) suggested, however, that the skull conductivity is only 1/15 times that of cortex or scalp because the cortex conductivity is itself much less than that of saline. Some earlier studies also supported a higher skull conductivity (Kosterich et al., 1984; Law, 1993; Gabriel et al., 1996).

There is little consensus among researchers if the absolute values of these conductivities are to be used. A number of authors have reviewed the literature in order to collect the different conductivities applied to the field of source modeling (Foster and Schwan, 1989; van den Broek, 1998; Awada et al., 1998). Reports range from 0.1-0.77

S/m for the scalp, 0.004-0.07 S/m for the skull, 1-1.79 S/m for the CSF, and 0.33–0.45 S/m for the brain (0.16-0.48 S/m for grey matter and 0.08-1.19 S/m for white matter). Adopted from Geddes and Baker (1967), effective homogenous isotropic conductivities of 0.33 S/m assigned to the scalp, 0.0042 S/m assigned to the skull, and 0.33 S/m assigned to the brain/CSF compartments are commonly used for realistically-shaped multilayer boundary-element head models (Meijs et al., 1989; Buchner et al., 1995b; Kristeva-Feige et al., 1997). These values correspond to the previously mentioned ratio of 1:1/80:1 for the relative conductivity of the scalp, skull, and brain/CSF. Applying the more recent skull conductivity ratio of 1:1/15:1 to the above absolute values, we obtain the following conductivity values for the three compartments in question: 0.33, 0.22, and 0.33 S/m, respectively. Note that, although not always included as a separate compartment, the CSF layer has also been shown to have a significant influence on source localization despite its relatively small volume (Haueisen et al., 1997).

Although the simplest head model is a single homogenous sphere, the low conductivity of the skull mandates the use of a multilayer model where the skull, along with the scalp, brain, and possibly CSF, are represented (see Section 1.5). Errors in forward solutions tend to be the largest for sources near the boundaries between compartments of differing conductivity (see Section 1.2), especially when the difference in conductivity is considerable (Meijs et al., 1987). Many EEG sources are assumed to lie in the cortex near the skull (see Section 1.4), and adequate modeling of this region is therefore required for accurate scalp potential calculations. With a skull conductivity of 1/80, Hämäläinen and Sarvas (1989) demonstrated that the skull attenuated surface potentials to such an extent that standard forward solutions were rendered inaccurate, even when a three-shell, spherical head model was used. They suggested a two-step isolated-problem implementation in which cortical potentials were initially calculated assuming the skull to be perfect insulator (the so-called isolated brain problem), and then adding a correction factor to these isolated cortical potentials so as to obtain the surface potentials with the low-conductivity skull in place. This led to improved forward solution accuracy especially for eccentric dipoles. While increasing the skull conductivity from 1/80 to 1/15 renders the use of the isolated-problem implementation less critical, it still may be required for accurate scalp potential calculations.

The effects of conductivity errors have been discussed in many papers (Ary et al., 1981; Stok, 1987; Radich and Buckley, 1995; Haueisen et al., 1997; Pohlmeier et al., 1997; Awada et al., 1998; Huiskamp et al., 1999; Ollikainen et al., 1999, Vanrumste et al., 2000). Studying the influence of several modeling parameters on dipole localization using a four-shell spherical model, Stok (1987) concluded that conductivity changes affect the dipole moment rather than the dipole position. Ary et al. (1981) acknowledged the uncertainty of the 1/80 ratio, but found that a change of 20% in this value resulted in a change of only 2% in dipole position, expressed as a fraction of the radius of the scalp compartment. However, a relative skull conductivity of 1/15 represents a substantially larger change than that (i.e., a skull conductivity of 1/80 corresponds to a conductivity of 1/15-81.25%), and the impact of underestimating the skull conductivity by that much yielded position errors which were typically higher than those found due to neglecting the ventricular system or neglecting a hole in the skull when using finite-difference volume conductor models (Vanrumste et al., 2000). Increasing the number of electrodes improved these dipole position errors marginally. The dipoles were displaced in the radial outward direction from their original position, a tendency previously noted by other researchers when underestimating the skull conductivity (Pohlmeier et al., 1997; Awada et al., 1998).

1.7 Numerical considerations

The numerical methods applied to realistic volume conductor models require significant computational capacity and the multiple calculations of the forward solution that constitute the inverse solution is inevitably time consuming. The reciprocal approach provides a convenient means of cutting down on the laborious forward calculations since scalp potentials are only calculated between the electrode pairs. Fletcher et al. (1995) indicated that computation times for the reciprocal approach are linearly proportional to BEM head model size, while those of the conventional approach are proportional to its square. Furthermore, for a given BEM model, only the potentials and normal fluxes on the inner brain surface for each electrode pair need to be stored for subsequent inverse solution calculations with the reciprocal approach. In the conventional approach, storage requirements are again proportional to the square of BEM head model size. Although the initial generation of transfer matrices takes longer for the reciprocal approach than for the conventional approach (Fletcher et al., 1995), this is only required once for a given volume conductor discretization, after which inverse solutions can be repeatedly calculated for different potential distributions, time points, and source models. As such, another advantage of the reciprocal approach is its reduced time and storage requirements for EEG inverse solutions.

Inverse solutions involve the iterative adjustment of source parameters until the global minimum of the forward solution error function is found. Non gradient-based minimization techniques only use evaluations of the error function itself for each iteration. An example of this type of non-linear minimization technique is the well-known simplex algorithm (Nelder and Mead, 1965, Caceci and Cacheris, 1984), which has the advantages of being relatively simple and robust to local minima in the error function. Gradient-based minimization techniques use evaluations of both the error function and its partial derivatives with respect to the parameters to be optimized, when and if they exist, and therefore typically converge faster than the non gradient-based minimization techniques. An example of this type of minimization technique is Levenberg-Marquardt algorithm (Marquardt, 1963). With spherical head models, the existence of analytic expressions for the potential due to an arbitrary dipole makes minimization via the Levenberg-Marquardt the obvious choice. For the reciprocal approach, in which derivatives of the surface potential with respect to source location are available (Fletcher at al., 1995), minimization techniques that exploit these derivatives to accelerate convergence such as Levenberg-Marquardt can also be employed, even for realistic volume conductor models. The possibility of convergence to a local rather than a global minimum of both the simplex and Levenberg-Marquardt algorithms can be somewhat reduced by using another minimization algorithm, namely simulated annealing (Kirkpatrick et al., 1983; Geman and Geman, 1984; Gerson et al., 1994; Khosla et al., 1997), which can also be combined with a modified simplex algorithm (Press et al., 1992). Grave de Peralta Menendez and Gonzalez Andino (1994) have proposed an approach for testing whether these algorithms have found the global or a local minimum.

1.8 Clinical Applications

The EEG can be used to record either spontaneous electrical activity of the brain or evoked electrical activity in the form of evoked potentials (EPs) or event-related potentials (ERPs) induced by various stimuli. EEGs and EPs are routinely employed clinical examinations in neurology and provide a non-invasive means of gathering information on brain function and dysfunction. The spontaneously recorded EEG reflects various pathological conditions of the brain including epilepsy (Nunez, 1981). Visual evoked potentials (VEPs), median nerve SEPs, and brainstem auditory evoked potentials (AEPs) are the EPs that are most frequently used in clinical practice (Nuwer, 1998). SEPs can be recorded over the scalp and spine following repeated electrical stimulation of peripheral sensory nerve fibers and it is assumed that repetitive applications of the same stimulus will activate similar pathways. Averaging of the low-amplitude evoked signals (~1 μV), or epileptic spikes, is usually required to improve signal-to-noise ratio (SNR) (e.g., the noise level typically equals 20% for single epileptic spikes, but it typically equals 10% for averaged spikes) and to distinguish the EP from the spontaneous background EEG (Bronzino, 1995; Gulrajani, 1998). Digitally obtained data can be post-processed by a variety of signal-processing techniques (Bronzino, 1995; Blum, 1998; Lopes da Silva, 2004).

The EEG consists of a series of potential differences measured between pairs of scalp electrodes. The electrodes were historically set according to standard systems, usually either the 10-20 (typically 32 EEG channels) (Jasper, 1958) or the 10-10 (typically 64 EEG channels) (Sharbrough et al., 1991) electrode systems. EEG machines have since evolved into digital devices with increasing numbers of available recording channels (Blum, 1998). To record small potential fields, such as those of the early median nerve SEPs, an inter-electrode distance of less than 3 cm is required for accurate spatial sampling (Gevins et al., 1990; Spitzer et al., 1989). In modern systems the electrodes are attached to caps that can be rapidly placed and adapted to fit individual head shapes. Standard electrode positions can be determined from MRIs where the inion, nasion, and preauricular points have been marked, and the lines connecting these points can then be divided according to the 10-20 or 10-10 electrode systems (Hayashi et al., 1995;

Heinonen et al., 1999; Kobayashi et al., 2000). In spherical head models, the measured electrode positions can be projected onto the best fitting sphere (de Munck et al., 1991; Law and Nunez, 1991; Towle et al., 1993; Buchner et al., 1995b). However, these methods provide only an approximation of the electrode coordinates, which may lead to both electrode position errors and even source localization errors. Systems now exist for determining accurate electrode coordinates including digitization (Gevins et al., 1994; Wang et al., 1994; Simpson et al., 1995; Khosla et al., 1999) and marking techniques (Cohen et al., 1990; Buchner et al., 1997; Fuchs et al., 1998b) that correlate the anatomical images with the true electrode positions.

Single- or multiple-dipole models may be well suited for clinical applications such as EPs and epileptic foci (see Section 1.4). Dipole localization has been applied to both simulated and recorded VEPs using spherical (Brigell et al., 1993; Srebro et al., 1993) and realistic head models (Srebro and Oguz, 1997), but observed localization errors were relatively large (i.e., up to 5 cm). Again using spherical head models, AEPs have been localized using spatio-temporal dipole modeling (STDM) (Scherg and von Cramon, 1986) and dipole component modeling (Turetsky et al., 1990). Raz et al. (1993) employed frequency domain dipole localization to both VEPs and AEPs. Dipole source localization (DSL) has also been applied to epilepsy studies (Jayakar et al., 1991; Scherg and Ebersole, 1993; Scherg and Ebersole, 1994; Lantz et al., 1996; Ebersole, 1997; Shibata et al., 1998; Boon et al., 2000; Ebersole, 2000; Kobayashi et al., 2003; Ebersole and Hawes-Ebersole, 2007; Rose and Ebersole, 2009). Using simultaneous EEG and MEG data (see below) with a limited number of recording channels and a four-layer spherical head model, single-dipole solutions were found to be more stable than multiple-dipole solutions for individual epileptic spikes (Diekmann et al., 1998). A number of research groups (Fuchs et al., 1999; Gevins et al., 1999; Michel et al., 1999; Mosher et al., 1999a; Scherg et al., 1999) were asked to analyze the same epileptic data set with different source imaging and source localization approaches. It was concluded that each source localization approach had its limitations and failed under certain conditions, and that several distinct solutions were possible (Ebersole, 1999). As such, the use of multiple simultaneous approaches is probably required to obtain reliable results in clinical practice.

There also exists alternative means of imaging brain activity non-invasively other than EEG. The electric activity of the brain induces, in addition to the electric field, a magnetic field that can be detected above the scalp. The recording of the corresponding signal constitutes MEG. The relative advantages and disadvantages of source localization based on either EEG or MEG have given rise to much debate (Sarvas, 1987; Cohen et al., 1990; Tan et al., 1990; Ioannides, 1991; Mosher et al., 1992; Mosher et al., 1993; Wikswo et al., 1993; Haueisen et al., 1997; Malmivuo et al., 1997; Phillips et al., 1997; Fuchs et al., 1998b; Leahy et al., 1998; van den Broek et al., 1998; Barkley and Baumgartner, 2003; Barkley, 2004; Baumgartner, 2004; Scheler et al., 2007). Functional magnetic resonance imaging (fMRI), positron emission tomography (PET), and single-photon emission tomography (SPECT) provide information on the blood flow and metabolic activity of the brain (Shin, 2000; Rojo et al., 2001). The time resolution of these functional imaging modalities is typically in the order of seconds (Scherg, 1992). This produces temporal summation of phenomena lasting only milliseconds such as SEPs and spatial uncertainty in the images may therefore result, even if these modalities are generally considered to have better spatial resolution than EEG and MEG (Simpson et al., 1995; Korvenoja et al., 2006). Complementary data can however still be obtained from these images to estimate, for example, the number or approximate location of active sources, which then can be integrated into EEG and MEG source modeling (Buchner et al., 1994b; Dhawan et al., 1995; Sipilä et al., 2000; George et al., 2000). However, while increases in blood flow and metabolic activity also undoubtedly reflect active areas of the brain, the exact physical relationship between these areas and the sources of electrical activity measured on the scalp is uncertain.

The primary somatosensory cortex of the human brain (SI), the main sensory receptive area for the sense of touch, is located in postcentral gyrus of the parietal lobe (i.e., in the posterior bank of the central or Rolandic sulcus) and corresponds to Brodmann area 3b. The SI representation of the human hand was first described intra-operatively in cortical stimulation studies (Penfield and Boldrey, 1937). Since then position emission tomography (PET) (Fox et al., 1987; Nyberg et al., 1996; Bittar et al., 1999) and functional magnetic resonance imaging (fMRI) (Hammeke et al., 1994; Rao et al., 1995; Sakai et al., 1995; Puce et al., 1995; Lin et al., 1996; Pujol et al., 1996; Kurth et al., 1998) have been used to identify the primary sensory hand area non-invasively. The N_{20}-P_{20} is the earliest cortical potential elicited by median nerve stimulation and, based in part on direct cortical potential recordings (Woolsey et al., 1979; Allison, 1982; Wood et al., 1988; Allison et al., 1989), is believed to be generated by the SI. In these studies, the primary hand area has been shown to occupy a very limited volume of the postcentral gyrus (i.e., no more than 30 mm along the central sulcus). Inverse dipole solutions using magnetoencephalography (MEG) (Hari et al., 1984; Kaukoranta et al., 1986; Hari, 1991; Suk et al., 1991; Gallen et al., 1993; Hari et al., 1993; Yang et al., 1993; Kristeva-Feige et al., 1994; Kristeva-Feige et al., 1995; Nakamura et al., 1998) and EEG (Henderson et al., 1975; Buchner et al., 1995a; Kristeva-Feige et al., 1997) all point to a dipole source tangent to the scalp surface thought to reflect the response of pyramidal neurons in Brodmann area 3b to sensory afferents.

An equivalent dipole source model is now used to localize the central sulcus in the non-invasive pre-operative assessment of patients with a space-occupying lesion or an epileptogenic zone in the central region (Buchner et al., 1994a; Hayashi et al., 1995; Mine et al., 1998; Gross et al., 2000). However focal resection performed in the Rolandic area always carries the risk of sensory or motor deficits and functional information on this region is still often obtained through neurosurgical procedures (King and Schell, 1987; Berger et al., 1989; Burchiel et al., 1989; Suzuki and Yasui, 1992; Hirsch et al., 2000). The accuracy of EEG inverse solutions is limited by the extent to which scalp SEPs result from the superposition of several source activities located in different parts of the brain. Accounting for all these various effects requires a complex dipole model based on temporal as well as spatial information (Zhang et al., 1994). Equivalent dipoles are often also used to model these secondary overlapping sources (Baumgartner et al., 1991; Franssen et al., 1992; Buchner et al., 1995a; Valeriani et al., 2001), but the exact origins of these activities and the validity of a dipole model in these cases may be less obvious than for the N_{20}-P_{20} SEP (see Section 1.4). The accuracy of inverse dipole solutions based on scalp potentials has been reported to be in order of 1 cm for N_{20}-P_{20} SEPs (Scherg, 1992; Buchner et al., 1994a; Buchner et al., 1995a; Gross et al., 2000; Vanrumste, 2001). Using a combination of both EEG and MEG data on a realistically-shaped head model (Fuchs et al., 1998b), inverse solution results were improved but the use of a single-dipole model was found to be as accurate as more complicated source models for left-hand median nerve stimulation. SEPs have also been analyzed using spatial deblurring (Gevins et al., 1994) and spatio-temporal dipole localization using wavelets (Geva et al., 1995).

1.9 Overview

The present work consists of a comparison of conventional and reciprocal approaches to the EEG forward and inverse problems. The main objective is to follow the two approaches throughout the entire modeling process from beginning to end: starting with the fundamental equations, followed by discretization and numerical techniques, software design and implementation, then validation and comparison of the forward and inverse problems on simulated data, and finally comparison of inverse dipole localization on real EEG data. Progressing in this manner from fundamental physics, to biomedical engineering, and then to a clinical application, attempts to fully exploit the M.D./Ph.D. program context in which this thesis is conducted. The hope is that by trying to achieve an overall perspective, as opposed to focusing on a single step such as, for example, forward solution accuracy, some insight might be gained into the relative importance of different modeling aspects in terms of the ultimate goal, which is to say source localization. Our particular interest in the reciprocal approach is due to its encouraging scalp potential accuracy when using discretization refinement around electrode sites, especially for eccentric dipoles that tend to be problematic with the conventional approach. The potential translation of this improved forward solution accuracy to improved inverse solution accuracy, as well as the possibility of reduced computational requirements, are the main motivating factors for pursuing the reciprocal approach. Special attention is paid to the effects of skull conductivity on both approaches, since this appears to be a major determinant of EEG forward and inverse solution accuracy, and much uncertainty still surrounds the skull conductivity value that best reproduces scalp potentials (see Section 1.6).

Boundary-element field equations for the conventional and reciprocal approaches to the EEG forward problem are derived using a weighted-residual formulation, and details of their numerical implementation are described for a fairly general volume conductor geometry. These approaches are initially validated on a three-concentric-spheres head model consisting of planar triangles assuming either a constant or linear potential variation on those triangles. Similar surface discretizations with selective refinement around electrode sites are used for both approaches, but an additional curvilinear quadrilateral with quadratic interpolation is inserted at each electrode in one implementation of the reciprocal approach. Scalp potentials are calculated at either the centroids or the vertices of the BEM discretization elements used. Calculated scalp potentials are compared with simulated, analytic potentials for radial and tangential dipoles of varying eccentricity and two very different skull conductivity values. Conventional and reciprocal inverse single-dipole solutions are theoretically described and then calculated using simplex minimization again for radial and tangential dipoles of varying eccentricity and the two different values of skull conductivity. Inverse solution accuracy is compared in terms of dipole amplitude, orientation, and position and the effects of noise and conductivity errors are also studied.

Single-dipole inverse solutions are also determined on real EEG data for both conventional and reciprocal approaches. Bilateral median nerve stimulation is performed on three healthy subjects and inverse solutions for the N_{20}-P_{20} somatosensory evoked potentials (SEPs) are then obtained by simplex minimization. Inverse dipole position is validated against the primary sensory hand area identified on MRI. Solutions are compared for different time points, filtering strategies, skull conductivity values, and BEM discretizations. Realistically-shaped head models including scalp, skull, and brain/CSF surfaces are generated from individual MRIs and then discretized into planar triangles assuming either a constant or linear potential variation on those triangles. The 129 electrode sites considered are digitized and projected onto the individual scalp surfaces. Similar scalp surface discretizations consisting of planar triangles with and without selective refinement around electrode sites on the scalp are used, but again an additional curvilinear quadrilateral with quadratic interpolation is inserted at each electrode in one implementation of the reciprocal approach. Once again, scalp potentials are calculated at either the centroids or the vertices of the BEM discretization elements used. Discretizations for skull and brain/CSF surfaces are identical for all approaches. Computational requirements for the conventional and reciprocal approaches are also considered.

As far as we know, this work is the first to present EEG inverse solutions using a BEM reciprocal approach, both on spherical simulations and real data. Although BEM reciprocal forward solutions have been previously presented (Fletcher et al. 1995; Finke, 1998), we are the first to use the presumably more realistic skull conductivity of 1/15 and to compare conventional and reciprocal approaches on similar volume conductor models with selective refinement around electrode sites on the scalp (i.e., selective electrode refinement has been exclusively used for the reciprocal approach which makes comparisons problematic). The axis along which source dipoles are displaced in our spherical simulations is also more general than in Finke (1998), a greater number of discretization elements are used, and forward solution accuracy is compared using the actual error function minimized in the inverse problem, which is also not the case in Fletcher et al. (1995) and Finke (1998). Details on exact computational times and storage requirements in the literature are limited as the focus tends to be on solution accuracy, and analysis is often performed using commercially available software on personal computers. In this work we also study reciprocal and conventional approaches in terms of computational requirements for recorded SEPs. Comparing this present work with Finke (1998), other than the differences mentioned above, the equations derived for forward calculations have been reworked and the computer programs have been rewritten and updated.

Two commercial software packages are used in this work, BESA (Brain Electrical Source Analysis, Gräfelfing, DE) (Scherg and Picton, 1991) and CURRY (Current Reconstruction and Imaging, Neuroscan, Charlotte, NC), as well as several shareware programs including NeuroLens (University of Montreal, Montreal, QC) and EEGLAB (Electroencephalography Laboratory, Mathworks, Natick, MA). Original programs used in this thesis for both the forward and inverse problems are written in Fortran 90 and run through the *RQCHP* (*Réseau québécois de calcul de haute performance*). Source code is available on request via e-mail at .

Chapter 2 Conventional and Reciprocal Approaches to the Forward Problem of Electroencephalography[2]

Stefan Finke[1] and Ramesh M. Gulrajani[1]

[1]*Institut de génie biomédical, Faculté de médecine, Université de Montréal, Montréal, Québec, Canada.*

Published in Electromagnetics, vol. 21, no. 7, pp. 513-530, 2001. Manuscript received on February 10, 2001; manuscript accepted on April 11, 2001.

2.1 Preface

This work was conducted at the Institute of Biomedical Engineering, Faculty of Medicine, University of Montreal, in Montreal, Quebec, Canada from 1999 to 2001. Note that during this period research was conducted on a part-time basis in the context of an M.D./Ph.D. program through the University of Montreal. Original programs were written by Stefan Finke in Fortran 90 and run through the high-performance computing (HPC) facilities of the *RQCHP* (*Réseau québécois de calcul de haute performance*). Source code is available on request via e-mail at . Derivations presented in this paper are the work of Stefan Finke and Ramesh M. Gulrajani with the assistance of Dr. Peter Johnston of Griffith University, Australia, for some of the singular integrals. Text and figures represent the combined efforts of both authors. Financial support was provided by the Natural Sciences and Engineering Research Council of Canada (NSERC)

---

[2]

Reprinted, with permission, from S. Finke, R. M. Gulrajani, Conventional and reciprocal approaches to the forward problem of electroencephalography, Electromagnetics, Sept 2001.

and by the Canadian Institutes of Health Research (CIHR). Preliminary versions of portions of this work have been previously published as short conference proceedings (Finke and Gulrajani, 1999; Finke and Gulrajani, 2000).

2.2 Abstract

The conventional approach to forward problem solutions in electroencephalography entails computing the surface potentials starting from source current dipoles. The reciprocal approach, on the other hand, first solves for the electric field at the source dipole location when the surface electrodes are reciprocally energized with a unit current. A scalar product of this electric field with the source dipole then yields the surface potential. Using a common weighted-residual formulation, this paper initially develops the boundary-element field equations for both approaches, next describes the discretization and matrix deflation techniques to be used with them, and, using a three-concentric-spheres head model, finally evaluates their performance for two widely different skull conductivities. It was found that while a conventional vertex method, in which the desired potentials are calculated at the vertices as opposed to the centroids of the discretization triangles, in general yields the most accurate forward solutions for skull conductivities close to recently measured values, the reciprocal approaches offer the least variation in error for different skull conductivities.

Keywords: Electroencephalography, electrocardiography, forward problem, reciprocity, weighted residuals.

2.3 Introduction

In theoretical electroencephalography it is often necessary to calculate surface potentials assuming a given source. Given a source current dipole $\mathbf{J}_s$ in the volume conductor and surface electrodes A and B (Figure 2.1), the potential $u_{AB} \equiv u_A - u_B$

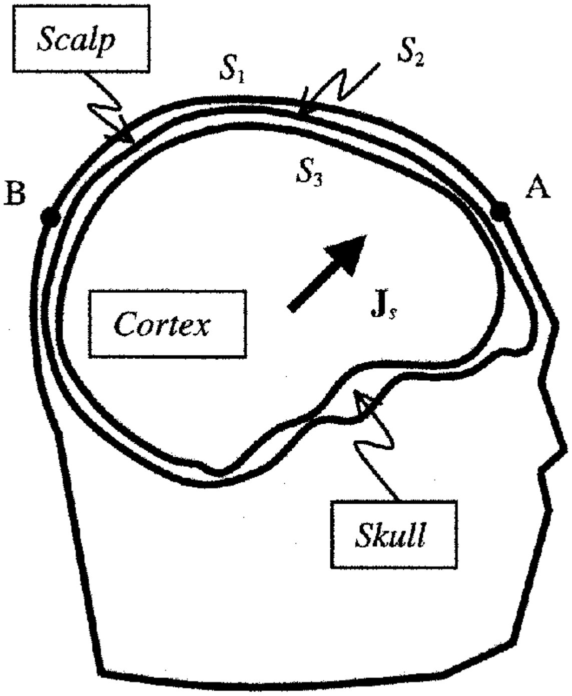

Figure 2.1. A three-surface head model with a source current dipole $\mathbf{J}_s$ and surface electrodes A and B.

between electrodes A and B may be expressed as $u_{AB} = \mathbf{L} \cdot \mathbf{J}_s$, where $\mathbf{L}$ is a so-called lead vector. The lead vector may be obtained by calculating the potentials u_{AB} corresponding to unit dipoles in the x, y, and z directions. The three values of the potentials then yield the lead vector components L_x, L_y, and L_z, respectively. Calculating the potential in this way constitutes the conventional approach to the forward problem of electroencephalography. An alternative determination of $\mathbf{L}$ invokes Helmholtz's principle of reciprocity, which states that $\mathbf{L} = -\mathbf{E}$, where $\mathbf{E}$ is the electric field set up at the dipole location when unit current is injected into the volume conductor at A and withdrawn at B. The reciprocal or ``lead-field'' approach to the forward problem thus entails calculating $\mathbf{E}$ in the volume conductor, which is now assumed to be passive with no dipole sources, due to this current injection at the surface electrodes. The potential is then obtained from $u_{AB} = -\mathbf{E} \cdot \mathbf{J}_s$.

Both conventional and reciprocal approaches entail building a numerical model of the volume conductor. Numerical volume conductor models may be of the finite-element

(FEM) or the boundary-element (BEM) type. Fletcher et al. (1995), in a simulation study employing a BEM three-concentric-spheres model for the head, found that the reciprocal approach yielded more accurate values for the surface potentials than did the conventional approach. Using a common weighted-residual formulation, this paper initially develops the BEM field equations for both conventional and reciprocal approaches, next describes the discretization and matrix deflation techniques to be used with them, and finally evaluates their performance for two widely different skull conductivities. All the equations developed here are also applicable to conventional and reciprocal solutions of the forward problem of electrocardiography.

2.4 Theory

2.4.1 Method of Weighted Residuals

The method of weighted residuals (Brebbia and Dominguez, 1992) is used to derive approximate solutions to partial differential equations over arbitrarily shaped regions. A fairly general volume conductor geometry may be assumed consisting of several regions of different isotropic conductivities, each region being bounded by nonintersecting and nontouching internal and/or external surfaces. Figure 2.1 shows a typical head model showing scalp, skull, and cortex regions. All surfaces are internal with the exception of the external scalp surface S_1. One region, here the cortex, is presumed to contain the active sources. Conductivities inside and outside the cortical surface $S_c (\equiv S_3)$ are denoted σ_c^- and σ_c^+, respectively. A similar volume conductor model can be constructed for the torso if electrocardiographic solutions are envisaged.

The governing Poisson's equation for the cortex region is

$$\sigma_c^- \nabla'^2 u = b, \tag{2.1}$$

where u is the potential and b the current sources. The prime on the Laplacian operator is used because $u(\mathbf{r}')$ is a function of the primed spatial variable $\mathbf{r}'$. Note that $b = \nabla' \cdot \mathbf{J}_s$ or equivalently $b = -I_{sv}$, depending on whether the source is a dipole moment density $\mathbf{J}_s$ expressed in A/m^2 or a volume source I_{sv} expressed in A/m^3 (Plonsey, 1969; Gulrajani, 1998). With weighted residuals, we aim to satisfy Poisson's equation in the form

$$\int_{V_c} \left[\sigma_c^- \nabla'^2 u - b\right] u^* \, dV' = 0, \tag{2.2}$$

where u^* denotes a weighting function, V_c the volume of interest (here the cortex), and the prime on dV' is used to signify that the spatial variable is the primed position vector $\mathbf{r}'$. The weighting function u^* is selected as the potential due to a point current source of unit strength situated at coordinate $\mathbf{r}$ in an infinite homogeneous medium of unit conductivity, in other words, we have

$$\nabla'^2 u^* = -\delta(\mathbf{r}'-\mathbf{r}) \tag{2.3}$$

with u^* given by $u^* = 1/(4\pi|\mathbf{r}'-\mathbf{r}|)$. Integrating (2.2) by parts yields

$$\int_{V_c} \left[\sigma_c^- (\nabla' u \cdot \nabla' u^*) + b u^*\right] dV' = \int_{S_c} \sigma_c^- q u^* \, dS', \tag{2.4}$$

where the flux $q \equiv \partial u / \partial n'$ is the normal derivative of u over the surface S_c bounding V_c. A second integration by parts converts (2.4) into

$$\int_{V_c} \left[-\sigma_c^- u \nabla'^2 u^*\right] dV' = \int_{S_c} \sigma_c^- q u^* \, dS' - \int_{S_c} \sigma_c^- u q^* \, dS' - \int_{V_c} b u^* \, dV', \tag{2.5}$$

where $q^* \equiv \partial u^* / \partial n'$. We now make use of (2.3). If $\mathbf{r}$ is inside V_c, the left-hand side of (2.5) becomes $\sigma_c^- u(\mathbf{r})$, where $u(\mathbf{r})$ is the potential at $\mathbf{r}$, and we have

$$\sigma_c^- u(\mathbf{r}) = \int_{S_c} \sigma_c^- q u^* \, dS' - \int_{S_c} \sigma_c^- u q^* \, dS' - \int_{V_c} b u^* \, dV'. \tag{2.6}$$

This yields the weighted residual equation for the potential $u(\mathbf{r})$ at an arbitrary interior point of V_c. Note that $\mathbf{r}$ can also be selected outside V_c, in which event the left-hand sides of (2.5) and (2.6) are zero. With the BEM approach, however, $\mathbf{r}$ is placed on a boundary surface. The surface integrals in (2.6) now exhibit singularities, when $\mathbf{r}' = \mathbf{r}$, that need special attention.

2.4.2 Conventional Approach

Derivation of the Integral Equation

In the conventional approach we start with current sources b and aim to calculate the potential u on every surface. Its normal derivative q is of no interest to us. Equation (2.6) is applied to each volume conductor region in turn, *keeping* $\mathbf{r}$ *fixed at a particular surface*. If as in Figure 2.1, we have three regions, the three resulting equations are then summed. Regions other than the cortex contain no sources b, so the last volume integral in (2.6) disappears for these regions. Since the normal component of the current is continuous across interfaces, the first surface integral in (6) will yield equal and opposite contributions for adjacent regions. Moreover, the first surface integral is zero over the outer surface S_1, as no current crosses over into air. Assuming $\mathbf{r}$ to be selected on a particular surface S_r (actually infinitesimally close to S_r but on the inside), the summed equations give

$$\sigma_r^- u_r(\mathbf{r}) = -\sum_{s=1}^{M} (\sigma_s^- - \sigma_s^+) \int_{S_s} uq^* \, dS' - \int_{V_c} bu^* \, dV', \tag{2.7}$$

where it is assumed that all surface normals point outward (toward σ_s^+) and the additional subscript $\mathbf{r}$ on $u_r(\mathbf{r})$ explicitly indicates that $\mathbf{r}$ lies on S_r. The index s ranges over all M assumed surfaces, even S_1, since $\sigma_1^+ = 0$. Note how the summation eliminates the first surface integral in (2.6) and hence the flux terms q. We now split the integral over S_r in two by demarcating a small region S_ε around $\mathbf{r}$. This leads to

$$\sigma_r^- u_r(\mathbf{r}) = -\sum_{s=1}^{M} (\sigma_s^- - \sigma_s^+) \int_{\bar{S}_s} uq^* \, dS' - (\sigma_s^- - \sigma_s^+) \int_{S_\varepsilon} uq^* \, dS' - \int_{V_c} bu^* \, dV', \tag{2.8}$$

where $\bar{S}_s$ is used to signify that in the summation the integral over S_r excludes the region S_ε. Using

$$q^* \, dS' = \frac{1}{4\pi} \nabla' \left(\frac{1}{|\mathbf{r}' - \mathbf{r}|} \right) \cdot d\mathbf{S}',$$

and consequently

$$\int_{S_\varepsilon} q^* \, dS' = -\frac{1}{4\pi} \Omega^-(S_\varepsilon; \mathbf{r}),$$

where $\Omega^-(S_\varepsilon; \mathbf{r})$ is the solid angle subtended by S_ε at $\mathbf{r}$ and the minus superscript indicates that $\mathbf{r}$ is assumed on the inside, we can rewrite (2.8) as

$$\begin{aligned} &\left[\Omega^-(S_r - S_\varepsilon; \mathbf{r}) \sigma_r^- + \Omega^-(S_\varepsilon; \mathbf{r}) \sigma_r^+ \right] u_r(\mathbf{r}) \\ &\qquad = -\sum_{s=1}^{M} (\sigma_s^- - \sigma_s^+) \int_{\bar{S}_s} u \nabla' \left(\frac{1}{|\mathbf{r}' - \mathbf{r}|} \right) \cdot d\mathbf{S}' - 4\pi \int_{V_c} bu^* \, dV'. \end{aligned} \tag{2.9}$$

In deriving (2.9), we have explicitly used the fact that $\Omega^-(S_r - S_\varepsilon; \mathbf{r}) + \Omega^-(S_\varepsilon; \mathbf{r}) = 4\pi$. Substituting for u^* in (2.9) and using $b = -I_{sv}$ yields

$$\left[\Omega^{-}(S_r - S_\varepsilon;\mathbf{r})\sigma_r^{-} + \Omega^{-}(S_\varepsilon;\mathbf{r})\sigma_r^{+}\right]u_r(\mathbf{r})$$

$$= \int_{V_c} \frac{I_{sv}}{|\mathbf{r}'-\mathbf{r}|}dV' - \sum_{s=1}^{M}(\sigma_s^{-} - \sigma_s^{+})\int_{\bar{S}_s} u\nabla'\left(\frac{1}{|\mathbf{r}'-\mathbf{r}|}\right)\cdot d\mathbf{S}'. \tag{2.10}$$

The first term on the right-hand side in (2.10) can be rewritten as

$$\int_{V_c} \frac{I_{sv}}{|\mathbf{r}-\mathbf{r}'|}dV' = 4\pi u^{\infty}(\mathbf{r}),$$

where $u^{\infty}(\mathbf{r})$ represents the potential at $\mathbf{r}$ assuming that the cortical sources exist in an infinite homogeneous medium of unit conductivity. This gives

$$\left[\sigma_r^{-}\Omega^{-}(S_r - S_\varepsilon;\mathbf{r}) + \sigma_r^{+}\Omega^{-}(S_\varepsilon;\mathbf{r})\right]u_r(\mathbf{r})$$

$$= 4\pi u^{\infty}(\mathbf{r}) - \sum_{s=1}^{M}(\sigma_s^{-} - \sigma_s^{+})\int_{\bar{S}_s} u(\mathbf{r}')\nabla'\left(\frac{1}{|\mathbf{r}-\mathbf{r}'|}\right)\cdot d\mathbf{S}' \tag{2.11}$$

as the fundamental integral equation for the conventional approach to the forward problem valid for $\mathbf{r}$ on S_r.

Discretization of the Integral Equation

If we assume that each surface S_s is discretized into E_s elements (which may be triangular or quadrilateral in shape), then a discretized version of (2.11) is

$$\left[\sigma_r^{-}\Omega^{-}(S_r - S_\varepsilon;\mathbf{r}) + \sigma_r^{+}\Omega^{-}(S_\varepsilon;\mathbf{r})\right]u_r(\mathbf{r})$$

$$= 4\pi u^{\infty}(\mathbf{r}) - \sum_{s=1}^{M}(\sigma_s^{-} - \sigma_s^{+})\sum_{j=1}^{E_s}\int_{\bar{\Delta}_j^s} u(\mathbf{r}')\nabla'\left(\frac{1}{|\mathbf{r}-\mathbf{r}'|}\right)\cdot d\mathbf{S}', \tag{2.12}$$

where Δ_j^s denotes element j of surface S_s, but by placing a bar over it we mean that elements (or portions of elements) within the region S_ε are excluded. Next we select an ensemble of N functions $\{h_n(\mathbf{r})\}_{n=1}^{N}$, together with an ensemble of N collocation points on the surfaces S_s characterized by the position vectors $\{\mathbf{r}_m\}_{m=1}^{N}$ such that

$$h_n(\mathbf{r}_m) = \delta_{nm}. \tag{2.13}$$

We seek an approximate solution given by the expansion

$$u(\mathbf{r}) = \sum_{n=1}^{N} u_n h_n(\mathbf{r}), \tag{2.14}$$

where the coefficients u_n represent the unknown potentials. For example, with the surfaces discretized into N $(N=\sum_s E_s)$ triangles, and $\mathbf{r}_m$ the position vectors to the triangle centroids, by selecting $h_n(\mathbf{r})=1$ on triangle n and zero elsewhere, equation (2.13) is obviously satisfied. From (2.14), the unknown potentials are constant on each triangle and equal to u_n. This constitutes the *centroid* option. On the other hand, we may conceive of a *vertex* option in which the unknowns are the potentials at the N vertices of the surface mesh of triangles. (For the same value of N, this represents a finer mesh of triangles, since for a given mesh the number of vertices is approximately half the number of triangles.) The $\mathbf{r}_m$ are now the position vectors to these vertices. For a linear interpolation of the potential across each triangular face, we select

$$\begin{aligned} h_n(\mathbf{r}) &= \frac{d(\mathbf{r},\mathbf{r}_k,\mathbf{r}_l)}{d(\mathbf{r}_n,\mathbf{r}_k,\mathbf{r}_l)}, && \mathbf{r} \in \text{all triangles } \Delta^s_{n(kl)} \text{ with } n \text{ as a vertex,} \\ &= 0 && \text{otherwise,} \end{aligned} \tag{2.15}$$

where $d(\mathbf{r}_n,\mathbf{r}_k,\mathbf{r}_l) \equiv \mathbf{r}_n \cdot (\mathbf{r}_k \times \mathbf{r}_l)$ is the determinant of triangle $\Delta^s_{n(kl)}$ on surface S_s, whose vertices are given by $\mathbf{r}_n$, $\mathbf{r}_k$, and $\mathbf{r}_l$. Note that (2.15) also satisfies condition (2.13).

Substituting (2.14) in (2.12) and setting $\mathbf{r}=\mathbf{r}_m$, we obtain

$$\begin{aligned} &\left[\sigma_r^- \Omega^-(S_r - S_\varepsilon;\mathbf{r}_m) + \sigma_r^+ \Omega^-(S_\varepsilon;\mathbf{r}_m)\right] u_m \\ &= 4\pi u^\infty(\mathbf{r}_m) - \sum_{n=1}^{N} u_n \sum_{s=1}^{M} (\sigma_s^- - \sigma_s^+) \sum_{j=1}^{E_s} \int_{\bar{\Delta}^s_j} h_n(\mathbf{r}')\nabla'\left(\frac{1}{|\mathbf{r}_m - \mathbf{r}'|}\right)\cdot d\mathbf{S}'. \end{aligned} \tag{2.16}$$

By placing $\mathbf{r}_m$ at each of the N collocation points in turn, we obtain a set of N equations such as (2.16), which may be written compactly in matrix form

$$\mathbf{AU}=\mathbf{G}, \tag{2.17}$$

where $\mathbf{U}$ is an $N\times 1$ column matrix of the desired potentials, $\mathbf{G}$ is an $N\times 1$ column matrix of the first terms on the right-hand side of equation (2.16) $(\mathbf{g}_m = 4\pi u^\infty(\mathbf{r}_m))$, and $\mathbf{A}$ is an $N\times N$ coefficient matrix. The elements of $\mathbf{A}$ are given by

$$\begin{aligned} a^{rt}_{mn} &= \sum_{s=1}^{M} (\sigma_s^- - \sigma_s^+) \sum_{j=1}^{E_s} \int_{\bar{\Delta}^s_j} h_n(\mathbf{r}')\nabla'\left(\frac{1}{|\mathbf{r}_m - \mathbf{r}'|}\right)\cdot d\mathbf{S}' \\ &\qquad + \delta_{mn}\left[\sigma_r^- \Omega^-(S_r - S_\varepsilon;\mathbf{r}_m) + \sigma_r^+ \Omega^-(S_\varepsilon;\mathbf{r}_m)\right], \end{aligned} \tag{2.18}$$

where the first superscript in a^{rt}_{mn} identifies the surface S_r associated with $\mathbf{r}_m$ and the second superscript the surface S_t associated with Δ^t_n. The elements of $\mathbf{A}$ are determined solely by the geometry of the volume conductor and its different conductivities, and (2.17) is therefore a linear equation. It needs to be inverted to obtain $\mathbf{U}$, the matrix of potentials.

From physical considerations, we know that the conventional potential problem is indeterminate up to a constant for the potential. It follows that the matrix $\mathbf{A}$ must be singular. This is achieved by imposing the condition

$$\sum_{n=1}^{N} h_n(\mathbf{r}) = 1, \tag{2.19}$$

where $\mathbf{r}$ is a point on any of the surfaces S_s. This condition is manifestly true for the centroid approach. Using (2.15), it is also easily verified for the vertex approach. With this condition we can show that each row of $\mathbf{A}$ sums to zero. In other words,

$$\begin{aligned}\sum_{n=1}^{N} a_{mn}^{rt} = \sum_{s=1}^{M} (\sigma_s^- - \sigma_s^+) \sum_{j=1}^{E_s} \int_{\bar{\Delta}_j^s} \nabla'\left(\frac{1}{|\mathbf{r}_m - \mathbf{r}'|}\right) \cdot d\mathbf{S}' \\ + \left[\sigma_r^- \Omega^-(S_r - S_\varepsilon; \mathbf{r}_m) + \sigma_r^+ \Omega^-(S_\varepsilon; \mathbf{r}_m)\right] = 0.\end{aligned} \tag{2.20}$$

This can be seen by noting that the sum

$$\sum_{j=1}^{E_s} \int_{\bar{\Delta}_j^s} \nabla'\left(\frac{1}{|\mathbf{r}_m - \mathbf{r}'|}\right) \cdot d\mathbf{S}'$$

in (2.20) is equal to $-\Omega^-(S_r - S_\varepsilon; \mathbf{r}_m)$ for $S_s = S_r$, is equal to -4π for $S_r \subset S_s$, and is zero otherwise. The result in (2.20) then follows by using $\sigma_1^+ = 0$ and the condition $\sigma_{s-1}^+ = \sigma_s^-$ for nested surfaces such as those in Figure 2.1. From (2.20) it follows that the $N \times 1$ column vector of ones, denoted $\mathbf{e}$, is an eigenvector of $\mathbf{A}$ corresponding to the eigenvalue zero. It confirms that $\mathbf{A}$ is singular and that this singularity holds for both centroid and vertex options.

For the centroid option, from (2.18), the off-diagonal terms of $\mathbf{A}$ are given by

$$a_{mn}^{rt} = (\sigma_t^- - \sigma_t^+) \int_{\Delta_n^t} \nabla'\left(\frac{1}{|\mathbf{r}_m - \mathbf{r}'|}\right) \cdot d\mathbf{S}' = -(\sigma_t^- - \sigma_t^+)\Omega(\Delta_n^t; \mathbf{r}_m), \tag{2.21}$$

where $\Omega(\Delta_n^t; \mathbf{r}_m)$ is the solid angle subtended by triangle Δ_n^t at $\mathbf{r}_m$. Numerical values for $\Omega(\Delta_n^t; \mathbf{r}_m)$ are computed by an analytical formula due to van Oosterom and Strackee (1983). The diagonal terms of $\mathbf{A}$ are given by $a_{mm}^{rr} = \left[\sigma_r^- \Omega^-(S_r - S_\varepsilon; \mathbf{r}_m) + \sigma_r^+ \Omega^-(S_\varepsilon; \mathbf{r}_m)\right] =$

$2\pi(\sigma_r^- + \sigma_r^+)$ since both solid angles are equal to 2π due to the surface being smooth around the centroid.

For the vertex option, again from (2.18), the off-diagonal terms of $\mathbf{A}$ are

$$a_{mn}^{rt} = (\sigma_t^- - \sigma_t^+) \sum_{\forall \Delta_{n(kl)}^t} \int_{\Delta_{n(kl)}^t} \frac{d(\mathbf{r}', \mathbf{r}_k, \mathbf{r}_l)}{d(\mathbf{r}_n, \mathbf{r}_k, \mathbf{r}_l)} \nabla' \left(\frac{1}{|\mathbf{r}_m - \mathbf{r}'|} \right) \cdot d\mathbf{S}', \tag{2.22}$$

where $\forall \Delta_{n(kl)}^t$ denotes that the summation is done over all triangles $\Delta_{n(kl)}^t$ that include the vertex n. An analytic expression for the integration over the triangles in (2.22) is found in de Munck (1992). The diagonal terms of $\mathbf{A}$, given again by $a_{mm}^{rr} = \left[\sigma_r^- \Omega^-(S_r - S_\varepsilon; \mathbf{r}_m) + \sigma_r^+ \Omega^-(S_\varepsilon; \mathbf{r}_m)\right]$, are difficult to compute since the auto solid angle $\Omega^-(S_\varepsilon; \mathbf{r}_m)$ at the vertex $\mathbf{r}_m$ is not as easily inferred as for the centroid option. One approximation is to make use of (2.20) and simply set $a_{mm}^{rr} = -\sum_{n=1, n \neq m}^{N} a_{mn}^{rs}$. This is the approach we used, as it also conserves the singularity of $\mathbf{A}$. Other approximations are discussed in Meijs et al. (1989), Heller (1990), and Wischmann et al. (1996).

Deflation

The singularity of $\mathbf{A}$ precludes a simple inversion of the matrix equation (2.17). Neither can the solution $\mathbf{U}$ be obtained via iterative techniques. Barnard and coworkers (Barnard et al., 1967; Lynn and Timlake, 1968) first suggested the use of matrix deflation to solve (2.17). In effect, we solve for

$$\mathbf{A}^* \, \mathbf{V} = \mathbf{G}, \tag{2.23}$$

where $\mathbf{V}$ is the new sought-after solution and $\mathbf{A}^*$ denotes a “deflated’’ matrix derived from $\mathbf{A}$ using the relation

$$\mathbf{A}^* = \mathbf{A} + \mathbf{e}\mathbf{p}^T. \tag{2.24}$$

The matrix $\mathbf{e}$ is, as before, an $N \times 1$ matrix of ones, $\mathbf{p}$ is an $N \times 1$ column matrix whose first N_1 terms are each $1/N_1$ and the rest are zeros, and the superscript T denotes the transpose. Here N_1 denotes either the number of triangles on the outer surface S_1 for the centroid option or the number of vertices on S_1 for the vertex option. Using $\mathbf{p}^T\mathbf{e} = 1$, it is easy to show that $\mathbf{e}$, which was an eigenvector of $\mathbf{A}$ corresponding to the eigenvalue $\lambda = 0$, becomes an eigenvector of $\mathbf{A}^*$ with eigenvalue $\lambda = 1$. Thus the eigenvalue $\lambda = 0$

has been removed or deflated (provided it was a simple eigenvalue) and the coefficient matrix $\mathbf{A}^*$ is consequently nonsingular. Thus (2.23) can be inverted. However, it is by no means certain that $\mathbf{V}$ is the sought-after potential. Now any particular solution $\tilde{\mathbf{U}}$ of the original equation $\mathbf{AU} = \mathbf{G}$ that also satisfies the condition $\mathbf{p}^T\tilde{\mathbf{U}} = 0$ will satisfy (2.23), since we have $\mathbf{A}^* \tilde{\mathbf{U}} = (\mathbf{A} + \mathbf{ep}^T)\tilde{\mathbf{U}} = \mathbf{G}$. Since, by virtue of the nonsingularity of its coefficient matrix, equation (2.23) has a unique solution, it follows that $\tilde{\mathbf{U}}$ is this unique solution. In other words, by solving (2.23) with the particular choice of $\mathbf{p}$ described above, we end up obtaining that solution of (2.17) corresponding to the condition $\mathbf{p}^T\tilde{\mathbf{U}} = 0$. This condition simply stipulates that the sum of the potentials on the outer surface S_1 is zero and corresponds to using a reference for the potential that is equal to the mean of the potentials on S_1.

Compensation for Low-Skull Conductivity

The skull conductivity has long been accepted as 1/80 times that of the scalp or of the cortex. This was largely based on extrapolations of measurements by Rush and Driscoll (1968) that the skull conductivity was 1/80 times that of saline. With this low conductivity, Hämäläinen and Sarvas (1989) showed that the skull attenuated surface potentials to such an extent that the above solution is rendered inaccurate. They proposed a two-step procedure that essentially involves first calculating the cortex surface potentials assuming the skull to be a perfect insulator (the so-called isolated brain problem) and then adding a correction term to these isolated brain potentials so as to obtain the surface potentials with the low-conductivity skull in place. This led to much more accurate surface potentials than a direct one-step calculation. Recent skull conductivity measurements and simulation tests done by Oostendorp et al. (2000) suggest, however, that the skull conductivity is only 1/15 times that of cortex or scalp because the cortex conductivity is itself much less than that of saline. While the increased ratio of skull to brain conductivity from 1/80 to 1/15 renders the use of the isolated problem procedure less critical, it is still required for accurate computation of electroencephalographic potentials. For electrocardiographic potentials, this isolated problem procedure is not needed at all.

2.4.3 Reciprocal Approach

The weighted residual equation (2.6) can also be used to set up the reciprocal approach to the forward problem. Now, however, the flux q is of interest, as we need it to eventually calculate the electric field at the dipole source location. Since this field is calculated in response to unit current injection and withdrawal at the surface electrodes but with the biological sources assumed to be zero, the last term in (2.6) drops out. Equation (2.6) is then applied to each volume region in turn. Thus, for the cortical region, we have

$$4\pi u(\mathbf{r}) = \int_{S_c} q\left(\frac{1}{|\mathbf{r}'-\mathbf{r}|}\right) dS' - \int_{S_c} u\nabla'\left(\frac{1}{|\mathbf{r}'-\mathbf{r}|}\right)\cdot d\mathbf{S}', \tag{2.25}$$

where we have again used

$$u^* = \frac{1}{4\pi|\mathbf{r}'-\mathbf{r}|} \quad \text{and} \quad q^*\, dS' = \frac{1}{4\pi}\nabla'\left(\frac{1}{|\mathbf{r}'-\mathbf{r}|}\right)\cdot d\mathbf{S}'$$

and the regional conductivity σ_c^- drops out, as it is common to all terms. In (2.25) the position vector $\mathbf{r}$ is assumed strictly inside the region V_c. Now let $\mathbf{r}$ be at the surface S_c but nevertheless just within it. Both surface integrals become singular when $\mathbf{r}'=\mathbf{r}$. As before, we demarcate S_ε around $\mathbf{r}$ and separate out the singularity in the second integral, but keep it in the first since the lower order $1/|\mathbf{r}'-\mathbf{r}|$ singularity can be handled during integration. Equation (2.25) becomes

$$\left[4\pi - \Omega^-(S_\varepsilon;\mathbf{r})\right]u(\mathbf{r}) = \int_{S_c} q\left(\frac{1}{|\mathbf{r}'-\mathbf{r}|}\right) dS' - \int_{\bar{S}_c} u\nabla'\left(\frac{1}{|\mathbf{r}'-\mathbf{r}|}\right)\cdot d\mathbf{S}', \tag{2.26}$$

where $\Omega^-(S_\varepsilon;\mathbf{r})$ is again the solid angle subtended by S_ε at $\mathbf{r}$. Equation (2.26) is the fundamental equation used to relate surface potentials and fluxes at the surface of a region. As $\mathbf{r}$ varies over the cortex surface, a matrix equation results. These matrix equations are combined for each region to set up the final global matrix equation.

Discretization

As before, we assume that each surface S_s is discretized into E_s elements. Then, for the cortex region, the discretized version of (2.26) becomes

$$\left[4\pi - \Omega^{-}(S_\varepsilon;\mathbf{r})\right]u(\mathbf{r}) = \sum_{j=1}^{E_c}\int_{\Delta_j^c} q\left(\frac{1}{|\mathbf{r}'-\mathbf{r}|}\right)dS' - \sum_{j=1}^{E_c}\int_{\bar{\Delta}_j^c} u\nabla'\left(\frac{1}{|\mathbf{r}'-\mathbf{r}|}\right)\cdot d\mathbf{S}'. \tag{2.27}$$

We now select *two* ensembles of N_c functions each, $\{h_n(\mathbf{r})\}_{n=1}^{N_c}$ and $\{f_n(\mathbf{r})\}_{n=1}^{N_c}$, together with an ensemble of N_c points characterized by the position vectors $\{\mathbf{r}_m\}_{m=1}^{N_c}$, such that

$$h_n(\mathbf{r}_m) = \delta_{nm}, \quad f_n(\mathbf{r}_m) = \delta_{nm}. \tag{2.28}$$

The potential and flux are then estimated with the expansions

$$u(\mathbf{r}) = \sum_{n=1}^{N_c} u_n h_n(\mathbf{r}), \quad q(\mathbf{r}) = \sum_{n=1}^{N_c} q_n f_n(\mathbf{r}). \tag{2.29}$$

As before, we can conceive of a centroid option in which the N_c collocation points are selected at the centroids of the discretization triangles, or of a vertex option in which they are selected at the vertices. In the former case, the potential and flux are assumed constant over each triangle; in the latter they may be assumed to vary linearly. The form of the functions h_n and f_n are exactly as before. Using (2.29) in (2.27) and setting $\mathbf{r} = \mathbf{r}_m$, we get

$$\sum_{n=1}^{N_c} u_n\left[\sum_{j=1}^{E_c}\int_{\bar{\Delta}_j^c} h_n(\mathbf{r}')\nabla'\left(\frac{1}{|\mathbf{r}'-\mathbf{r}_m|}\right)\cdot d\mathbf{S}' + \delta_{mn}\left[4\pi - \Omega^{-}(S_\varepsilon;\mathbf{r}_m)\right]\right]$$

$$= \sum_{n=1}^{N_c} q_n \sum_{j=1}^{E_c}\int_{\Delta_j^c} f_n(\mathbf{r}')\left(\frac{1}{|\mathbf{r}'-\mathbf{r}_m|}\right)dS'. \tag{2.30}$$

As we sequence $\mathbf{r}_m$ through the N_c points, we get an ensemble of N_c equations, and the set of resultant equations (2.30) may be written in matrix form:

$$\mathbf{AU} = \mathbf{CQ}. \tag{2.31}$$

The $N_c \times N_c$ matrices $\mathbf{A}$ and $\mathbf{C}$ have as their terms

$$a_{mn}^{cc} = \left[\sum_{j=1}^{E_c}\int_{\bar{\Delta}_j^c} h_n(\mathbf{r}')\nabla'\left(\frac{1}{|\mathbf{r}'-\mathbf{r}_m|}\right)\cdot d\mathbf{S}' + \delta_{mn}\left[4\pi - \Omega^{-}(S_\varepsilon;\mathbf{r}_m)\right]\right] \tag{2.32a}$$

and

$$c_{mn}^{cc} = \sum_{j=1}^{E_c}\int_{\Delta_j^c} f_n(\mathbf{r}')\left(\frac{1}{|\mathbf{r}'-\mathbf{r}_m|}\right)dS', \tag{2.32b}$$

respectively. Simplified forms of (2.32a) result for the centroid and vertex options, akin to equations (2.21) and (2.22), respectively. Since $\sum_{n=1}^{N_c} h_n(\mathbf{r}) = 1$, from (2.32a) we still have $\sum_{n=1}^{N_c} a_{mn}^{cc} = 0$. In other words, the matrix $\mathbf{A}$ is singular, with eigenvalue zero and associated eigenvector $\mathbf{e}$. Physically, applied to (2.31), this means that knowing all the fluxes at the surface is not sufficient to determine the potentials uniquely. Finally, note that the integrals implicated in the diagonal elements of $\mathbf{C}$ are singular for both the centroid and vertex options, and that again, for the vertex option, $\Omega^{-}(S_\varepsilon;\mathbf{r}_m)$ in (2.32a) is not easily calculated.

A matrix equation similar to (31) can be written for each of the volume conductor regions in Figure 2.1. Where a region contains two bounding surfaces, e.g., the scalp and skull regions, both surfaces must be included. The matrix equations for each region are then combined using the conditions that the potential and the normal component of the current are continuous across regions. This combination is best illustrated with respect to the specific case of the three regions depicted in Figure 2.1. For the cortex (region 3), we have

$$\mathbf{A}_3^3\mathbf{U}_3 = \mathbf{C}_3^3\mathbf{Q}_3^3. \tag{2.33}$$

The superscript indicates the region; the subscript indicates the surface (S_3). For the skull (region 2), we have

$$\begin{bmatrix}\mathbf{A}_2^2 & \mathbf{A}_3^2\end{bmatrix}\begin{bmatrix}\mathbf{U}_2\\ \mathbf{U}_3\end{bmatrix} = \begin{bmatrix}\mathbf{C}_2^2 & \mathbf{C}_3^2\end{bmatrix}\begin{bmatrix}\mathbf{Q}_2^2\\ \mathbf{Q}_3^2\end{bmatrix}. \tag{2.34}$$

Note the partition of the potential and flux matrices and of $\mathbf{A}$ and $\mathbf{C}$ over surfaces S_2 and S_3. Also, while the potential $\mathbf{U}_3$ is the same for both cortex and skull regions, the fluxes $\mathbf{Q}_3^3$ and $\mathbf{Q}_3^2$ at surface S_3 are different. Similarly for the scalp (region 1), we have

$$\begin{bmatrix}\mathbf{A}_1^1 & \mathbf{A}_2^1\end{bmatrix}\begin{bmatrix}\mathbf{U}_1\\ \mathbf{U}_2\end{bmatrix} = \begin{bmatrix}\mathbf{C}_1^1 & \mathbf{C}_2^1\end{bmatrix}\begin{bmatrix}\mathbf{Q}_1^1\\ \mathbf{Q}_2^1\end{bmatrix}. \tag{2.35}$$

Matrix equations (2.33)–(2.35) are easily combined using the continuity of normal current, namely $\sigma_1^{-}\mathbf{Q}_2^1 = -\sigma_2^{-}\mathbf{Q}_2^2$ and $\sigma_2^{-}\mathbf{Q}_3^2 = -\sigma_3^{-}\mathbf{Q}_3^3$, and the combined equation is written as

$$\begin{bmatrix} \mathbf{A}_1^1 & \mathbf{A}_2^1 & \mathbf{0} \\ \mathbf{0} & \mathbf{A}_2^2 & \mathbf{A}_3^2 \\ \mathbf{0} & \mathbf{0} & \mathbf{A}_3^3 \end{bmatrix} \begin{bmatrix} \mathbf{U}_1 \\ \mathbf{U}_2 \\ \mathbf{U}_3 \end{bmatrix} = \begin{bmatrix} \mathbf{C}_1^1 & -\dfrac{\sigma_2^-}{\sigma_1^-}\mathbf{C}_2^1 & \mathbf{0} \\ \mathbf{0} & \mathbf{C}_2^2 & -\dfrac{\sigma_3^-}{\sigma_2^-}\mathbf{C}_3^2 \\ \mathbf{0} & \mathbf{0} & \mathbf{C}_3^3 \end{bmatrix} \begin{bmatrix} \mathbf{Q}_1^1 \\ \mathbf{Q}_2^2 \\ \mathbf{Q}_3^3 \end{bmatrix}. \tag{2.36}$$

In the usual reciprocal problem where current is injected at the external surface, only $\mathbf{Q}_1^1$ is known. Transposing all unknowns to the left-hand side, we have

$$\begin{bmatrix} \mathbf{A}_1^1 & \mathbf{A}_2^1 & \dfrac{\sigma_2^-}{\sigma_1^-}\mathbf{C}_2^1 & \mathbf{0} & \mathbf{0} \\ \mathbf{0} & \mathbf{A}_2^2 & -\mathbf{C}_2^2 & \dfrac{\sigma_3^-}{\sigma_2^-}\mathbf{C}_3^2 & \mathbf{A}_3^2 \\ \mathbf{0} & \mathbf{0} & \mathbf{0} & -\mathbf{C}_3^3 & \mathbf{A}_3^3 \end{bmatrix} \begin{bmatrix} \mathbf{U}_1 \\ \mathbf{U}_2 \\ \mathbf{Q}_2 \\ \mathbf{Q}_3 \\ \mathbf{U}_3 \end{bmatrix} = \begin{bmatrix} \mathbf{C}_1^1 \\ \mathbf{0} \\ \mathbf{0} \end{bmatrix} \left[\mathbf{Q}_1\right], \tag{2.37}$$

where the superscripts on the **Q**s have been dropped, it being understood that all fluxes are outward. The coefficient matrix on the left-hand side is square of dimension $(N_1 + 2N_2 + 2N_3)$, that on the right is not and has dimensions $(N_1 + 2N_2 + 2N_3) \times N_1$.

That the coefficient matrix on the left-hand side of (2.37) is singular is seen by noting that the sum of the first, second, and last column blocks is zero. Therefore, (2.37) does not possess a unique solution, which follows from physical considerations since knowing the injected current on the outer surface S_1 is not sufficient to determine the potential uniquely. The appropriate eigenvector corresponding to the zero eigenvalue is the $(N_1 + 2N_2 + 2N_3) \times 1$ column vector,

$$\mathbf{e} = \left[[\mathbf{e}_1]^T \quad [\mathbf{e}_2]^T \quad \mathbf{0} \quad \mathbf{0} \quad [\mathbf{e}_3]^T \right]^T, \tag{2.38}$$

where $\mathbf{e}_1$, $\mathbf{e}_2$, and $\mathbf{e}_3$ are column vectors of N_1, N_2, and N_3 ones, respectively. Physically, this eigenvector corresponds to the case where the potential is constant everywhere and all the currents are zero. The singular coefficient matrix in (2.37) is deflated as before; i.e., if we denote it by $\mathbf{A}$, the deflated matrix is given by $\mathbf{A}^* = \mathbf{A} + \mathbf{e}\mathbf{p}^T$, with $\mathbf{e}$ given by (2.38) and $\mathbf{p}$ an $(N_1 + 2N_2 + 2N_3) \times 1$ column vector whose first N_1 elements are $1/N_1$ and the rest zeros. The solution of the deflated equation again corresponds to that particular solution of (2.37) such that the sum of the potentials on the outer surface is zero. Once the potential $(\mathbf{U}_3)$ and flux $(\mathbf{Q}_3)$ values are determined on the cortex surface, they are used to find the electric field at a point inside the cortex by taking the negative gradient of (2.25).

2.5 Methods

The conventional and reciprocal approaches, each with centroid and vertex options, were tested using radial and tangential dipoles within a three-concentric-sphere s head model for which analytic solutions are available (Ary et al., 1981). The three spheres of radii 10, 9.2, and 8.7 cm represent the scalp-air (S_1), skull-scalp (S_2), and cortex-skull (S_3) interfaces, respectively. Two sets of conductivities for the scalp, skull, and cortex were used, either 1, 1/80 and 1, or 1, 1/15 and 1, respectively. Two levels of discretization were used: level 1, employing 1572, and level 2, employing 2228 triangles per sphere. These are shown in Figures 2.2a and 2.2b, respectively. The triangles were defined by lines of latitude and longitude, except around the 42 regularly distributed electrode sites, where a higher triangle density was used. No attempt was made to use nearly equilateral triangles, so as to better mimic the real-head situation where such optimization may not be possible. In the conventional centroid (CC) approach, the centroid of the innermost triangle in each high-density region coincided with the electrode position. This centroid was also used for current injection in the reciprocal centroid (RC) approach. With the conventional vertex (CV) approach, one of the vertices of the innermost triangle was selected as the electrode site. A slightly different discretization was used with the reciprocal vertex (RV) approach, where a curvilinear-quadrilateral innermost element was used, with quadratic interpolation for the potential and flux, and with the site of current injection at the center of the quadrilateral (Figures 2.2c and 2.2d). A discretization designated 111 (222) meant the spheres of Figure 2.2a (2b) for S_1, S_2, and S_3, respectively, in the CC, CV, and RC approaches, but those of Figure 2.2c (2.2d) in the RV approach. Radial and tangential dipoles were moved, at eccentricities ranging from 0 to 8.65 cm (0% to 99.4%), along a 45° axis in the first octant (shown dotted in Figure 2.2a). Simulations were also run for dipoles ranging along the x and z axes.

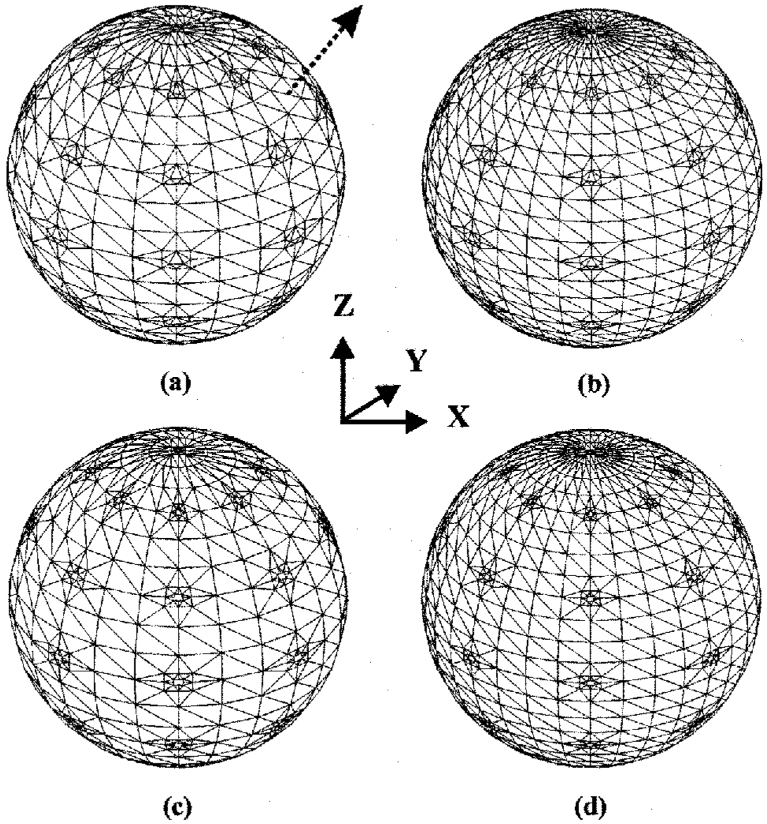

Figure 2.2. (a), (b) Sphere discretizations used with the CC, CV, and RC approaches. There are 1572 triangles per surface in (a) and 2228 in (b). The 45° axis along which the dipole is moved is shown dotted in (a). (c), (d) Sphere discretization with the RV approach. In addition to 42 curvilinear quadrilaterals, there are 1824 triangles in (c) and 2480 triangles in (d). See text for additional details.

The 42 electrode sites meant 41 potential difference measurements, using the electrode at the north pole as a reference. Numerical potential difference computations with each of the four approaches (CC, CV, RC, and RV) were compared with analytic calculations and the relative difference measure (RDM) defined by

$$\mathrm{RDM} = \left(\sum_{i=1}^{41} (u_i^c - u_i^a)^2 \Big/ \sum_{i=1}^{41} (u_i^a)^2 \right)^{1/2}, \tag{2.39}$$

where u_i^c and u_i^a denote the computed and analytic potentials, respectively, was used as an index of computational accuracy.

2.6 Results

Results are only shown for the dipole ranging along the 45° axis. Figure 2.3a shows the RDM variation for the conventional approach with both centroid (CC) and vertex (CV) options and a relative skull conductivity of 1/80. A 111 discretization was used for CC and a 222 discretization for CV, so that the number of unknown potentials N remained somewhat comparable. For both radial and tangential dipoles, the CC option yielded lower RDM values than the CV option at eccentricities less than 86%. Above this eccentricity, RDM values for both CC and CV options exhibited large errors, rendering a choice difficult. Figure 2.3b depicts the results with a relative skull conductivity of 1/15. Now the CV option yields better results than the CC option for eccentricities up to 75%, due to significantly lowered RDMs with the former and slightly increased RDMs with the latter. Above this eccentricity, large RDM values were again noted, rendering a choice difficult.

Results for the reciprocal approach with both centroid (RC) and vertex (RV) options are depicted in Figures 2.4a and 2.4b for relative skull conductivities of 1/80 and 1/15, respectively. Again a 111 discretization was used for RC and a 222 discretization for RV to facilitate their comparison. Note, however, that both RC and RV approaches solve for almost twice as many unknowns as their CC and CV counterparts of Figure 2.3. In contrast to Figure 2.3, the skull conductivity has a much smaller effect on the RDM curves. With both skull conductivities, the RC option performed better than RV, except for highly eccentric tangential dipoles where the RV option was better. However, at high eccentricities, large RDM values were noted for both options.

If we assume a relative skull conductivity of 1/15, then the CV option is the most accurate. Where the reciprocal approaches are undeniably superior is their stability in the face of skull conductivity alterations. Since others (Fletcher et al., 1995; Schlitt et al., 1995; Ferguson and Stroink, 1997) have shown that some variability in the RDM curves is to be expected as the axis along which the dipole is moved changes, we repeated the above curves for dipoles moving along the x and z axes. Now the dipole approaches an electrode site, and errors at this electrode can greatly influence the RDM curves. While some quantitative variation was noted, qualitatively the above findings remained

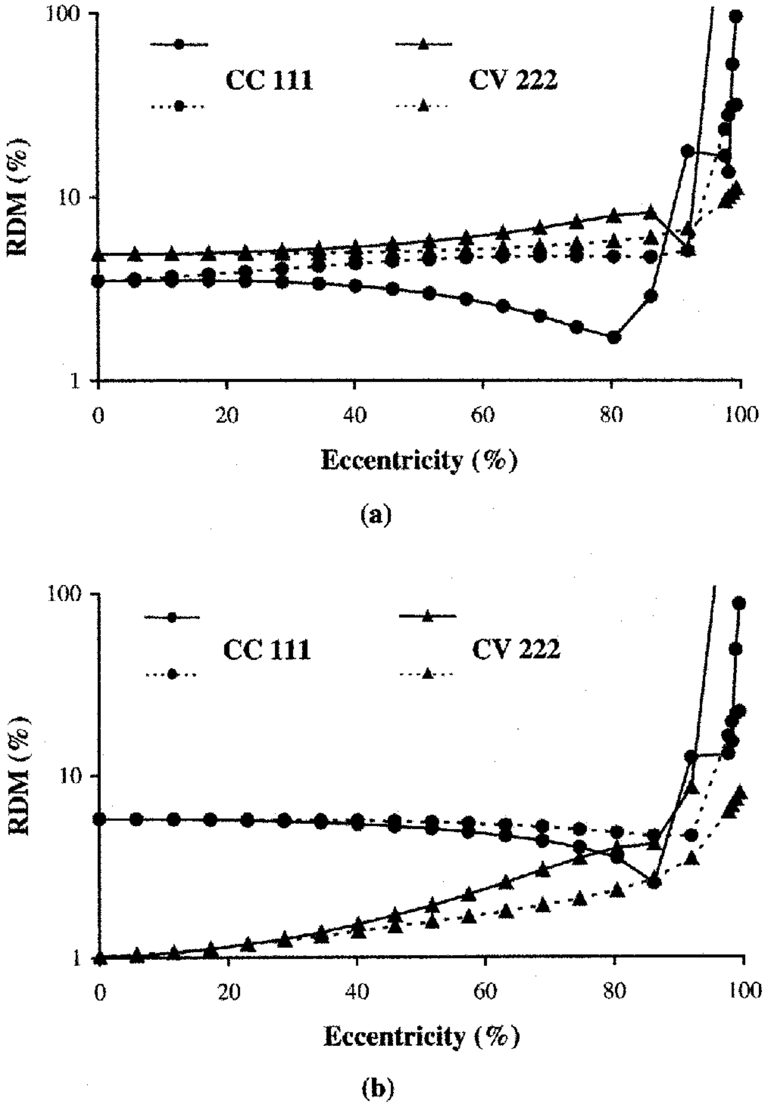

Figure 2.3. Relative difference measures plotted against dipole eccentricity for radial (solid line) and tangential (dotted line) dipoles. Results for both CC (circles) and CV (triangles) approaches are depicted. Relative skull conductivity was 1/80 in (a) and 1/15 in (b).

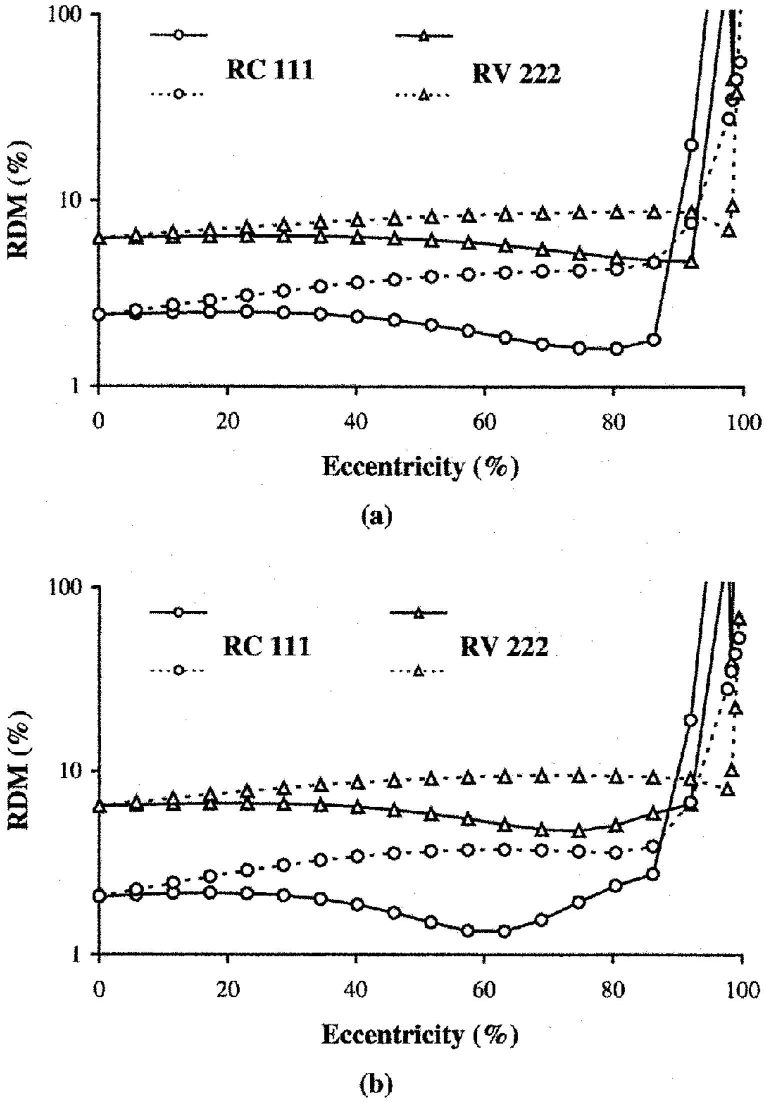

Figure 2.4. Relative difference measures plotted against dipole eccentricity for radial (solid line) and tangential (dotted line) dipoles. Results for both RC (circles) and RV (triangles) approaches are depicted. Relative skull conductivity was 1/80 in (a) and 1/15 in (b).

unchanged.

We found that CC, CV, RC, and RV options all improved with increasing discretization. Improving the auto solid angle computation in the CV option with either the Heller (1990) or the Wischmann et al. (1996) correction had negligible effect on our RDM values, thereby suggesting that our approximation for the auto solid angle was sufficiently accurate at the discretization levels used. Straightforward implementation of the Heller (1990) and Wischmann et al. (1996) corrections is not possible with the RV option owing to the presence of quadrilaterals in the mesh.

2.7 Discussion

Our results implying that the CC option is superior to the CV option with a relative skull conductivity of 1/80 except at high eccentricities (Figure 2.3a) confirms the observations of others (Schlitt et al., 1995; Mosher et al., 1999b). While Ferguson and Stroink (1997) suggested that overall the CV option is superior, their study was limited to single-surface volume conductors of spherical, spheroidal, and cubic shapes. In effect, their single surface corresponds to the innermost sphere in the three-concentric-spheres model, and for the innermost sphere we, as well as others (Schlitt et al., 1995), have found that the CV option yields lower errors than the CC option.

An important finding of our study was the greatly improved accuracy on the *outer* sphere of the CV option and the diminished accuracy of the CC option, with an increased skull conductivity (Figure 2.3b). An improved accuracy is to be expected with increased skull conductivity as the correction term to the isolated brain potentials becomes more precise. The unexpected diminished accuracy of the CC option with increased skull conductivity was traced to the larger magnitude and greater spatial variability of the surface potential on the scalp, rendering the interpolation of a constant potential on each triangle face less valid. Thus, assuming that the higher skull conductivity is the correct value, the CV option is to be preferred over the CC option. Since more accurate computation of the auto solid angle did not further improve the CV option, it would appear that the best way to achieve this improvement may be to use an even higher order interpolation (Mosher et al., 1999b; Pullan, 1996; Fischer et al., 1999; Gençer and Tanzer, 1999; Frijns et al., 2000). This would achieve a more accurate match of the variation in potential over the surface.

The change in RDM curves with skull conductivity in the conventional approach (Figure 2.3) must be contrasted with the relative invariance of the RDM curves in the reciprocal approach (Figure 2.4). Inherently, it would appear that the errors associated with the reciprocal approach adjust more or less in proportion to the increase in scalp potential caused by the increased conductivity. Between RC and RV options, while the RC option offers lower errors for all but the most eccentric dipoles, it is difficult to imagine any significant improvement in this option for eccentric dipoles. For these dipoles, choosing the potential and flux constant over each triangle constitutes a severe limitation, and we are therefore left with just the RV option where linear interpolation is used.

Of some concern are the somewhat large RDM values obtained with the RV approach, since Fletcher et al. (1995), using a normalized median-error measure over all electrodes, reported much smaller numbers for the RV approach. We found that the Fletcher et al. (1995) error measure generally resulted in error values that were, on the average, half those of the more usual RDM measure and considerably less than half for highly eccentric dipoles. This latter fact is easy to understand, since for eccentric dipoles only the few electrodes close to the dipole exhibit large errors and the median-error measure reflects the lower error at one of the other electrode pairs. Real reductions in our RDM values for the RV approach may be possible by better evaluation of the auto solid angle term, by using curvilinear quadrilaterals and quadratic interpolation throughout rather than just over the electrode sites, or by using a new reciprocal solution (Riera and Fuentes, 1998) in terms of current fluxes at the BEM elements that gives the electric field at the dipole site without recourse to the gradient of the potential.

There is, at present, considerable interest in using the reciprocal approach to obtain the forward problem transfer matrix when performing inverse dipole solutions (Laarne et al., 2000; Weinstein et al., 2000; Vanrumste et al., 2000), despite its larger coefficient matrix sizes. As Fletcher et al. (1995) have pointed out, the reciprocal approach in effect transfers the source currents to the known positions of the current injecting electrodes, and, as we have done, the region around these electrodes can then be selectively discretized with higher resolution for improved lead vector accuracy. On the other hand, in the conventional approach, it is the region near the source dipole that needs to be discretized with higher resolution, and the position of this source dipole is not known *a priori*, thereby mandating a fine discretization throughout the cortex surface. A second advantage might be the invariance of the reciprocal approach's RDM measure with skull conductivity values. It remains to be seen whether these advantages can be exploited to yield more accurate inverse dipole computations.

Chapter 3 Conventional and Reciprocal Approaches to the Inverse Dipole Localization Problem of Electroencephalography[3]

Stefan Finke[1], Ramesh M. Gulrajani[1], and Jean Gotman[2]

[1]*Institut de génie biomédical, Faculté de médecine, Université de Montréal, Montréal, Québec, Canada*
[2]*Montreal Neurological Institute, McGill University, Montréal, Québec, Canada*

Published in IEEE Transactions on Biomedical Engineering, vol. 50, no. 6, June 2003, pp. 657-666. Manuscript received on June 26, 2002; manuscript accepted on December 8, 2002.

3.1 Preface

This work was conducted at the Institute of Biomedical Engineering, Faculty of Medicine, University of Montreal, in Montreal, Quebec, Canada from 2001 to 2003. Note that during this period research was conducted on a part-time basis in the context of an M.D./Ph.D. program through the University of Montreal. Original programs were written by Stefan Finke in Fortran 90 and run through the high-performance computing (HPC) facilities of the *RQCHP* (*Réseau québécois de calcul de haute performance*). Text and figures represent the combined efforts of all authors. Source code is available on request via e-mail at . Financial support was provided by the Canadian Institutes of Health Research (CIHR). The work of Stefan Finke was also supported in

---

[3] © 2003 IEEE

Reprinted, with permission, from S. Finke, R. M. Gulrajani, J. Gotman, Conventional and reciprocal approaches to the inverse dipole localization problem of electroencephalography, IEEE Transactions on Biomedical Engineering, June 2003.

part by an M.D./Ph.D. Scholarship from the CIHR and in part by the *FRQS* (*Fonds de recherche du Québec – Santé*). Preliminary versions of portions of this work have been previously published as short conference proceedings (Finke et al., 2001; Gulrajani et al., 2001; Finke et al., 2002; Finke et al., 2003a).

3.2 Abstract

Forward transfer matrices relating dipole source to surface potentials can be determined via conventional or reciprocal approaches. In numerical simulations with a triangulated boundary-element three-concentric-spheres head model, we compare four inverse electroencephalogram (EEG) solutions: those obtained utilizing conventional or reciprocal forward transfer matrices, relating in each case source dipole components to potentials at either triangle centroids or triangle vertices. Single-dipole inverse solutions were obtained using simplex optimization with an additional position constraint limiting solution dipoles to within the brain region. Dipole localization errors are presented in all four cases, for varying dipole eccentricity and two different values of skull conductivity. Both conventional and reciprocal forward transfer matrices yielded inverse dipole solutions of comparable accuracy. Localization errors were low even for highly eccentric source dipoles on account of the nonlinear nature of the single-dipole solution and the position constraint. In the presence of Gaussian noise, both conventional and reciprocal approaches were also found to be equally robust to skull conductivity errors.

Keywords: Boundary element method, dipole source model, electroencephalography, inverse problem, reciprocity.

3.3 Introduction

There has been much recent interest in a “reciprocal” approach to the inverse problem of electroencephalography, whereby the forward transfer coefficients relating the dipole source to the resulting potentials at surface electrode sites on the scalp are obtained via a reciprocal approach (Fletcher et al., 1995). The reciprocal approach first entails calculating the electric field that results at the dipole location within the brain, due to current injection and withdrawal at the surface electrode sites. The forward transfer coefficients are then simply obtained from the scalar product of this electric field and the dipole moment. One advantage of the reciprocal approach is that, if increased precision in the forward transfer coefficients is required, the volume conductor discretization can be refined exclusively at the known scalp electrode sites. With a conventional transfer-coefficient calculation, in which surface potentials are calculated from the dipole source via an integral equation, increased precision demands that the volume conductor discretization be refined near the dipole position. Unfortunately, this position is not known *a priori* in the inverse problem. Thus, interest in the reciprocal approach has been sparked by this possibility of increased precision in the forward transfer coefficients and therefore, presumably, more accurate inverse dipole solutions. Examples of inverse electroencephalogram (EEG) solutions obtained with reciprocal transfer coefficients employing finite-difference (Laarne et al., 2000; Vanrumste et al., 2000; Vanrumste, 2001; Vanrumste et al., 2001) and finite-element (Weinstein et al., 2000) volume conductor discretizations have recently been published. However, in a study employing locally refined boundary-element meshes near the surface electrodes, we found no advantage in precision with reciprocally computed forward transfer coefficients over conventionally computed ones that used the same locally refined mesh (Finke and Gulrajani, 2001). Indeed, for centric dipoles, conventionally computed transfer coefficients were sometimes more accurate, whereas for highly eccentric dipoles both conventional and reciprocal transfer coefficients exhibited large errors. What we did find was a greater invariance of the precision of reciprocally computed transfer coefficients as skull conductivity was altered. In other words, reciprocally computed transfer coefficients were more robust to skull conductivity alterations. This paper examines the single-dipole *inverse* solutions obtained using these conventional and reciprocal boundary-element transfer coefficients, for both centric and highly eccentric dipole sources. The robustness of these inverse solutions to skull conductivity errors is also studied. Preliminary versions of portions of this work have been published before as short conference proceedings

(Finke et al., 2001; Gulrajani et al., 2001; Finke et al., 2002).

3.4 Methods

3.4.1 Forward Solutions

In certain brain events such as epileptic spikes, the early stages of an epileptic seizure, or evoked potentials, a single current dipole may be an adequate model for the electrical source. Assuming that a particular neural source can be represented by a current dipole source $\mathbf{J}_s$ at a given location in the brain volume conductor, the potential difference between any two given scalp electrodes A and B, $u_{AB} \equiv u_A - u_B$, may be expressed as

$$u_{AB} = \mathbf{L} \cdot \mathbf{J}_s \tag{3.1}$$

where $\mathbf{L}$ is a so-called "lead vector."

In the conventional approach to the forward problem, the lead vector is obtained by calculating the potentials u_{AB} corresponding to unit dipoles in the x, y, and z directions at the dipole position under consideration. The three potential values determined in this way then yield the individual lead vector components L_x, L_y, and L_z, respectively. For accurate computations, however, the low conductivity of the skull mandates the use of a two-step "isolated-problem" implementation (Hämäläinen and Sarvas, 1989) whereby potentials are first computed assuming a skull of zero conductivity following which, in a second step, these "isolated" potentials are corrected for the real skull conductivity. Also, a simple matrix deflation technique (Lynn and Timlake, 1968) is needed in these potential computations to counter the singular matrix that results on account of the indeterminacy of the potential to within a constant value.

The alternative reciprocal determination of $\mathbf{L}$ invokes Helmholtz' principle of reciprocity which states that $\mathbf{L} = -\mathbf{E}$, where $\mathbf{E}$ is the electric field or "lead field" at the dipole position resulting from a unit current injected into the volume conductor at electrode A and withdrawn at electrode B. The reciprocal or "lead-field" approach to the forward problem, thus, entails first calculating $\mathbf{E}$ in the volume conductor which is now assumed passive (containing no current dipole sources), and then the potential u_{AB} which is now given by $u_{AB} = -\mathbf{E} \cdot \mathbf{J}_s$. Matrix deflation is also required in the reciprocal approach when computing $\mathbf{E}$.

3.4.2 Inverse Solution

Let $\hat{\mathbf{U}}$ be the $N \times 1$ column matrix containing the measured potential differences $\hat{u}_i$ between the N surface electrode pairs on the scalp. For a particular *fixed* trial dipole location, $\mathbf{T}$ is defined as the $N \times 3$ transfer matrix whose rows contain the individual lead vector components L_x, L_y, and L_z for each of the N electrode pairs considered. These individual lead vector components may have been obtained by either the conventional or the reciprocal approach to the forward problem. From (3.1), the theoretical potential differences $\mathbf{U}$, where $\mathbf{U}$ is the corresponding $N \times 1$ matrix of theoretical potentials u_i, can be calculated via the matrix relation $\mathbf{U} = \mathbf{T}\mathbf{J}_s$. These theoretical potentials are more appropriately termed "numerical" potentials, and henceforth the term numerical will be used to denote them. The best trial dipole at the chosen location can then be estimated from a standard linear least-squares minimization of the sum-squared residual

$$R = \sum_{i=1}^{N} \left(\hat{u}_i - u_i\right)^2 = \left(\hat{\mathbf{U}} - \mathbf{U}\right)^T \left(\hat{\mathbf{U}} - \mathbf{U}\right) \tag{3.2}$$

where the superscript T denotes the matrix transpose. The best moment of this trial dipole is given by the so-called "normal equations" (Forsythe and Molar, 1967)

$$\mathbf{J}_\mathbf{s} = \mathbf{T}^{+}\hat{\mathbf{U}} \tag{3.3}$$

where $\mathbf{T}^{+} = \left(\mathbf{T}^T\mathbf{T}\right)^{-1}\mathbf{T}^T$ is known as the "Moore-Penrose pseudoinverse" of the matrix $\mathbf{T}$. Using this value for $\mathbf{J}_\mathbf{s}$, the residual R can be written as

$$R = \hat{\mathbf{U}}^T\left[\mathbf{I} - \mathbf{T}\mathbf{T}^{+}\right]\hat{\mathbf{U}} \tag{3.4}$$

with $\mathbf{I}$ denoting the $N \times N$ identity matrix. The well-known simplex algorithm can now be used to select the best *location* for the trial dipole by minimizing the above expression for the sum-squared residual (He et al., 1987). In practice, we did not minimize R but rather the relative-difference measure (RDM) given by

$$\text{RDM} = \sqrt{\frac{\sum_{i=1}^{N}\left(\hat{u}_i - u_i\right)^2}{\sum_{i=1}^{N}\left(\hat{u}_i\right)^2}} = \sqrt{\frac{\hat{\mathbf{U}}^T\left[\mathbf{I} - \mathbf{T}\mathbf{T}^{+}\right]\hat{\mathbf{U}}}{\hat{\mathbf{U}}^T\hat{\mathbf{U}}}}. \tag{3.5}$$

This not only renders the function to be minimized dimensionless, but it also reduces the magnitude range of this function for different locations of the source dipole. Consequently, it makes it easier to select a stopping point for the simplex algorithm, i.e., when the difference in RDM between successive iterations drops to below a certain *fixed* tolerance, that is applicable for all dipole locations. Note that the simplex algorithm only searches for the three location coordinates of the dipole since the dipole moment is always given by (3.3). Each iteration entails determining **T** (and hence $\mathbf{T}^{+}$) corresponding to the dipole location under test, prior to calculating the RDM. This determination of **T** may be either by conventional or reciprocal approaches, and correspondingly we get either a conventional or a reciprocal inverse solution. Also, in order to restrict the search to within the brain region, a large constant is added to RDM whenever the trial location is selected outside this region. Thus, any trial location chosen within the skull or scalp is corrected in the next simplex iteration to fall within the brain region.

3.4.3 Three-Concentric-Spheres Head Models

In order to test conventional and reciprocal inverse EEG solutions, the three-concentric-spheres head model was employed. Two different sets of relative conductivities were used for the scalp, skull, and cortex: 1, 1/80, 1 and 1, 1/15, 1, respectively. The first set corresponds to the values usually employed for these conductivities, the second reflects the higher skull conductivity suggested by more recent work (Oostendorp et al., 2000). Sphere radii were 10, 9.2, and 8.7 cm.

Next, the spheres were discretized into planar triangles employing regularly spaced lines of latitude and longitude. Forty-two electrode sites were selected on the outermost (scalp) sphere at the intersections of these lines of latitude and longitude. A higher triangle density was then introduced around these 42 sites (Figure 3.1(a) and (b)),

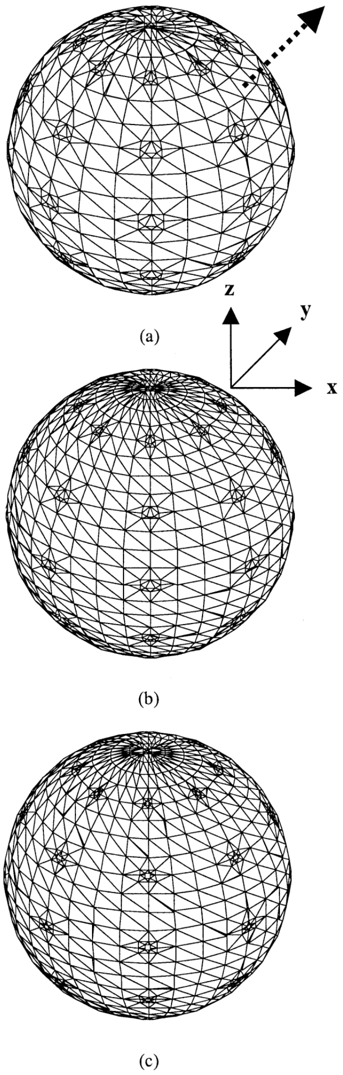

Figure 3.1. Level 1 sphere discretization is shown in (a), and level 2 sphere discretizations are shown in (b) and (c). There are 1572 triangles per sphere in (a), and 2228 triangles per sphere in (b). In addition to the 42 curvilinear quadrilaterals, there are 2480 triangles in (c). The CC and RC approaches use sphere (a), the CV approach uses sphere (b), and the RV approach sphere (c). The axis along which the source dipole is moved is shown by the arrow in (a). To give a quantitative idea of the discretizations, at the equator in (c), the quadrilaterals are of 4.3-mm width and 2.9-mm height for the outermost sphere of radius 10 cm, 4.0-mm width and 2.7-mm height for the middle sphere of radius 9.2 cm, 3.8-mm width and 2.5-mm height for the innermost sphere of radius 8.7 cm. Coordinate axes are as shown.

not only on the outermost sphere but also on the two inner ones.

Forward transfer matrices can be computed between source dipole and potentials at triangle centroids, or between source dipole and potentials at triangle vertices. Accordingly, we obtain four possibilities for these forward transfer matrix determinations, either a conventional centroid (CC) or a conventional vertex (CV) approach, or alternatively, a reciprocal centroid (RC) or reciprocal vertex (RV) approach. With the two centroid approaches, the potential was assumed constant across each triangle. With the vertex approaches, a linear variation in potential was assumed. In the CC approach, the centroid of the innermost triangle in each high density region coincided with the electrode position. With the CV approach, one of the vertices of the innermost triangle was selected as the electrode site. In the reciprocal approaches, these electrode sites are to be used for current injection. Thus, in the RC approach, the centroids of the innermost triangles were used for reciprocal current injection and withdrawal. Because of the difficulty of calculating the current distribution following injection at a triangle vertex, a slightly different discretization was used with the RV approach. A curvilinear quadrilateral innermost element was used, with quadratic interpolation of the potential for this element alone, and with the site of current injection at the center of the quadrilateral (Figure 3.1(c)).

Two levels of discretization were used, level 1 employing 1572 and level 2 employing 2228 triangles per sphere. Level 1 was used for the CC and RC approaches (Figure 3.1(a)), but level 2 was used for the CV and RV approaches (Figure 3.1(b) and (c), respectively). This is because in a triangular discretization the number of vertices is approximately half the number of triangles, and this permits using a finer discretization for the vertex approach while keeping the same number of unknown potentials. On account of the presence of the quadrilaterals at each electrode site, the level 2 discretization used for the RV approach had 2480 triangles and 42 curvilinear quadrilaterals (Figure 3.1(c)). The three discretization meshes used by us and depicted in Figure 3.1 are, in essence, a means of approximately leveling the playing field for all four forward problem approaches. Further details of the numerical methods used by us to compute the **T** matrices for all four approaches are described in (Finke and Gulrajani, 2001).

3.4.4 Simplex Minimization

The correct forward potentials, due to a unit current dipole in this three-concentric-spheres volume conductor, were calculated via analytic equations (Ary et al., 1981). The equations yield exact potentials at triangle vertices, but not at triangle centroids whose "correct" potentials were taken to be the mean of the three corresponding triangle vertices. The electrode at the north pole on the outermost sphere was used as the reference electrode, and accordingly 41 correct analytic potential differences were obtained. The source dipole was assumed to move along the diagonal axis shown in Figure 3.1(a). This axis was chosen to intersect the outer sphere approximately equidistant from four contiguous electrodes. Dipole orientations were either radial (along this axis) or tangential (pointing downwards in the vertical plane containing this axis). Dipole positions ranged from zero to a maximum of 8.5 cm (corresponding to 97.7% of the radius of the innermost sphere). A few simulations were also run for radial and tangential dipoles along the x and z axes (Figure 3.1).

The analytic potentials were initially computed assuming no noise and then perturbed by the addition of 10% or 20% white Gaussian noise (corresponding to a signal-to-noise ratio of 20 db and 13.98 db, respectively). These noise levels were selected as being representative of the noise to be expected during EEG measurement (for single epileptic spikes, the noise level typically equals 20%, but for averaged spikes, it typically equals 10%). These noisy potentials then served as the input measured potentials $\hat{\mathbf{U}}$ for the inverse solution. For each inverse solution, ten simplex minimizations with different randomly chosen starting points were run, with stopping points either when the difference in RDM between successive simplex iterations dropped below 0.0001, or following a maximum of 1000 iterations. An individual simplex minimization can, therefore, return a result of either convergence or of nonconvergence (having reached the maximum of 1000 iterations). The computed dipole was obtained from the simplex with the least RDM among the set of converging simplexes. The position error (in cm) between the correct source dipole and this computed dipole was used as an index of precision for each of the four approaches. However, the amplitude error (absolute difference from unity) and orientation error (in degrees) of the solution dipole, which also contribute to the overall RDM for a given approach, were calculated as well.

A final set of simulations was run to test the robustness of the inverse solution to incorrect assumed values for the relative skull conductivity. For this set of simulations, all inverse solutions were run using a transfer matrix **T** calculated assuming a relative skull conductivity of 1/15. The input matrix $\hat{\mathbf{U}}$ to this inverse solution was, however, calculated from the analytic potentials assuming skull conductivities of either $(1/15)+25\%$ or $(1/15)-25\%$. These input potentials were in the first instance noiseless, and in the second instance contaminated with 10% and 20% noise. Simplex minimization was as before.

3.5 Results

Figure 3.2 summarizes the results of our earlier study (Finke and Gulrajani, 2001) regarding the accuracy of the forward transfer coefficients computed with each of the four approaches CC, CV, RC, and RV, and this for the two values of relative skull conductivity. The abscissa denotes the dipole eccentricity, and the ordinate the RDM, again given by the first equality in (3.5), but with $\hat{u}_i$ now denoting the noiseless analytic potentials and u_i the numerically computed forward potentials. The salient points are the invariance of the RC and RV curves to changes in skull conductivity, and the large RDM values at high eccentricities.

Figure 3.3 depicts the position error of the inversely computed dipole when computed from the noiseless analytic potentials. These curves are an expression of the extent to which the errors in the forward transfer coefficients of Figure 3.2 impact on the inverse problem. Surprisingly, the position errors are small (< 0.45 cm), even for highly eccentric dipoles where the forward transfer coefficients, particularly for radial dipoles, exhibit errors of greater than 100%. There is little to choose between the four approaches CC, CV, RC, and RV. Note, however, the drop in position error for all four approaches when the relative skull conductivity is increased from 1/80 to 1/15. Adding 20% noise to the analytic potentials prior to performing the inverse computations increases the position

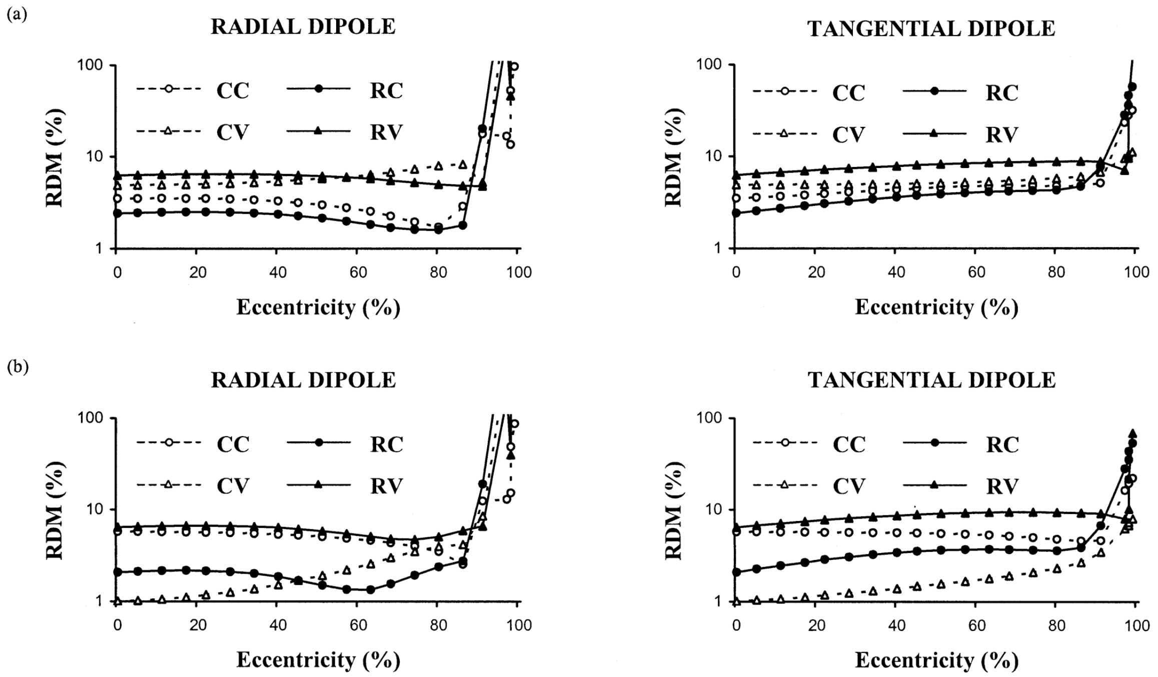

Figure 3.2. RDM of the forward problem versus dipole eccentricity for radial and tangential dipoles (maximum eccentricity is 8.65 cm). Relative skull conductivity is 1/80 in (a) and 1/15 in (b). Results for conventional approaches (CC and CV) are shown using dashed lines and those for reciprocal approaches (RC and RV) are shown using solid lines. The CC and RC approaches (circles) use level 1 discretizations for all three spheres, while the CV and RV approaches (triangles) use level 2 discretizations for all spheres.

error (Figure 3.4). Nevertheless, we see that these position errors are still limited. Radial dipoles exhibited a maximum error of 1.14 cm for centric dipoles, tangential dipoles a maximum error of 1.41 cm for dipoles of intermediate eccentricity. Errors for highly eccentric dipoles (eccentricity of 97.7%) were less than 0.76 cm. These unexpectedly good results were traced to an inherent robustness of the position error with the single-dipole inverse solution to errors in the forward transfer matrix. A secondary effect, seen only for highly eccentric tangential dipoles, is due to the position constraint under conditions when this constraint is *active*, i.e., when an inverse dipole is placed at the brain-skull interface due to this constraint, thereby limiting the position error and compensating for the inaccuracy of the forward transfer matrix. Dipole amplitude and

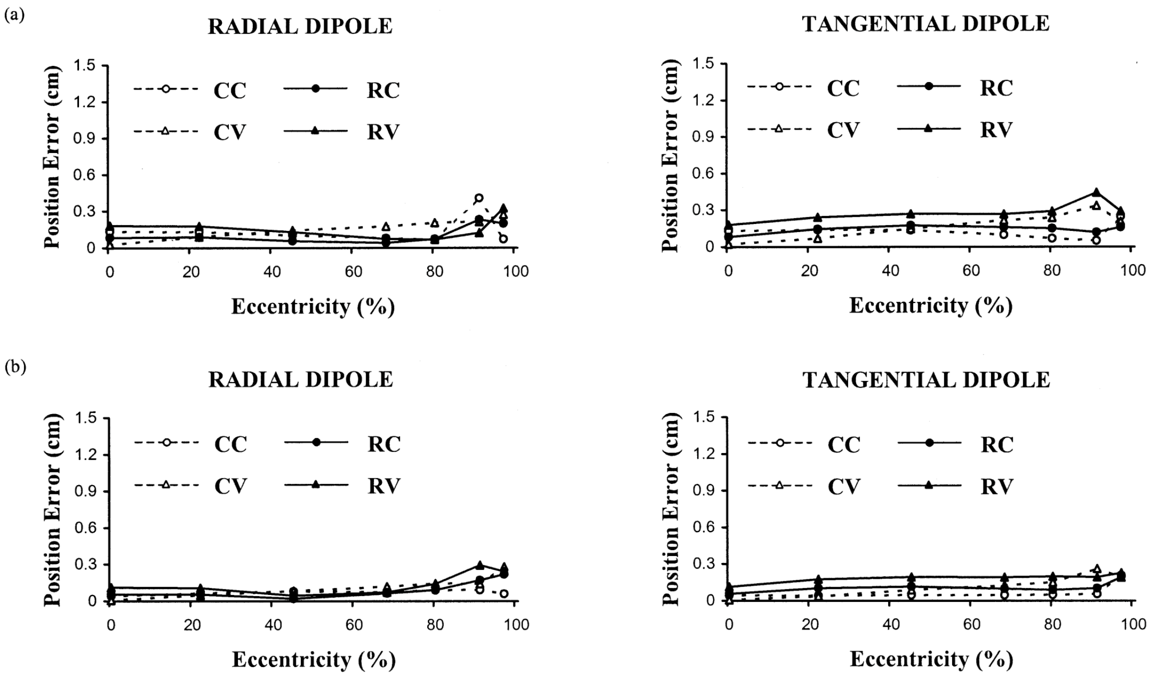

Figure 3.3. Dipole position error versus dipole eccentricity for radial and tangential dipoles in the absence of measurement noise (maximum eccentricity is 8.5 cm). Relative skull conductivity is 1/80 in (a) and 1/15 in (b). Results for conventional approaches (CC and CV) are shown using dashed lines and those for reciprocal approaches (RC and RV) are shown using solid lines. The CC and RC approaches (circles) use level 1 discretizations for all three spheres, while the CV and RV approaches (triangles) use level 2 discretizations for all spheres.

orientation errors, however, do increase at high eccentricities and we show these for the case of 20% noise in Figures 3.5 and 3.6, respectively. Results for 0% and 10% noise (not shown) fell below the values for 20% noise. All of the above findings remainedqualitatively the same for dipoles positioned along the *x* and *z* axes.

While our preliminary work suggested that tangential-dipole position errors with the RV approach are resistant to ±10% changes in skull conductivity (Finke et al., 2002), this invariance to skull conductivity errors does not hold for radial dipoles nor for the RC approach. It does not hold under any circumstance when 10% or 20% measurement noise is present. Figure 3.7 illustrates the position errors, corresponding to ±25% skull conductivity errors and 20% measurement noise, for a radial dipole, and Figure 3.8 those

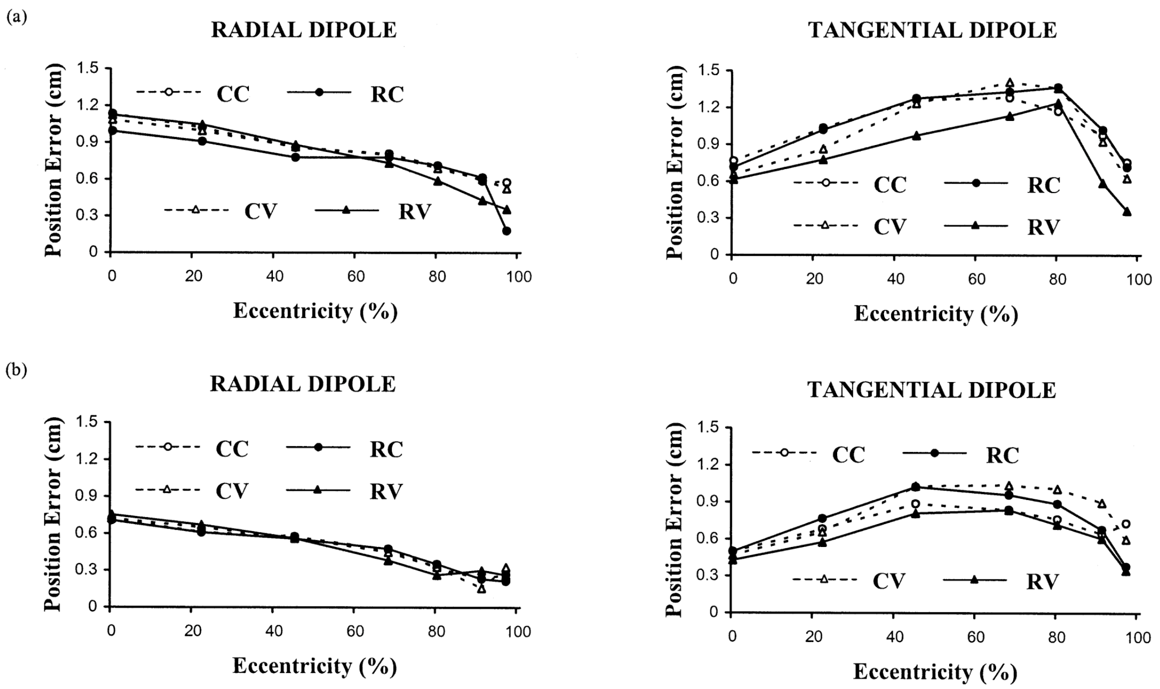

Figure 3.4. Dipole position error versus dipole eccentricity for radial and tangential dipoles in the presence of 20% noise (maximum eccentricity is 8.5 cm). Relative skull conductivity is 1/80 in (a) and 1/15 in (b). The format is the same as in Figure 3.3.

for a tangential dipole. Clearly, in practice, the invariance in precision of reciprocal transfer matrices to conductivity changes (Figure 3.2) does not translate to a greater invariance of position errors with reciprocal approaches than with conventional ones. On the whole, large conductivity errors, with or without the presence of measurement noise, affect the position errors equally for all four approaches, and again there is little to choose between the approaches.

The number of convergent simplex solutions for each approach was noted. Results for radial and tangential dipoles at all eccentricities (seven, including the centric dipole), for both relative skull conductivities (1/80 and 1/15), and for zero, 10% and 20% noise are all lumped together. Also included were solutions when an erroneous conductivity was assumed $(\sigma_{\text{skull}} = (1/15) \pm 25\%)$, for a total of 168 inverse dipole solutions for each of the four approaches. Each inverse dipole solution implied ten simplex trials, so that in all 1680 simplex trials were performed for each approach. Of

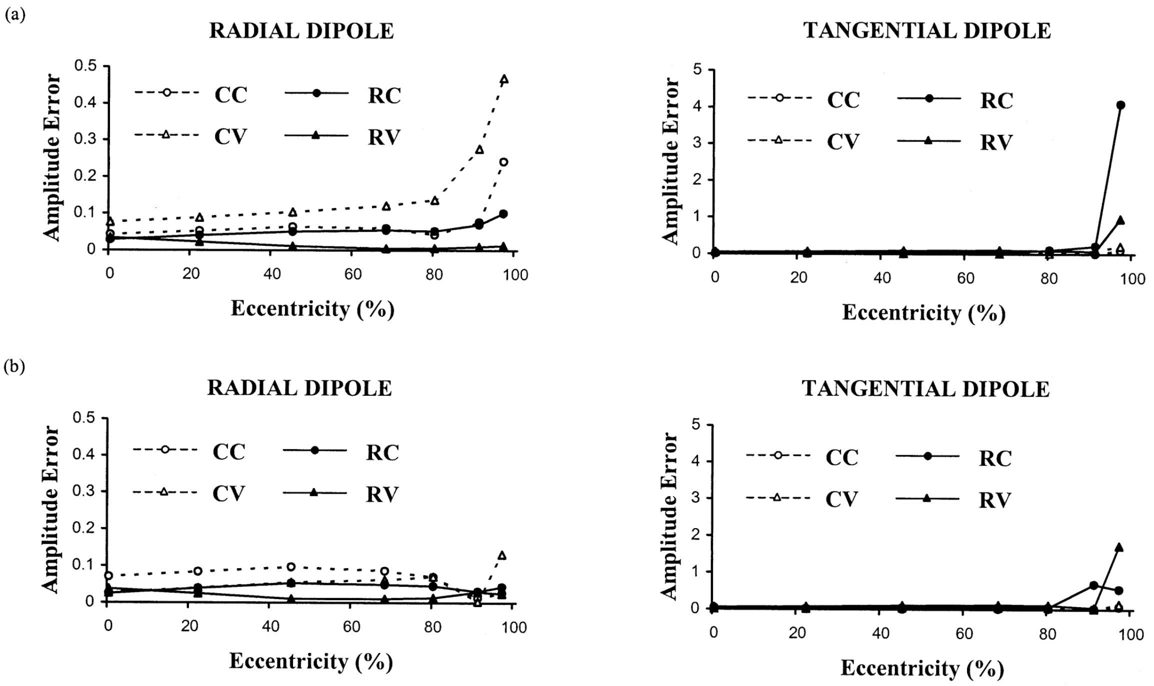

Figure 3.5. Dipole amplitude error versus dipole eccentricity for radial and tangential dipoles in the presence of 20% noise (maximum eccentricity is 8.5 cm). Relative skull conductivity is 1/80 in (a) and 1/15 in (b). The format is the same as in Figure 3.3. Note, however, that the graphs for radial and tangential dipoles have different vertical scales.

these simplex trials, 86.25% converged in less than 1000 iterations for the CC approach, 85.83% for the CV approach, 82.38% for the RC approach, and 90.48% for the RV approach. In every inverse dipole solution, at least one of the ten simplex trials converged in less than 1000 iterations. It was found that convergence was easier in the *presence* of measurement noise. Not only did more of the ten simplex trials converge, but they also converged in roughly half the number of iterations.

A very important question is that of convergence to the correct solution. Amongst the converging simplexes for each of the 168 inverse dipole solutions, we have implicitly assumed that the simplex with the least RDM yielded the correct solution, and this for all four approaches. In other words, a global minimum in RDM always corresponded to the correct solution. To test the validity of this assumption, for each of the 168 inverse dipole solutions in each approach, we plotted a position error versus RDM curve for the set of

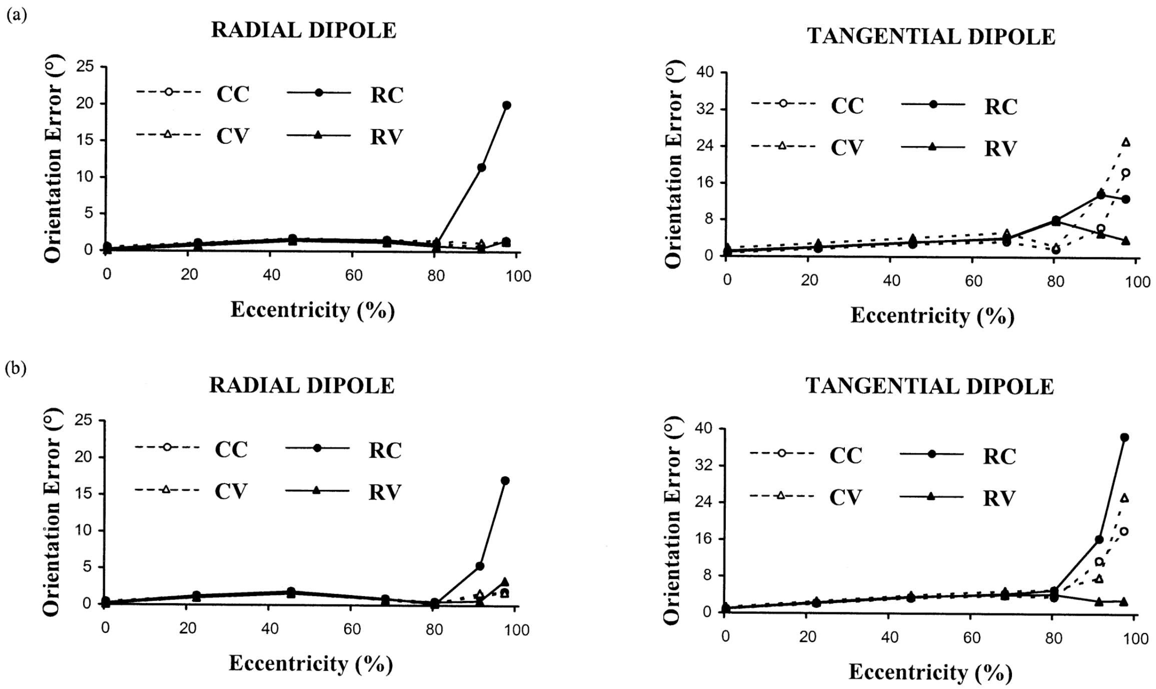

Figure 3.6. Dipole orientation error versus dipole eccentricity for radial and tangential dipoles in the presence of 20% noise (maximum eccentricity is 8.5 cm). Relative skull conductivity is 1/80 in (a) and 1/15 in (b). The format is the same as in Figure 3.3. Note, however, that the graphs for radial and tangential dipoles have different vertical scales.

converging simplexes. A typical example of these curves is shown in Figure 3.9, which gives the ten converging simplex solutions for the case of a tangential dipole at an eccentricity of 8.5 cm in a three-spheres model with relative skull conductivity of 1/80. The inverse solution was computed with the CV approach, in the presence of 20% noise but with no error in skull conductivity. We see that the simplexes fall into three distinct clusters, A, B, and C, respectively, easily identifiable visually on the basis of RDM and position error values. Cluster C, which consists of a single converging simplex, is obviously incorrect and corresponds to convergence to a local minimum. The position error corresponding to the simplex with minimum RDM (see magnified image of Cluster A in Figure 3.9) is 6.27 mm. Clusters A and B, the latter with a single point, correspond to solutions found on either side of the source dipole. In fact, the single solution in cluster B yields a position error of 6.17 mm, which is 0.1 mm better than the minimum RDM

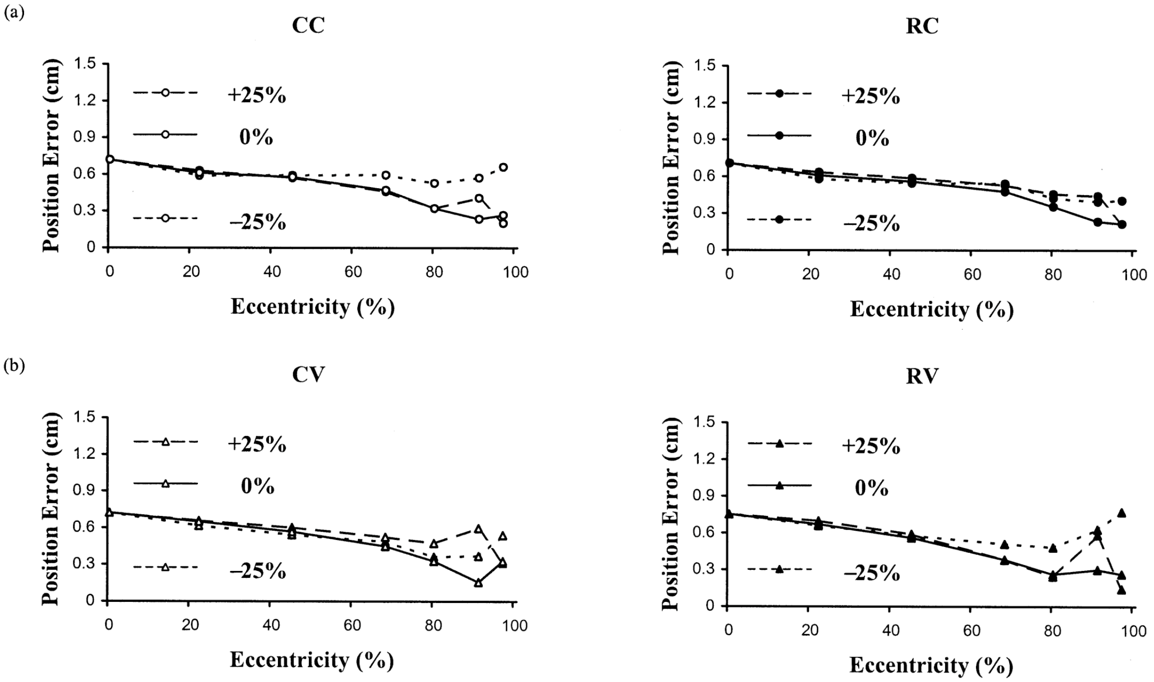

Figure 3.7. Dipole position error versus dipole eccentricity for radial dipoles in the presence of 20% noise (maximum eccentricity is 8.5 cm). Each graph refers to a particular inverse solution, with conventional approaches shown using hollow symbols and reciprocal approaches using full symbols. Relative skull conductivity was 1/15 in all inverse solutions, but a relative skull conductivity of $(1/15) \pm 25\%$ was assumed in computing the input analytic potentials. The CC and RC approaches (circles) use level 1 discretizations for all three spheres, while the CV and RV approaches (triangles) use level 2 discretizations for all spheres.

solution. Other solutions in cluster A also exhibit such marginally better position errors than the minimum RDM solution, but the improvement in position error is not greater than that of the single point in cluster B. We define this maximum improvement of 0.1 mm by a simplex solution with a nonminimum RDM as a *position error tolerance*. For all solutions in the presence of noise, the maximum value of this position error tolerance was 5.2 mm, and in most cases it remained well below this value. This tolerance of 5.2 mm occurs because of the presence of noise in the input signals. For inverse solutions without noise contamination, no converging simplex yielded a solution with a position

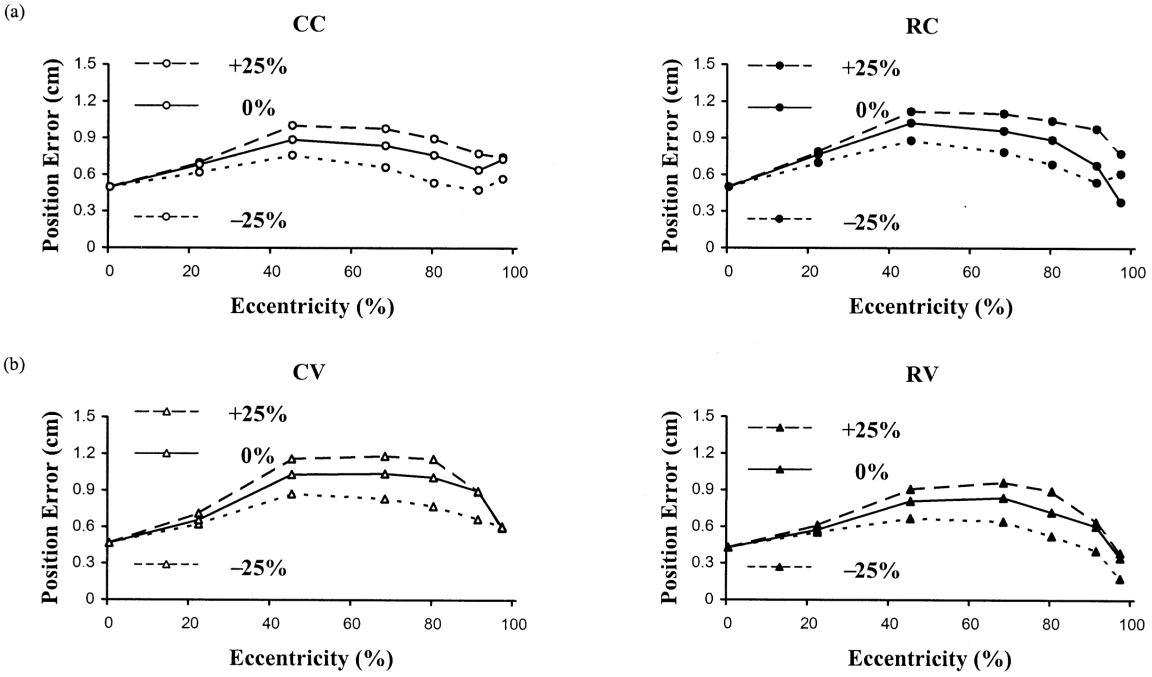

Figure 3.8. Dipole position error versus dipole eccentricity for tangential dipoles in the presence of 20% noise (maximum eccentricity is 8.5 cm). Relative skull conductivity was 1/15 in all inverse solutions, but a relative skull conductivity of $(1/15) \pm 25\%$ was assumed in computing the input analytic potentials. The format is the same as in Figure 3.7.

error that improved on the minimum RDM simplex solution by more than 2 mm. In other words, the maximum position error tolerance was 2 mm. For noiseless inverse solutions, but computed with relative skull conductivity errors of ±25%, the maximum position error tolerance was 2.4 mm. Thus, how well the minimum RDM solution yields the most accurate dipole solution depends on the extent of noise and volume conductor contamination. Also, the given position error tolerances are across all four inverse solution approaches (CC, CV, RC, and RV). No one approach consistently outperformed the others in all situations.

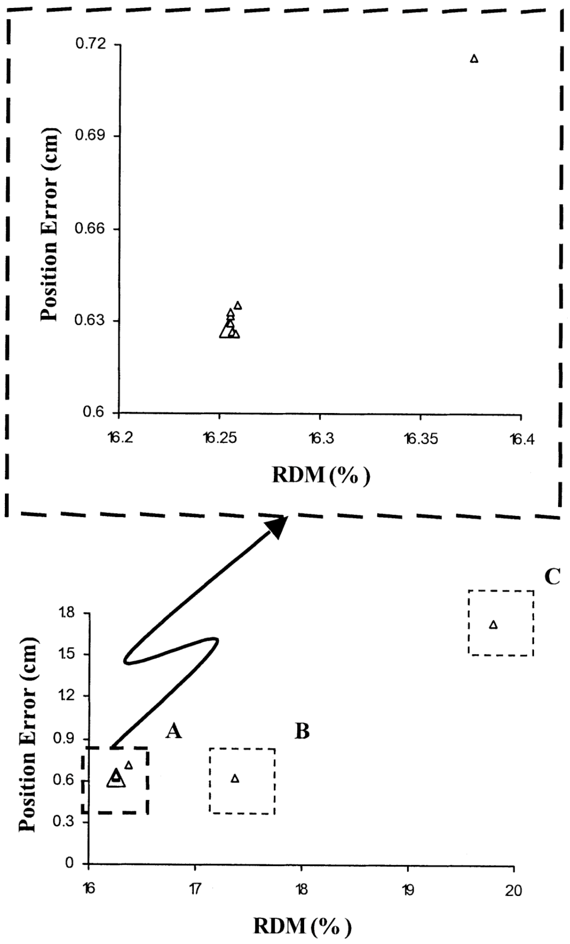

Figure 3.9. Diagram of the dipole position error versus RDM for each of the ten simplex trials used to locate a tangential dipole at an eccentricity of 8.5 cm (97.7%) with a relative skull conductivity of 1/80. The inverse solution was computed with the CV approach, in the presence of 20% noise but with no error in skull conductivity. All simplexes converged, but three clusters (A, B, and C) may be identified. A magnification of cluster A is provided. The minimum RDM solution is identified with a larger triangle, and yields a position error of 6.27 mm. Other solutions in cluster A yielded slightly smaller position errors, but the lowest position error was obtained by the single point corresponding to cluster B, which yielded a position error of 6.17 mm.

3.6 Discussion

The large RDM errors obtained in the forward computations for highly eccentric dipoles are clearly irrelevant, in part due to the robustness of the position error for the single-dipole inverse solution and, to a lesser extent, due to the position constraint employed in the simplex algorithm. By and large, the position errors in the inverse solutions are independent of whether conventional or reciprocal approaches are used to compute the transfer matrices. The inaccuracies in the forward computations are mainly reflected in the orientation and amplitude errors. Our conclusions, however, only hold for single-dipole inverse localizations.

The reduced sensitivity of inverse-dipole position errors to inaccuracies in the forward matrix, coupled with the effect of the position constraint used in the simplex algorithm, means that more accurate computations of these matrices via linear Galerkin (Mosher et al., 1999b) or second-order interpolation (Frijns et al., 2000) would yield limited returns. A similar conclusion may also hold for two-moving-dipole inverse solutions, though admittedly we have not attempted simplex algorithm inverse solutions for the two-dipole case on account of the doubling of the solution parameter space and, potentially, much longer solution times. If, however, solutions to the linear problem of inverse computations of cortical surface potentials or of the amplitudes of a fixed layer of cortical dipoles are desired, more accurate computations of forward transfer matrices should improve the accuracy of these types of inverse solutions.

Inverse solutions with the more recent higher relative skull conductivity value of 1/15 yielded lower position errors than with a relative skull conductivity of 1/80. Also, in general, the relative invariance of reciprocally computed transfer matrices to skull conductivity alterations does not translate to a superiority of reciprocal inverse approaches over conventional ones to skull conductivity errors, once measurement noise is present. Quite simply, the nonlinear nature of the single-dipole inverse problem and the simplex position constraint nullify the beneficial effect of the invariance of reciprocal transfer matrices, just as they did the deleterious effect of the inaccuracies of the forward transfer matrices for highly eccentric dipoles. Once again, as regards position error, there is little to choose between all four approaches.

Simplex solutions converged more consistently, and with fewer iterations, in the presence of measurement noise, than when noise was absent. The reason for this is that noise tends to smooth the valleys of the four-dimensional hyperspace formed by the RDM and the three trial-dipole position coordinates. This was first shown by Musha and Okamoto (1999). Figure 3.10(a) and (b) show two-dimensional semi-logarithmic plots of RDM versus trial-dipole x, y, or z position coordinates, without and with 20% Gaussian measurement noise, respectively. The correct dipole solution is at the origin, and the three curves in each case illustrate the RDM valley profile in three orthogonal directions around this global minimum. One consequence of the noise is the shift in the minimum from the origin, most evident in this case along the x and y directions, and resulting, therefore, in greater position errors. But the noise also raises the valley floor, resulting in much more gradual valley slopes. Musha and Okamoto noted both these changes with noise, but not their effect on simplex minimization. A simplex trial will only converge when the RDM difference between successive iterations is less than 0.0001, which can only occur if the valley floor is reached. However, because of the narrow valley and steep sides, this convergence is very slow. On the other hand, once noise is present, the wider valley floor and shallower slopes result in easier and faster simplex convergence. The down side of this is the presence of multiple small minima on the broad valley floor, that results in different simplex solutions converging to slightly different dipole solutions on either side of the correct dipole, as seen in Figure 3.9. This results in a minimum RDM solution that does not always yield a minimum position error. Nevertheless, in the practical situation, the simplex algorithm may be the most appropriate minimization routine to use, since the difference between the minimum-RDM position error and the absolute-minimum position error is always within a small position error tolerance that is essentially unavoidable due to the noise. This tolerance represents the maximum uncertainty in the simplex solution and is a function of the noise level. In passing, we note that for the noiseless case, an algorithm that makes use of the gradient in the RDM profile to achieve faster convergence may be preferable to the simplex algorithm that relies only on RDM evaluations. Also, although the curves of Figure 3.10 are for the RV approach, similar curves were also found for the other three inverse solution approaches.

Finally, it is very encouraging to note that the minimum RDM criterion used to

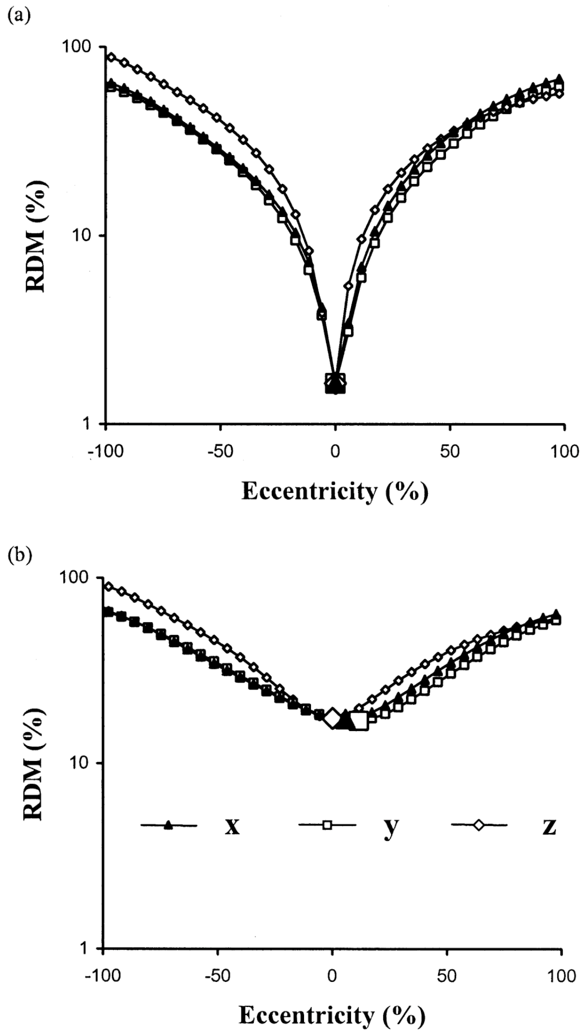

Figure 3.10. RDM plotted against trial dipole eccentricity along x, y, and z axes, for the noiseless case (a) and for 20% Gaussian measurement noise (b). The source dipole is a centric radial dipole, oriented along the direction shown by the dotted arrow in Figure 3.1(a). A three-sphere model with relative skull conductivity of 1/15 was used. Analytic surface potentials were computed from this source dipole for the noiseless case (a), and contaminated with 20% noise (b), to yield the so-called measured potentials $\hat{u}_i$. The RDM is evaluated from (5) with the numerical potentials u_i, corresponding to an optimum dipole placed at trial positions at 0.5-cm intervals along the axes, computed with transfer matrices **T** determined by the RV approach. The minimum RDM point is identified with a larger symbol.

pick the eventual inverse dipole solution amongst converging simplex trials is correct to within a low position error tolerance determined by the measurement noise and the skull conductivity error, and this for all four inverse solution approaches. The correct operation of this criterion is essential in the real-world clinical situation, when the position of the source dipole is unknown.

Chapter 4 Conventional and Reciprocal Approaches to the Inverse Dipole Localization Problem for N_{20}-P_{20} Somatosensory Evoked Potentials

Stefan Finke[1], Ramesh M. Gulrajani[1], Jean Gotman[2], and Pierre Savard[3]

[1]*Institut de génie biomédical, Faculté de médecine, Université de Montréal, Montréal, Québec, Canada*
[2]*Montreal Neurological Institute, McGill University, Montréal, Québec, Canada*
[3]*Institut de génie biomédical, École Polytechnique, Montréal, Québec, Canada*

Submitted for publication to Brain Topography. Manuscript received on March 14, 2012.

4.1 Preface

This work was conducted at the Institute of Biomedical Engineering, Faculty of Medicine, University of Montreal, and the Montreal Neurological Institute (MNI) in Montreal, Quebec, Canada from 2003 to 2011. Note that during this period research was conducted on a part-time basis in the context of an M.D./Ph.D. program through the University of Montreal and a Family Medicine Residency Program through the University of British Columbia, followed by clinical practice as a family physician around Canada. The experimental protocol was approved by the Research Ethics Board of the Montreal Neurological Institute and Hospital in February, 2003. Electroencephalograms (EEGs) following median nerve stimulation as well as electrode registration were performed in the laboratory of Dr. Tomáš Paus at the MNI. Magnetic resonance images (MRIs) and functional magnetic resonance images (fMRIs) were also obtained at the MNI. Although not presented in this thesis, the fMRI protocol was

designed with the assistance of Emma Duerden and Mairie-Claire Albanese and analyzed in the laboratory of Dr. Pierre Rainville at the *CRIUGM* (*Centre de recherche de l'Institut universitaire de gériatrie de Montréal*). Original programs were written by Stefan Finke in Fortran 90 and run through the high-performance computing (HPC) facilities of the *RQCHP* (*Réseau québécois de calcul de haute performance*). Source code is available on request via e-mail at . Text and figures represent the combined efforts of all authors except Ramesh M. Gulrajani who passed away after the data was collected but before work on the manuscript had commenced. Financial support was provided by the Canadian Institutes of Health Research (CIHR). The work of Stefan Finke was also supported in part by an M.D./Ph.D. Scholarship from the CIHR and in part by the *FRQS* (*Fonds de recherche du Québec – Santé*). In memoriam to Ramesh M. Gulrajani.

4.2 Abstract

The non-invasive localization of the primary sensory hand area can be achieved by solving the inverse problem of electroencephalography (EEG) for N_{20}-P_{20} somatosensory evoked potentials (SEPs). This study compares two different mathematical approaches for the computation of transfer matrices used to solve the EEG inverse problem. Forward transfer matrices relating dipole sources to scalp potentials are determined via conventional and reciprocal approaches using individual, realistically shaped head models. The reciprocal approach entails calculating the electric field at the dipole position when scalp electrodes are reciprocally energized with unit current – scalp potentials are obtained from the scalar product of this electric field and the dipole moment. Median nerve stimulation is performed on three healthy subjects and single-dipole inverse solutions for the N_{20}-P_{20} SEPs are then obtained by simplex minimization and validated against the primary sensory hand area identified on magnetic resonance images (MRIs). Solutions are presented for different time points, filtering strategies, boundary-element method (BEM) discretizations, and skull conductivity values. Both approaches produce similarly small position errors for the N_{20}-P_{20} SEP. Position error for

single-dipole inverse solutions is inherently robust to inaccuracies in forward transfer matrices but dependent on the overlapping activity of other neural sources. Significantly smaller time and storage requirements are the principal advantages of the reciprocal approach. Reduced computational requirements and similar dipole position accuracy support the use of reciprocal approaches over conventional approaches for N_{20}-P_{20} SEP source localization.

Keywords: Somatosensory evoked potential, boundary-element method, reciprocity, inverse problem, source localization, equivalent current dipole.

4.3 Introduction

The electroencephalogram (EEG) – the recording of potential differences measured between pairs of electrodes on the scalp – detects volume currents generated in tissues surrounding compact, spatially structured groups of neurons (at least 10^5 synchronously active cells). Using EEG recordings to describe these current sources within the brain is the EEG inverse problem. An inverse solution typically involves multiple calculations of scalp surface potentials, i.e. the EEG forward problem. To solve the forward problem, models are needed for both the underlying source configuration, the source model, and the surrounding tissues, the volume conductor.

The volume conductor is most often a compartment model in which the scalp, skull, brain, and cerebrospinal fluid (CSF) may be represented (Fender, 1991). With the boundary-element method (BEM), compartment surfaces are described by simple geometrical shapes such as spheres, or more realistically, by averaged or individual anatomy obtained from magnetic resonance imaging (MRI) and, to a lesser extent, computed tomography (CT). Each compartment is assumed to be of homogenous and isotropic electrical conductivity, that is to say the conductivity is the same in every direction. The validity of this assumption and the specific conductivity values to assign to each compartment remains a topic of ongoing debate (see Methods).

As for source modeling in EEG, localization techniques often produce estimates of the position and moment of one or more equivalent current dipoles, each representing a current source and sink of equal amplitude separated by a small distance. Alternatively, in distributed models the amplitudes of a fixed layer of cortical dipoles are determined (Nicolas and Deloche, 1976). The equivalent dipole model is an oversimplified but convenient approximation of a few square centimeters or less of synchronously activated cortex (Fender, 1987; Nunez, 1990). The applicability of the dipole model in a given context is reliant on the specific source configuration underlying the measured potentials on the scalp.

Forward transfer matrices relating dipole sources in the brain to resulting potentials at electrode sites on the scalp may be determined via conventional or reciprocal approaches (Fletcher et al., 1995; Finke and Gulrajani, 2001). The reciprocal or "lead-field" approach first entails calculating the electric field at the dipole position under consideration, generated by a unit current injected and withdrawn at scalp electrode sites. Potential differences at the electrode sites are then obtained from the scalar product of this electric field and the dipole moment.

One possible advantage of the reciprocal approach is that, if increased accuracy in forward transfer matrices is required, the volume conductor discretization can be refined exclusively at the known scalp electrode sites. With the conventional approach in which potentials are calculated via an integral equation, increased transfer matrix accuracy demands that the discretization be refined near the dipole position. However solving the inverse problem often involves finding this position that is unknown *a priori*. Interest in the reciprocal approach has been sparked by this possibility of increased accuracy in forward transfer matrices and therefore, presumably, in inverse dipole solutions.

Another advantage of the reciprocal approach is reduced time and storage requirements. Fletcher et al. (1995) indicated that computation times for the reciprocal approach are linearly proportional to BEM head model size, while those of the conventional approach are proportional to its square. Furthermore, for a given BEM model, only the potentials and normal fluxes on the inner brain surface for each electrode pair need to be stored for subsequent inverse solution calculations with the reciprocal approach. In the conventional approach, storage requirements are again proportional to the square of BEM head model size.

In a study employing simulated potentials on spherical boundary-element models, both conventional and reciprocal approaches yielded inverse dipole solutions of comparable accuracy when discretizations refined at scalp electrode sites were used (Finke et al., 2003b). Dipole position errors were small even for highly eccentric source dipoles that exhibit large errors in forward transfer matrices. This inherent robustness of position error is due to the nonlinear nature of the single-dipole inverse solution. Inaccuracies in forward transfer matrices were mainly reflected in the linearly determined orientation and amplitude of these dipoles.

Examples of EEG inverse solutions obtained with reciprocal transfer matrices employing finite-difference (Laarne et al., 2000; Vanrumste et al., 2001) and finite-element (Weinstein et al., 2000) volume conductor discretizations have also previously been published.

The primary somatosensory cortex of the human brain (SI), the main sensory receptive area for the sense of touch, is located in postcentral gyrus of the parietal lobe (i.e., in the posterior bank of the central or Rolandic sulcus) and corresponds to Brodmann area 3b. The SI representation of the human hand was first described intra-operatively in cortical stimulation studies (Penfield and Boldrey, 1937). More recently position emission tomography (PET) (Fox et al., 1987; Nyberg et al., 1996; Bittar et al., 1999) and functional magnetic resonance imaging (fMRI) (Hammeke et al., 1994; Rao et al., 1995; Sakai et al., 1995; Puce et al., 1995; Lin et al., 1996; Pujol et al., 1996; Kurth et al., 1998) have been used to identify the primary sensory hand area non-invasively.

The N_{20}-P_{20} is the earliest cortical potential elicited by median nerve stimulation and, based in part on direct cortical potential recordings (Woolsey et al., 1979; Allison, 1982; Wood et al., 1988; Allison et al., 1989), is believed to be generated by the SI. In these studies the primary hand area has been shown to occupy a very limited volume of the postcentral gyrus (i.e., no more than 30 mm along the central sulcus). Inverse dipole solutions using magnetoencephalography (MEG) (Hari et al., 1984; Kaukoranta et al., 1986; Hari, 1991; Suk et al., 1991; Gallen et al., 1993; Hari et al., 1993; Yang et al., 1993; Kristeva-Feige et al., 1994; Kristeva-Feige et al., 1995; Nakamura et al., 1998) and

EEG (Henderson et al., 1975; Buchner et al., 1995a; Kristeva-Feige et al., 1997) all point to a dipole source tangent to the scalp surface thought to reflect the response of pyramidal neurons in Brodmann area 3b to sensory afferents.

An equivalent dipole source model is now used to localize the central sulcus in the non-invasive pre-operative assessment of patients with a space-occupying lesion or an epileptogenic zone in the central region (Buchner et al., 1994a; Mine et al., 1998; Gross et al., 2000). However focal resection performed in the Rolandic area always carries the risk of sensory or motor deficits and functional information on this region is still often obtained through neurosurgical procedures (King and Schell, 1987; Berger et al., 1989; Burchiel et al., 1989; Suzuki and Yasui, 1992; Hirsch et al., 2000).

The accuracy of EEG inverse solutions is limited by the extent to which scalp SEPs result from the superposition of several source activities located in different parts of the brain. Accounting for all these various effects requires a complex dipole model based on temporal as well as spatial information (Zhang et al., 1994). Equivalent dipoles are often also used to model these secondary overlapping sources (Baumgartner et al., 1991; Franssen et al., 1992; Buchner et al., 1995a), but the exact origins of these activities and the validity of a dipole model in these cases may be less obvious than for the N_{20}-P_{20} SEP.

This paper examines conventional and reciprocal approaches to calculating the single-dipole inverse solutions for N_{20}-P_{20} SEPs obtained from healthy subjects using individual, realistically shaped boundary-element models. As this is a comparison study, a unique single dipole, single time point model is selected although a systematic localization error may result from neglecting the unmodeled source activity. A realistically shaped head model is used since spherical head models may lead to considerable error in dipole position for SEPs (Buchner et al., 1995b).

Strategies for the localization of the primary sensory hand area based on gyral morphology as seen on CT or MRI are possible because of its known anatomical relationship to the primary motor hand area and the central sulcus (Kido et al., 1980; Iwasaki et al., 1991; Naidish et al., 1995; Yousry et al., 1997; Boling et al., 1999). Inverse solution accuracy is determined by comparing calculated dipole positions to a landmark-based identification of the primary sensory hand area on MRI.

4.4 Methods

4.4.1 Forward Transfer Matrices

Assuming that a particular neural source is represented by a current dipole $\mathbf{J}_s$ at a given position in the brain/CSF volume conductor, the potential difference between any two given scalp electrodes *A* and *B*, $u_{AB} \equiv u_A - u_B$, may be expressed as

$$u_{AB} = \mathbf{L} \cdot \mathbf{J}_s \tag{4.1}$$

where $\mathbf{L}$ is the so-called "lead vector." For a fixed dipole position, $\mathbf{T}$ is defined as the $N \times 3$ transfer matrix whose rows contain the individual lead vector components L_x, L_y, and L_z for each of the N electrode pairs considered. These individual lead vector components are determined by either the conventional or the reciprocal approach to the forward problem.

In the conventional approach the lead vector is obtained by calculating the potentials u_i where $i = 1 \ldots N$ corresponding to unit dipoles in the x, y, and z directions at the dipole position under consideration. The three potential values calculated in this way then yield the individual lead vector components L_x, L_y, and L_z, respectively. The alternative reciprocal determination of $\mathbf{L}$ invokes Helmholtz' principle of reciprocity which states that $\mathbf{L} = -\mathbf{E}$. $\mathbf{E}$ is the electric field or "lead field" at the dipole position resulting from a unit current injected into the volume conductor, which is now assumed passive (i.e., containing no source dipole), at electrode *A* and withdrawn at electrode *B*.

From (4.1) the numerical potential differences $\mathbf{U}$, where $\mathbf{U}$ is the matrix of numerical potentials u_i between the N electrode pairs, are calculated via the matrix equation $\mathbf{U} = \mathbf{T}\mathbf{J}_s$. Note that for a given volume conductor, the $\mathbf{T}$ transfer matrices are initially calculated in part independently of dipole position. Time and storage requirements for these partially predetermined matrices differ for the conventional and reciprocal approaches (see Introduction). Further details on the methods used to calculate the $\mathbf{T}$ matrices for all approaches are described in Finke and Gulrajani (2001).

4.4.2 Inverse Solutions

Let $\hat{\mathbf{U}}$ be the column matrix containing the measured potential differences $\hat{u}_i$ between the N electrode pairs on the scalp. The well-known simplex algorithm (He et al., 1987) is used to select the best position for the source dipole by minimizing the relative-difference measure (RDM) between measured and calculated potentials given by

$$\mathrm{RDM} = \sqrt{\frac{\sum_{i=1}^{N}\left(\hat{u}_i - u_i\right)^2}{\sum_{i=1}^{N}\left(\hat{u}_i\right)^2}}\,. \tag{4.2}$$

Prior to calculating the RDM, each iteration of the simplex algorithm entails determining the numerical potentials $\mathbf{U}$ (and hence $\mathbf{T}$) corresponding to the dipole position being evaluated.

For every inverse solution, ten simplex trials with different randomly chosen starting points are run, with stopping points either when the difference in minimum RDM between successive simplex iterations drops below 0.0001, or following a maximum of 1000 iterations. Therefore an individual simplex trial returns a result of either convergence or non-convergence (i.e., having reached the maximum of 1000 iterations). The inverse dipole solution is obtained from the simplex trial with the lowest minimum RDM among the set of converging simplex trials.

The simplex algorithm only searches for the three position coordinates of the source dipole that are nonlinearly related to the RDM. The best moment (i.e., orientation and amplitude) for this inverse dipole solution is linearly determined by the so-called "normal equations", $\mathbf{J}_\mathrm{s} = \mathbf{T}^{+}\hat{\mathbf{U}}$, where $\mathbf{T}^{+}$ is known as the "Moore-Penrose pseudoinverse" of the forward transfer matrix $\mathbf{T}$ (Forsythe and Moler, 1967). Every inverse solution therefore corresponds to a dipole position, orientation, and amplitude. The determination of the forward transfer matrix $\mathbf{T}$ by either conventional or reciprocal approaches results correspondingly in either conventional or reciprocal inverse solutions.

4.4.3 Subjects

SEPs and MRIs are obtained from three healthy right-handed adult male subjects aged 29 to 30. All subjects gave their informed written consent. The Research Ethics Board of the Montreal Neurological Institute and Hospital approved the experimental protocol.

4.4.4 Median Nerve Stimulation

Each subject is seated in a comfortable chair with their eyes open in a semi-darkened, partially shielded room and is asked to remain motionless. An attempt is made to keep the subjects' limbs at a constant temperature for the entire duration of the trial as this is known to affect peripheral nerve conduction velocities. SEPs are evoked by bipolar transcutaneous electrical stimulation applied on the skin over the trajectory of the median nerve. The cathode is placed 2 cm proximal to the wrist crease on the anterior surface of the arm. The anode is placed on the wrist crease thus avoiding anode block. The stimulating electrodes are held in place using a velcro strap.

The median nerves at the right and left wrist are stimulated separately via disk electrodes using constant current, monophasic, square wave pulses of 0.2 ms duration with a repetition rate of just over 3 Hz (Nuclear-Chicago, Des Plaines, IL) (Mauguière et al., 1999; Mauguière, 2005). Electrical stimuli are delivered at intensities equivalent to 3 to 4 times the sensory threshold (10 mA maximum) adjusted to produce a regular twitch in the muscles innervated by the stimulated nerve (i.e., small muscle twitch of the thumb) throughout the trial. At such stimulus intensities all SEP components peaking before 50 ms post-stimulus reach their maximal amplitude. Trial duration is approximately 15 min corresponding to over 2750 stimuli per subject per side.

4.4.5 SEP Recording

SEPs are recorded from 128 scalp electrodes against a common reference electrode Cz at the apex of the head using the Geodesic Sensor Net and the Net Station software package (EGI, Eugene, OR). The inter-electrode distance is approximately 2 cm (Gevins and Bressler, 1988). To record the small fields of the early SEPs an inter-electrode distance of less than 3 cm is required for accurate spatial sampling (Gevins et al., 1990; Spitzer et al., 1989). Each subject's head circumference is measured and an appropriate sensor net size is selected.

SEPs are sampled with 300 points over a 100 ms pre- and 200 ms post-stimulus period (i.e., 1000 Hz sampling frequency). EEG data is kept centered around its baseline (i.e., zero potential) by removing very low frequency components using an analog high-pass filter with 0.1 Hz cutoff. Recording Bessel low-pass filtering is set to 250 Hz. Note that the 50 or 60 Hz notch filter is turned off for SEP recordings since they may be significantly distorted by the use of this filter (i.e., the frequencies of this narrow band form an important part of the SEP).

EEG data is segmented into epochs and artifact rejection is performed (i.e., blinking, movements, etc.). For right and left median nerve stimulation of each subject more than 2500 SEPs are averaged. In order to improve signal-to-noise ratio (SNR) further, EEG data is baseline corrected by subtracting the mean signal from -100 to zero ms recorded at rest. EEG data is re-referenced to the average reference and imported into the BESA software package (BESA, Gräfelfing, DE).

It is generally accepted that most of the energy of the early SEPs is contained in the 20-250 Hz frequency band (Lüders et al., 1986). Further digital filtering is required in order to reduce the overlap of low frequency EEG components that, if not filtered, can lead to substantial source localization error. In general the use of a zero-phase shift type filter is recommended because this results in minimal phase distortion of the EEG data and better suppression of frequencies outside the selected frequency band. However, according to Scherg et al. (1999), a forward type filter should be used to analyze the early, weak N_{20}-P_{20} SEP activity. The concern is that because a zero-phase shift low cutoff filter has symmetric sidelobes in time, the stronger later SEP activity around 24-35 ms may be projected into the earlier phase of 13-22 ms. Therefore inverse dipole solutions are calculated on two EEG data sets, one filtered with the zero-phase shift type (20 Hz, 24 dB/oct, high-pass) and one filtered with the forward type (20 Hz, 6 dB/oct, high-pass) in BESA (Buchner et al., 1995b).

Excluded from further analysis are seven bad channels for Subject A (17, 49, 69, 95, 114, 126, 127), six bad channels for Subject B (49, 69, 95, 114, 126, 127), and two bad channels for Subject C (126, 127). All bad channels are removed because of poor SNR in the original EEG recording except electrode 17 for Subject A, which is removed because of erroneous electrode registration (i.e., the registered electrode position is not on or near the scalp surface (see below)). Only the interval from 10-50 ms post-stimulus is kept for further analysis.

4.4.6 SEP Analysis

The global field power (GFP) at a specific time point is defined as (Lehmann, 1987)

$$\text{GFP} = \sqrt{\frac{1}{N}\sum_{i=1}^{N}\left(\hat{u}_i - \frac{\sum_{j=1}^{N}\hat{u}_j}{N}\right)^2} \tag{4.3}$$

where again $\hat{u}_i$ denotes the measured potential differences between the N electrode pairs on the scalp. The second term on the right in (4.3) corresponds to the mean potential difference of the N electrode pairs or the so-called “average reference” (Nunez, 1981). Since the GFP takes only differences between measured potentials into account, it is independent of the reference electrode used and is therefore a reference-independent measure of the evoked potential activity.

The GFP is an assessment of the spatial variation of the potentials measured on the scalp at each point in time and therefore essentially reflects the degree of dispersion in a given potential distribution. The time point corresponding to the largest instantaneous global activity, defined on the basis of a peak in the GFP, is selected for source analysis in the interval of interest (i.e., 20-24 ms post-stimulation) (Buchner et al., 1995b). All bad channels are omitted prior to GFP calculations. GFP peaks are determined separately for zero-phase shift and forward filtered EEG data.

4.4.7 MRI Acquisition

MRI acquisition is performed prior to SEP recording using a 1.5 T Siemens Sonata scanner (Siemens, Erlangen, DE) and a standard head coil. A vacuum-sealed bag positioned around the individual's head is used to minimize motion artifacts. Subjects are comfortably positioned and told to remain motionless with their eyes closed. T_1-weighted 3D standard gradient-echo pulse sequence scans (fast low-angle shot (FLASH)) are acquired for each subject with the following specifications: 15 ms repetition time (TR), 5 ms echo time (TE), 30° flip angle, single excitation, 256 mm field of view (FOV), and 256 x 256 image matrix. Fat suppression (FS) is used to avoid chemical shift artifacts that can impact subsequent scalp surface segmentations (Brinkmann et al., 1998). This results in 192 one mm thick contiguous sagittal slices per subject after a total acquisition time of approximately 12 min.

4.4.8 Electrode Registration

Electrode registration is performed using Brainsight (Rogue Research, Montreal, QC). The location of scalp electrodes with respect to anatomical landmarks on the head are determined with a 3D digitizer (Polaris Optical Tracking System (NDI, Waterloo, Ontario)) to allow alignment of the EEG electrode coordinates with the anatomy provided by separate MRIs. The Brainsight Subject Tracker (ST-409) (i.e., a pair of glasses mounted with a subject tracker) is placed on the subject after the scalp electrodes but before the EEG recording is started. Individual MRIs are imported into the Brainsight software and the subjects are placed within the digitizer for electrode registration.

Landmarks (i.e., nasion, inion, and left and right pre-auricular points (PAL and PAR, respectively)) are co-registered in the digitizer real space and image space, allowing the generation of a transform mapping points in real space to image space. The 129 electrodes are consecutively registered in real space, transformed, and then displayed in image space over the individual's MRI where they are visually verified. Finally landmarks and electrode positions are again transformed and read into the CURRY software package (Neuroscan, Charlotte, NC) where they are projected onto the corresponding subject's BEM discretization for the scalp surface.

4.4.9 BEM Head Models

MRIs are segmented and transformed into BEM discretizations for scalp, skull, and brain/CSF surfaces using CURRY. Discretization elements consist of planar triangles and nodes consist of triangle vertices. Figure 4.1A shows discretizations obtained from CURRY for the scalp (i), skull (ii), and brain/CSF (iii) of Subject A. For the scalp surface these discretizations are referred to as Level 1. The 129 projected electrode sites for Level 1 discretizations correspond to triangle vertices (see Figure 4.1A(i)). Figure 4.1B illustrates refinement of the discretization in A(i) around electrode 94 for the scalp surface of Subject A (see below).

Forward transfer matrices are calculated between source dipole and scalp potentials at triangle centroids or between source dipole and scalp potentials at triangle vertices. Accordingly four possibilities for these forward transfer matrices are obtained, either a conventional centroid (CC) or a conventional vertex (CV) approach, or alternatively a reciprocal centroid (RC) or reciprocal vertex (RV) approach. Vertex approaches solve for approximately half the number of unknowns compared to centroid approaches because in a triangular discretization the number of vertices is approximately half the number of triangles. With the two centroid approaches the potential is assumed constant across each triangle. With the vertex approaches a linear variation in potential is assumed.

To exploit one possible advantage of the reciprocal approaches, the scalp discretizations are selectively refined in the vicinity of the projected electrode sites (see Introduction). These modified scalp discretizations are referred to as Level 2. With Level 2 discretizations the projected electrode sites correspond to triangle centroids (see Figure 4.1B(i)). In the reciprocal approaches these electrode sites are used for current injection and withdrawal. Because of the difficulty in calculating the current distribution following injection at a triangle vertex (Finke and Gulrajani, 2001), a slightly different discretization is used with the RV approach. A curvilinear quadrilateral is inserted at each

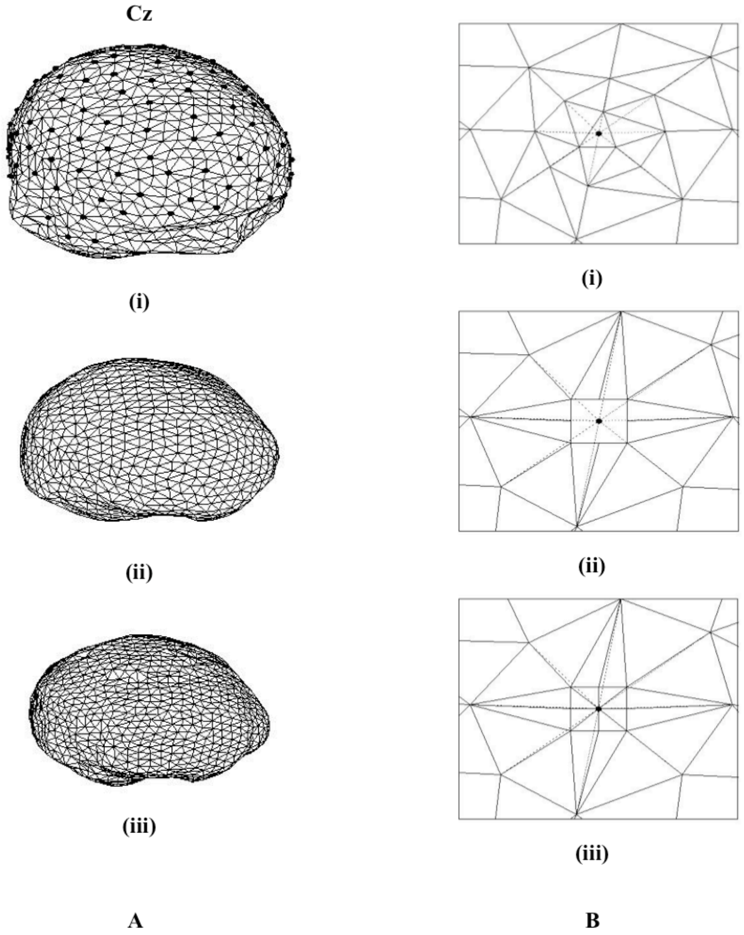

Figure 4.1. A shows discretizations obtained from CURRY for the scalp (i), skull (ii), and brain/CSF surfaces (iii) of Subject A. Projected electrode sites including the reference electrode Cz are shown with black circles at triangle vertices in A(i). B illustrates refinement (solid lines) of the discretization in A(i) around electrode 94 for the scalp surface (dashed lines) of the same subject. In B(i) the electrode site corresponds to the innermost triangle centroid, in B(ii) the electrode site corresponds to the quadrilateral center, and in B(iii) the electrode site corresponds to the innermost triangle vertex. Level 1 (shown in A(i)), Level 2 (shown in B(i)), and Level 3 (shown in B(iii)) discretizations for the scalp surfaces are used with the CC, CV, and RC approaches while Level Q (shown in B(ii)) discretization for the scalp surface is used with the RV approach. All approaches use discretizations for the skull and brain/CSF surfaces shown in A(ii) and A(iii), respectively. See Table 4.1 and text for additional details.

			Number of elements	Number of nodes	Average edge length (mm)	Average radius (mm)
SUBJECT A	Scalp	Level 1	2510	1257	10.81	97.81
		Level 2	4544	2274	7.87	94.86
		Level 3	4462	2233	7.93	94.92
		Level Q	3608	2233	9.46	94.92
	Skull		2282	1143	9.45	81.02
	Brain/CSF		2988	1496	7.55	72.89
SUBJECT B	Scalp	Level 1	2582	1293	10.78	98.76
		Level 2	4630	2317	7.87	96.08
		Level 3	4550	2277	7.92	96.21
		Level Q	3689	2277	9.43	96.21
	Skull		2226	1115	9.47	79.88
	Brain/CSF		2942	1473	7.53	72.54
SUBJECT C	Scalp	Level 1	2474	1239	10.77	97.00
		Level 2	4570	2287	7.74	93.87
		Level 3	4506	2255	7.87	93.96
		Level Q	3617	2255	7.79	93.96
	Skull		2150	1077	9.49	78.52
	Brain/CSF		2890	1447	7.58	71.80

Table 4.1. The number of elements and nodes, the average element edge lengths, and the average surface radii in mm are given for Level 1, 2, 3, and Q discretizations for the scalp surface as well as for discretizations for the skull and brain/CSF surfaces of Subjects A, B, and C (see Figure 4.1). Discretization elements are triangles and nodes are triangle vertices except for Level Q where elements also include curvilinear quadrilaterals (i.e., one at each electrode site considered) and nodes also include quadrilateral vertices (i.e., nine per quadrilateral). Level 1, Level 2, and Level 3 discretizations for the scalp surface are used with the CC, CV, and RC approaches while Level Q discretization for the scalp surface is used with the RV approach. All approaches use identical discretizations for the skull and brain/CSF surfaces of each subject. All radii are calculated in relation to the center of the innermost brain/CSF volume conductor.

electrode site with quadratic interpolation of the potential for these elements only. In this case the projected electrode sites (i.e., the sites of current injection) correspond to the center of the quadrilaterals (see Figure 4.1B(ii)). The resulting discretization is referred to as Level Q.

In an attempt at limiting any discretization related biases when comparing the different approaches, the quadrilaterals in Level Q discretizations are further divided into planar triangles. This final scalp discretization is referred to as Level 3. Again the projected electrode sites correspond to triangle vertices (see Figure 4.1B(iii)). So in summary Level 1, Level 2, and Level 3 discretizations for the scalp surface are used with the CC, CV, and RC approaches while Level Q discretizations for the scalp surface is used with the RV approach. All approaches use identical discretizations for the skull and brain/CSF surfaces of each subject (see Figures 4.1A(ii) and (iii), respectively).

Table 4.1 gives the number of elements and nodes, the average element edge lengths, and the average surface radii for Level 1, 2, 3, and Q discretizations for the scalp surface as well as for discretizations for the skull and brain/CSF surfaces of Subjects A, B, and C. The number of discretization elements per surface ranges from about 2000 to 5000 and the number of nodes ranges from about 1000 to 2500. Level 1 discretizations consist of the smallest number of elements for the scalp surface and Level 2 discretizations consist of the largest. Average element edge lengths are approximately 10 mm or below. Average radii are approximately 96, 80, and 72 mm for the scalp, skull, and brain/CSF surfaces, respectively.

For a given scalp discretization the projected electrode sites do not exactly correspond to the modeled electrode sites for certain approaches. This difference between projected electrode sites and modeled electrode sites is referred to as the electrode localization error. For example for Level 1 discretizations where the projected electrode sites correspond to triangle vertices, the electrode localization errors for the CC and RC approaches are approximately 5 mm on average since the scalp potentials are calculated at triangle centroids. Table 4.2 gives the maximum and average electrode localization errors for the CC, CV, RC, and RV approaches for Level 1, 2, 3, and Q discretizations for the scalp surfaces of Subjects A, B, and C. Electrode localization errors for Level 2 and 3 discretizations are smaller than for Level 1 discretizations (i.e., approximately 1.5 mm or

		ELECTRODE LOCALIZATION ERROR (mm)					
		SUBJECT A		**SUBJECT B**		**SUBJECT C**	
		Maximum	Average	Maximum	Average	Maximum	Average
CC	Level 1	7.0632	5.1135	7.4685	5.1195	7.0159	5.1049
	Level 2	0.6503	0.2540	0.8258	0.2722	0.9766	0.2844
	Level 3	1.7621	1.5050	1.7633	1.5038	1.8627	1.5542
CV	Level 1	0	0	0	0	0	0
	Level 2	2.5440	1.4971	2.1794	1.5028	2.2425	1.5666
	Level 3	0	0	0	0	0	0
RC	Level 1	7.0632	5.1135	7.4685	5.1195	7.0159	5.1049
	Level 2	0.6503	0.2540	0.8258	0.2722	0.9766	0.2844
	Level 3	1.7621	1.5050	1.7633	1.5038	1.8627	1.5542
RV	Level Q	0	0	0	0	0	0

Table 4.2. Maximum and average electrode localization errors in mm for the CC, CV, RC, and RV approaches for Level 1, 2, 3, and Q disretizations for the scalp surface of Subjects A, B, and C. Level 1, Level 2, and Level 3 discretizations for the scalp surface are used with the CC, CV, and RC approaches while Level Q discretization for the scalp surface is used with the RV approach.

less on average) because of the selective refinement around electrode sites in these discretizations.

Two different sets of conductivities are used for the scalp, skull, and brain/CSF volume conductors: (1) 0.33, 0.0042, 0.33 S/m (Geddes and Baker, 1967) and (2) 0.33, 0.022, 0.33 S/m for scalp, skull, and brain/CSF, respectively. The first set corresponds to the frequently employed relative skull conductivity of 1/80 (Rush and Driscoll, 1968; Cohen and Cuffin, 1983; Homma et al., 1994) and the second reflects the higher relative skull conductivity of 1/15 suggested by more recent work (Oostendorp et al., 2000). Some earlier studies also supported a higher skull conductivity (Kosterich et al., 1984; Law, 1993; Gabriel et al., 1996).

4.4.10 Anatomical Localization of the Primary Sensory Hand Area

As discussed in the Introduction, the cortical representation of primary sensory hand function is contained in the anterior wall of the postcentral gyrus in Brodmann area

3b. This primary sensory hand area is adjacent to the primary motor hand area that is readily identifiable on MRI using known anatomical landmarks (Yousry et al., 1997). The characteristic knob-like structure arising from the posterior wall of the precentral gyrus is shaped like an Ω or ε in the axial plane and like a hook in the sagittal plane through Broca's *pli de passage fronto-pariétal moyen* (Broca, 1888) that bulges into the central sulcus at the level of the middle knee. The primary sensory hand area is identified on MRI as above in the NeuroLens software package (University of Montreal, Montreal, QC) for both hemispheres of all three subjects. Figure 4.2 shows axial and sagittal views of the left primary sensory hand area for Subject A. Dipole position error, defined as the shortest distance between the N_{20}-P_{20} SEP inverse solutions and these cortical areas (i.e.,

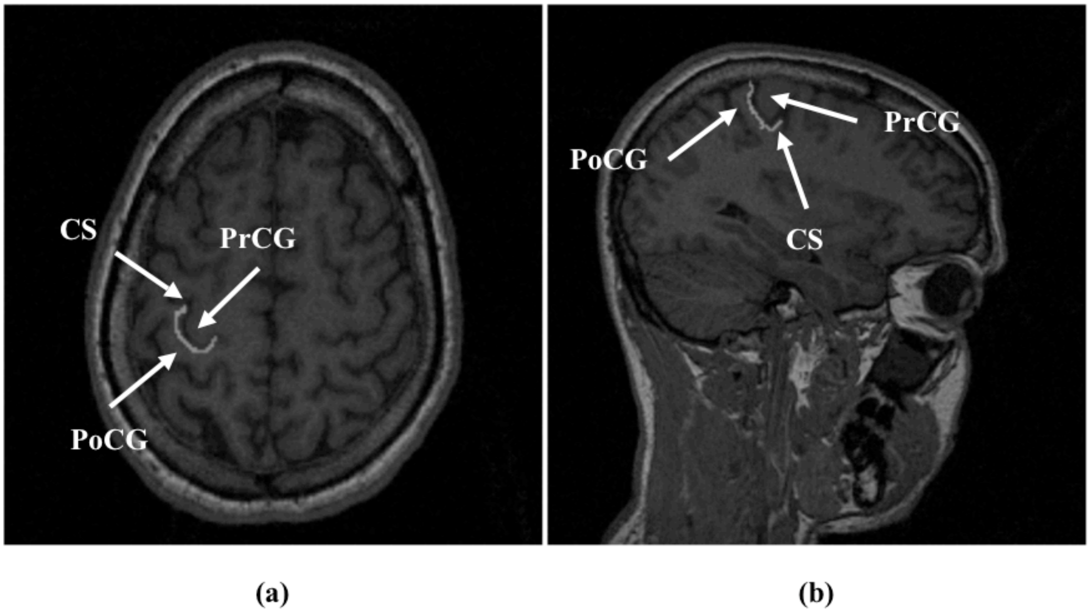

(a) (b)

Figure 4.2. Axial (a) and sagittal (b) slices through the left primary sensory hand area (shown in grey) identified on MRI for Subject A. The characteristic knob-like structure arising from the posterior wall of the precentral gyrus (PrCG) is shaped like an Ω in the axial (a) plane and like a hook in the sagittal (b) plane and corresponds to the left primary motor hand area. The primary sensory hand area is adjacent to the primary motor hand area in the posterior bank of the central sulcus (CS) in the postcentral gyrus (PoCG). Note that the scales in (a) and (b) are different. Images are generated using NeuroLens.

the minimum distance between the dipole position and the nearest voxel identified as belonging to the corresponding primary sensory hand area), is used as an index of precision for each of the four approaches.

4.5 Results

The CC, CV, RC, and RV approaches are used to calculate the single-dipole inverse solutions for N_{20}-P_{20} SEPs recorded following right and left median nerve stimulation of Subjects A, B, and C. Level 1, Level 2, and Level 3 discretizations for the scalp surface are used by the CC, CV, and RC approaches while Level Q discretization for the scalp surface is used by the RV approach. A relative skull conductivity of 1/15 is initially assumed (i.e., 0.33 S/m for the scalp, 0.022 S/m for the skull, and 0.33 S/m for the brain/CSF volume conductor). Initial analysis is performed on the zero-phase shift filtered data.

As described in Methods, the N_{20}-P_{20} SEP time points analyzed are selected based on peaks in the GFP (defined in (4.3)) within the interval of interest (i.e., 20-24 ms post-stimulation). For Subjects A and C, GFP peaks all correspond to 22 ms post right and left median nerve stimulation. However, for Subject B, no GFP peaks are found in this interval for either right or left hand data. In the absence of another obvious time point to analyze, 22 ms post-stimulation is selected as the initial estimate for this subject as well. Note that analysis is also performed at 21 and 23 ms for comparison purposes (see below).

The relative-difference measure (RDM, Equation 4.2), which compares measured and calculated scalp potentials numerically, is minimized by the simplex algorithm to select the best location for the trial dipole in each stimulation study (see Methods). All ten simplex trials for each inverse solution converge to a minimum RDM value in much less than 1000 iterations and the number of iterations required is similar for all approaches. The vast majority of simplex trials converge around the global RDM minima and produce similar dipole solutions for a given approach, scalp discretization, and stimulation study. Only one simplex trial for the CC (Level 2 and 3), CV (Level 3), and

RC (Level 2 and 3) approaches converges to a local minimum for left median nerve stimulation of Subject B and produces a clearly distinct dipole solution (i.e., greater than 1 cm dipole position difference). Among simplex trials converging around the global RDM minima, the maximum RDM value difference is 0.1%, the maximum dipole position difference is 2 mm, the maximum dipole orientation difference is 1°, and the maximum dipole amplitude difference is 0.1 $\mu A/mm^2$.

Average-reference measured and calculated N_{20}-P_{20} SEPs for the CC (Level 1), CV (Level 1), RC (Level 2), and RV (Level Q) approaches are shown in Figure 4.3 for right and left median nerve stimulation of Subjects A, B, and C. A scalp potential distribution consistent with an eccentric tangential dipole is measured over the contralateral parietal area in each stimulation study as expected. In general the calculated distributions concur with the corresponding measured distributions, the most visible difference being at the positive pole for right median nerve stimulation of Subject B. Calculated potential distributions for the four approaches are nearly identical in appearance for a given stimulation study.

Table 4.3 gives the minimum RDM values corresponding to the inverse solutions for the CC, CV, RC, and RV approaches for right and left median nerve stimulation of Subjects A, B, and C. Overall minimum RDM values are high, ranging from 12% to 58.5%, indicating quite large numerical differences between measured and calculated potentials. However RDM values were found to be high even with simulated potentials on spherical models with or without noise, greater than 100% for some eccentric dipole locations, and still reasonably accurate dipole positions were obtained (Finke et al., 2003b).

For the CC, CV, and RC approaches, Level 1 discretization of the scalp surface produces the highest minimum RDM for all stimulation studies and Level 2 the lowest overall. This is not surprising considering that Level 1 and Level 2 discretizations consist of the least and the most number of triangles, respectively (see Table 4.1). For both the CC and the RC approaches, these higher minimum RDM values for Level 1 discretizations are likely also due to the greater distance between the projected electrode sites on the scalp surface, which correspond to triangle vertices in Level 1 discretizations, and the electrode sites assumed in the CC and RC approaches which correspond to

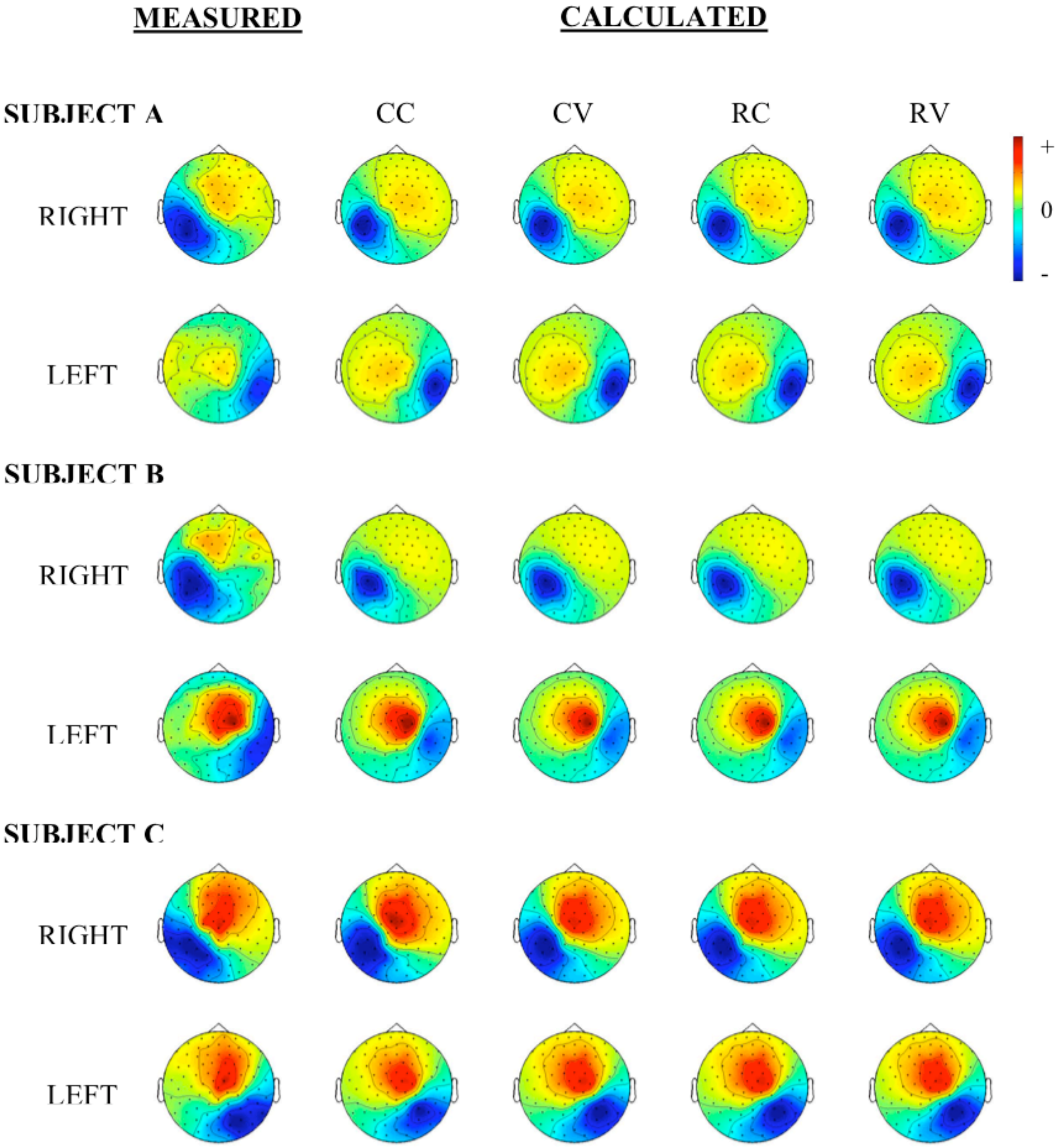

Figure 4.3. Average-reference measured and calculated N_{20}-P_{20} SEPs for right and left median nerve stimulation of Subjects A, B, and C visualized from directly above each subject (i.e., reference electrode Cz). Calculated scalp potential distributions are shown for the CC (Level 1), CV (Level 1), RC (Level 2), and RV (Level Q) approaches. CC, CV, and RC calculated potential distributions for other discretizations of the scalp surface (not shown) are similar in appearance to those shown for each stimulation study. Note that scale ranges for different potential distributions are not identical. Images are generated using EEGLAB in MATLAB (Mathworks, Natick, MA).

		RDM (%)					
		SUBJECT A		**SUBJECT B**		**SUBJECT C**	
		Right	Left	Right	Left	Right	Left
CC	Level 1	35.1177	45.2110	58.5216	33.0232	13.3342	16.7421
	Level 2	34.5826	44.7938	55.9722	32.2054	12.0350	16.0126
	Level 3	34.6236	44.6864	56.4291	32.2600	12.0814	15.9136
CV	Level 1	34.5976	44.7824	55.9621	32.2038	12.0831	15.9630
	Level 2	34.7554	44.9082	55.9844	32.1690	12.2884	15.9023
	Level 3	34.5999	44.7847	55.9597	32.2054	12.0835	15.9616
RC	Level 1	35.0680	45.1827	58.4683	32.9576	13.3436	16.6814
	Level 2	34.5436	44.7691	55.9401	32.1678	12.0434	16.0108
	Level 3	34.5595	44.6219	56.3862	32.2123	12.1292	15.9393
RV	Level Q	34.8278	44.9073	56.0441	32.2323	11.9821	15.8410

Table 4.3. Relative-difference measure (RDM) in % of N_{20}-P_{20} SEP inverse solutions for right and left median nerve stimulation of Subjects A, B, and C. Level 1, Level 2, and Level 3 discretizations for the scalp surface are used by the CC, CV, and RC approaches while Level Q discretization for the scalp surface is used by the RV approach.

triangle centroids (see Table 4.2).

The lowest RDM values are for right median nerve simulation of Subject C and the highest RDM values are for right median nerve stimulation of Subject B for all approaches and scalp discretizations. Whether in terms of potential distributions or RDM values, there is little to choose between the four approaches. The CC approach produces the highest minimum RDM values for almost all stimulation studies and the reciprocal approaches produce the lowest but only marginally. In fact the greatest difference in minimum RDM values between approaches for a given stimulation study is only 2.6% between the CC (Level 1) and the RC (Level 2) approaches for right median nerve stimulation of Subject B.

To further illustrate the similarities between inverse solutions for a given stimulation study, average dipole position, orientation, and amplitude differences between the various approaches and scalp discretizations are small (i.e., 1.5 mm, 0.9º, and 0.1 $\mu A/mm^2$, respectively). The maximum difference in dipole position is 5.1 mm, the maximum dipole orientation difference is 3.3º, and the maximum difference in dipole amplitude is 0.5 $\mu A/mm^2$.

Dipole position errors for the CC, CV, RC, and RV approaches are given in Table 4.4 for right and left median nerve stimulation of Subjects A, B, and C. As described in Methods, dipole position errors are calculated as the distance between the inverse solutions and the nearest point of the corresponding primary sensory hand area identified on MRI. Position errors range from zero to 11.3 mm for the CC approach, zero to 13.5 mm for the CV approach, zero to 11.2 mm for the RC approach, and zero to 11.1 mm for the RV approach. These values are similar to those found for simulated potentials on spherical models (Finke et al., 2003b), where a position error of approximately 1 cm was produced for tangential dipoles of intermediate eccentricity in the presence of noise.

The smallest dipole position errors are for right median nerve simulation of Subject A, corresponding to inverse solutions mostly located within the primary sensory hand area, and the largest position errors are for right and left median nerve stimulation of Subject B for all approaches. Again there is little to choose between the four approaches. The conventional approaches produce the smallest dipole position error for

		DIPOLE POSITION ERROR (mm)					
		SUBJECT A		**SUBJECT B**		**SUBJECT C**	
		Right	Left	Right	Left	Right	Left
CC	Level 1	0	4.9985	9.3522	8.3338	2.6894	1.5319
	Level 2	0	5.7673	10.3544	11.2758	1.6134	1.9570
	Level 3	0	5.2775	9.1109	10.9267	2.2009	2.7744
CV	Level 1	0.0469	5.6867	10.3417	11.9638	1.1619	1.6716
	Level 2	0	4.7985	10.5484	13.4578	1.6436	1.6444
	Level 3	0.1643	5.6260	9.8340	11.4137	1.1522	1.7116
RC	Level 1	0	4.9036	9.4066	8.5666	2.7220	1.3922
	Level 2	0	5.6890	10.6139	11.2100	1.5438	2.0219
	Level 3	0	5.4232	9.3671	11.0831	1.9396	2.4836
RV	Level Q	0	5.4488	11.0971	10.6657	2.3327	3.2927

Table 4.4. Dipole position error in mm of N_{20}-P_{20} SEP inverse solutions for right and left median nerve stimulation of Subjects A, B, and C compared to the nearest point of the corresponding primary sensory hand areas identified on MRI. Level 1, Level 2, and Level 3 discretizations for the scalp surface are used by the CC, CV, and RC approaches while Level Q discretization for the scalp surface is used by the RV approach. A position error of zero signifies that the dipole is located within the primary sensory hand area.

all stimulation studies except for left median nerve stimulation of Subject C, but no single approach consistently outperformed the others. The greatest difference in dipole position error between approaches for a given stimulation study is 5.1 mm between the CV (Level 2) and the CC (Level 1) approaches for left median nerve stimulation of Subject B.

Figures 4.4, 4.5, and 4.6 show inverse solutions for right and left median nerve stimulation of Subject A, B, and C, respectively, for the CC (Level 1), CV (Level 1), RC (Level 2), and RV (Level Q) approaches compared to the nearest point of the corresponding primary sensory hand areas identified on MRI. Again the similarities between dipoles in terms of both moment and position are clear. Overall position error is equally distributed in the axial, sagittal, and coronal planes. Inverse solutions tend to be located in the postcentral gyrus within or posterior to the primary sensory hand area except for left median nerve stimulation of Subject B that produces dipoles in the precentral gyrus. Note that there are no obvious landmarks to delimit the vertical extent of Brodmann area 3b in the posterior bank of the central sulcus. The postcentral gyrus at the apex of the central sulcus may in part correspond to Brodmann area 1 and the nadir to Brodmann area 3a. Although including its full vertical extent in the primary sensory hand area potentially underestimates position error for certain stimulation studies, it is unlikely to modify the small relative differences between the four approaches.

Although reciprocal approaches produce inverse solutions with the lowest minimum RDMs (see Table 4.3), the conventional approaches produce the smallest dipole position errors overall, findings which may seem somewhat counterintuitive. This relationship between dipole position error and inverse solution RDM is illustrated in Figure 4.7 for the CC (Level 1), CV (Level 1), RC (Level 2), and RV (Level Q) approaches for right and left median nerve stimulation of Subjects A, B, and C. Even if the general trend is for higher RDM values to produce larger position errors, the highest RDM values are for right median nerve stimulation of Subject B and correspond to similar position errors to those for left median nerve stimulation of Subject B with its lower RDM values. On the other hand the lowest RDM values are for right median nerve stimulation of Subject C and do not correspond to the smallest position errors (i.e., right median nerve stimulation of Subject A). Even the observed marginal improvement in minimum RDM values due to scalp discretization refinement and lower electrode

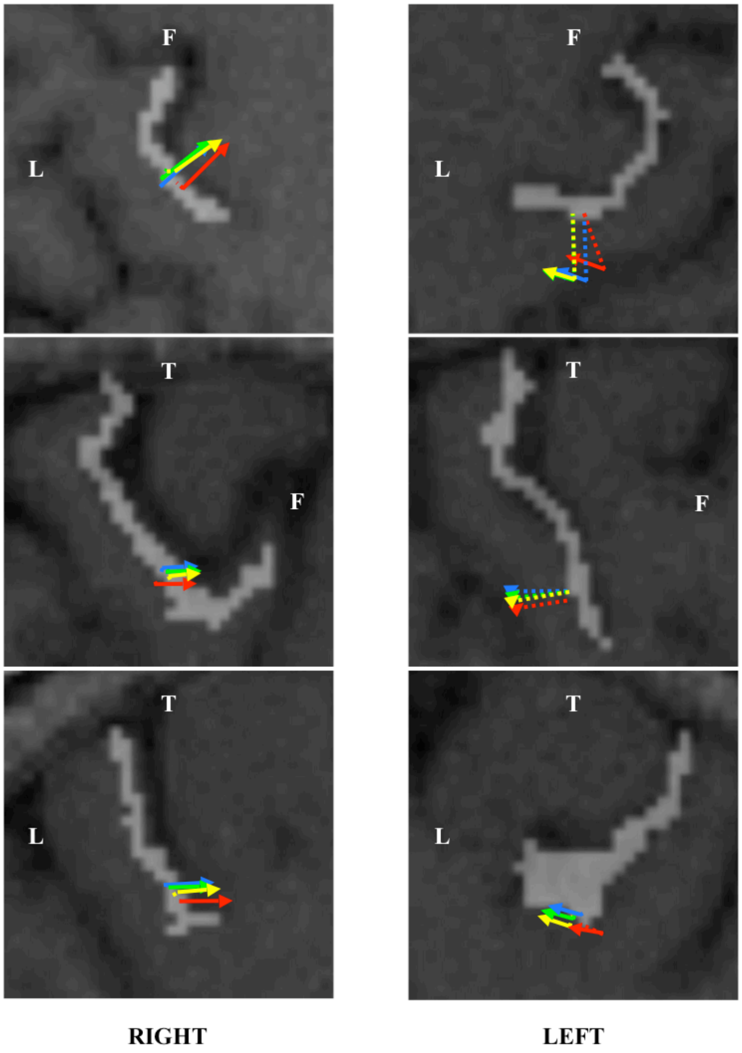

Figure 4.4. N_{20}-P_{20} SEP inverse dipole solutions for right and left median nerve stimulation of Subject A for the CC (Level 1), CV (Level 1), RC (Level 2), and RV (Level Q) approaches compared to the nearest point of the corresponding primary sensory hand areas identified on MRI. Primary sensory hand areas are shown in grey. Red, blue, green, and yellow represent the CC, CV, RC, and RV approaches, respectively. Arrows depict inverse dipole solutions and dashed lines depict dipole position errors projected onto the image plane. Shown are axial (top), sagittal (middle), and coronal (bottom) slices through the median coordinates of the primary sensory hand area points nearest to the inverse dipole solutions. L indicates the left, F the front, and T the top of the subject's head. Note that the distances shown are 2.3 times the actual values. Images are generated using NeuroLens.

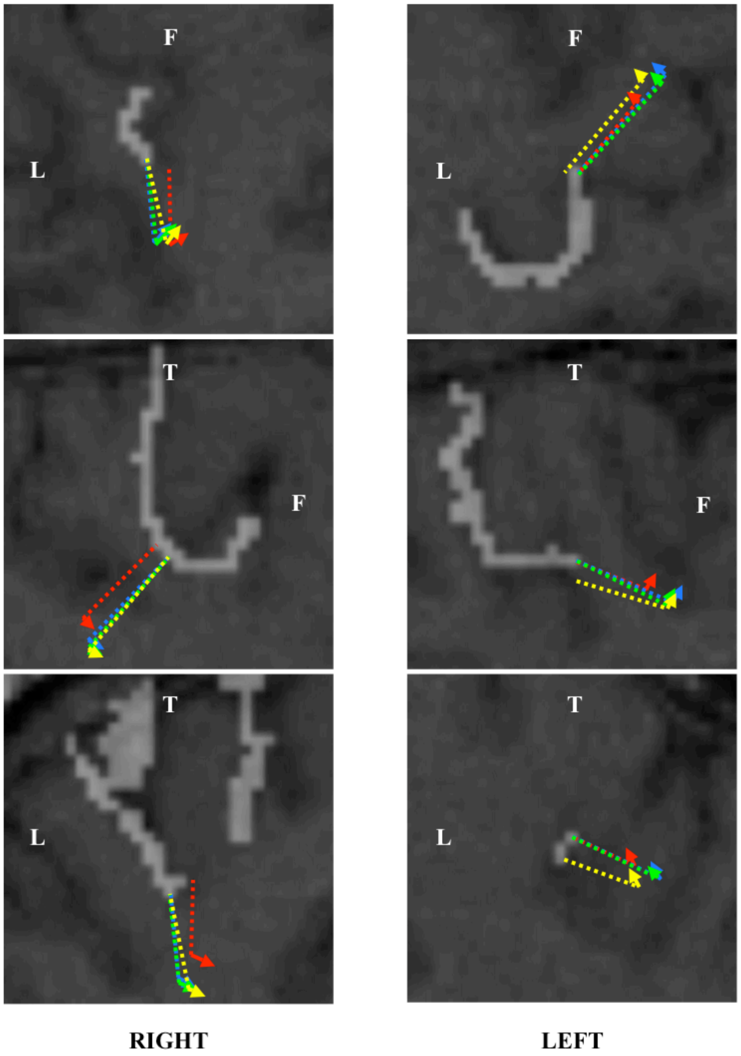

Figure 4.5. N_{20}-P_{20} SEP inverse dipole solutions for right and left median nerve stimulation of Subject B for the CC (Level 1), CV (Level 1), RC (Level 2), and RV (Level Q) approaches compared to the nearest point of the corresponding primary sensory hand areas identified on MRI. Primary sensory hand areas are shown in grey. Red, blue, green, and yellow represent the CC, CV, RC, and RV approaches, respectively. Arrows depict inverse dipole solutions and dashed lines depict dipole position errors projected onto the image plane. Shown are axial (top), sagittal (middle), and coronal (bottom) slices through the median coordinates of the primary sensory hand area points nearest to the inverse dipole solutions. L indicates the left, F the front, and T the top of the subject's head. Note that the distances shown are 2.3 times the actual values. Images are generated using NeuroLens.

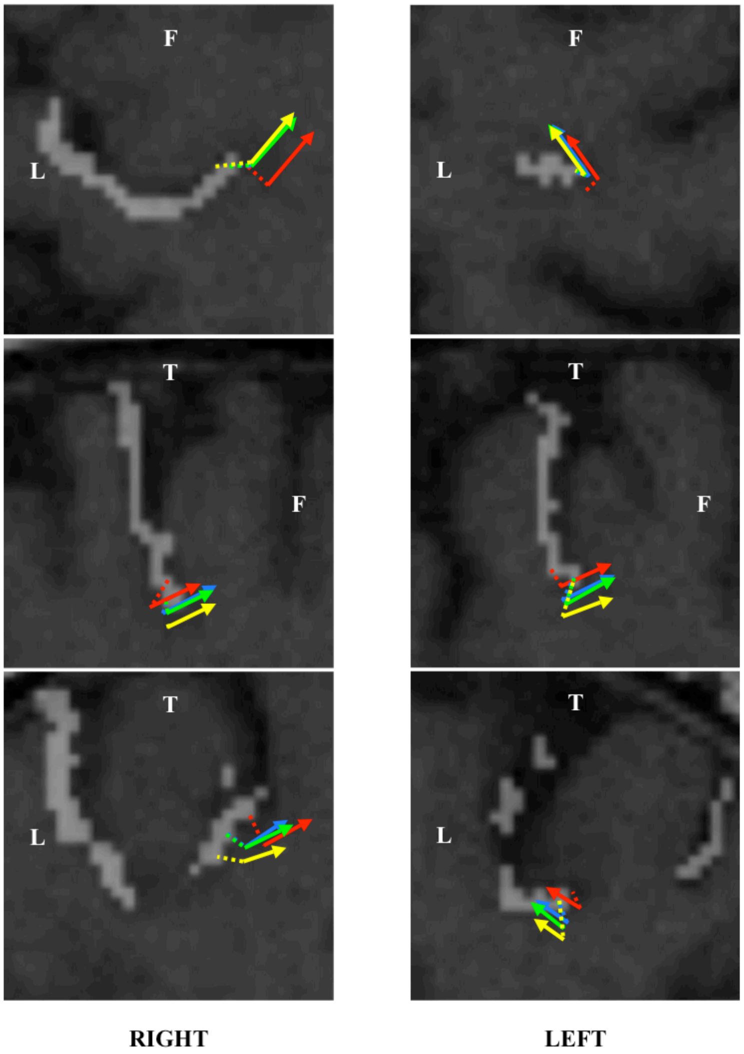

Figure 4.6. N_{20}-P_{20} SEP inverse dipole solutions for right and left median nerve stimulation of Subject C for the CC (Level 1), CV (Level 1), RC (Level 2), and RV (Level Q) approaches compared to the nearest point of the corresponding primary sensory hand areas identified on MRI. Primary sensory hand areas are shown in grey. Red, blue, green, and yellow represent the CC, CV, RC, and RV approaches, respectively. Arrows depict inverse dipole solutions and dashed lines depict dipole position errors projected onto the image plane. Shown are axial (top), sagittal (middle), and coronal (bottom) slices through the median coordinates of the primary sensory hand area points nearest to the inverse dipole solutions. L indicates the left, F the front, and T the top of the subject's head. Note that the distances shown are 2.3 times the actual values. Images are generated using NeuroLens.

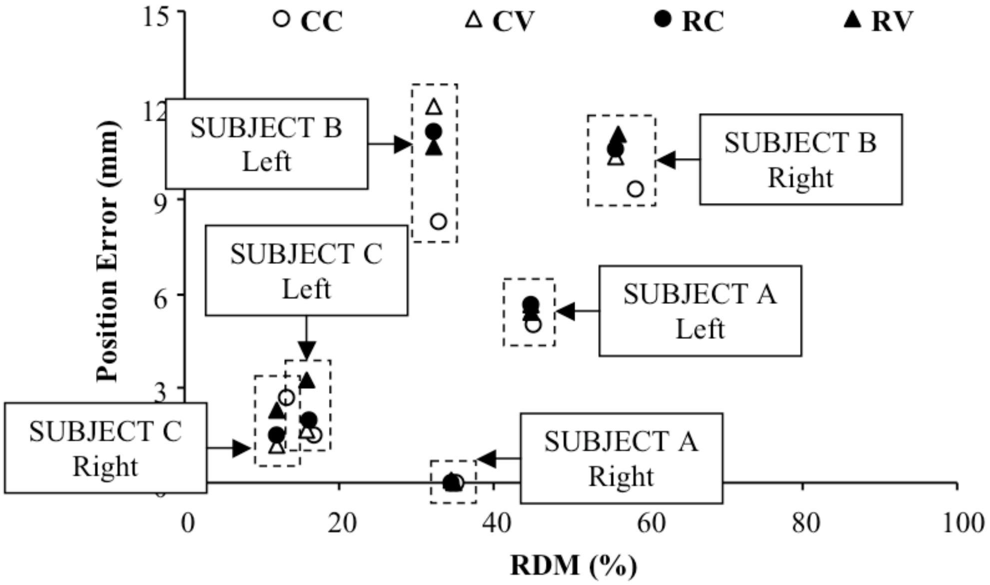

Figure 4.7. Dipole position error in mm versus relative-difference measure (RDM) in % of N_{20}-P_{20} SEP inverse solutions for right and left median nerve stimulation of Subjects A, B, and C. Plotted points are shown for the CC (Level 1), CV (Level 1), RC (Level 2), and RV (Level Q) approaches. The highest RDM values are for right median nerve stimulation of Subject B and the lowest RDM values are for right median nerve stimulation of Subject C. The largest position errors are for right and left median nerve stimulation of Subject B and the smallest position errors are for right median nerve stimulation of Subject A.

localization error does not generally translate to decreased dipole position errors.

For the most part dipole position errors remain reasonable (i.e., below 1.4 cm) even when associated with high minimum RDM values (i.e., above 50%). These findings support previous observations with spherical models, which suggested that there was an inherent robustness of position error with single-dipole inverse solutions to even high RDM values (Finke et al., 2003b). As mentioned in the Introduction, the inaccuracies in forward transfer matrices represented by high minimum RDM values were mainly reflected in the orientation and amplitude of these inverse dipole solutions.

It is important to note that the minimum RDM solution does not always yield the minimum dipole position error among converging simplex trials, but it is essential that this difference in position error remain within an acceptable range for the RDM based simplex minimization to function appropriately. We defined the position error tolerance in Finke et al., 2003b as the greatest improvement in dipole position error by a non-minimum RDM solution when compared to the dipole position error of the minimum RDM solution for a given approach, scalp discretization, and stimulation study. This is essentially a measure of how well the minimum RDM solution yields the most accurate dipole position and depends on forward transfer matrix inaccuracies reflected in RDM values which may to a large extent be unavoidable (e.g., due to noise, volume conductor errors, etc.).

Table 4.5 gives the position error tolerances for the CC, CV, RC, and RV approaches for right and left median nerve stimulation of Subjects A, B, and C. The highest single position error tolerance is 1.1 mm for the RV approach for left median

		POSITION ERROR TOLERANCE (mm)					
		SUBJECT A		**SUBJECT B**		**SUBJECT C**	
		Right	Left	Right	Left	Right	Left
CC	Level 1	0	0.6294	0.6729	0.6809	0.0645	0.2340
	Level 2	0	0.5825	0.7930	0.5346	0.1507	0.0484
	Level 3	0	0.4942	0.5080	0.5585	0.0997	0.1352
CV	Level 1	0.0469	0.2338	0.7983	0.6981	0.0615	0.1038
	Level 2	0	0.0648	0.5606	0.4390	0.0118	0.1024
	Level 3	0.1643	0.0798	0.4080	0.3191	0.0547	0.1438
RC	Level 1	0	0.1806	0.7410	0.6572	0.1227	0.0225
	Level 2	0	0.3238	0.6359	0.2114	0.2687	0.2302
	Level 3	0	0.4838	0.9147	0.7219	0.1782	0.2333
RV	Level Q	0	1.0727	1.0447	0.3559	0.1179	0.1894

Table 4.5. Position error tolerance in mm of N_{20}-P_{20} SEP inverse solutions for right and left median nerve stimulation of Subjects A, B, and C. Position error tolerance is defined as the greatest improvement in dipole position error by a non-minimum RDM solution when compared to the dipole position error of the minimum RDM solution (see text). Level 1, Level 2, and Level 3 discretizations for the scalp surface are used by the CC, CV, and RC approaches while Level Q discretization for the scalp surface is used by the RV approach. Note that if the minimum RDM dipole position error is zero (see Table 4.4) then no further improvement is possible and the position error tolerance is also zero.

nerve stimulation of Subject A. The lowest position error tolerance is zero for right median nerve stimulation of Subject A for those approaches that produce a minimum RDM dipole position error of zero (see Table 4.4) since no further improvement is possible in these cases. Overall the highest position error tolerances are for right median nerve stimulation of Subject B and, excluding the special case for right median nerve stimulation of Subject A mentioned above, the lowest position error tolerances are for right median nerve stimulation of Subject C. This difference in position error tolerance for these two stimulation studies reflects the trends in RDM noted previously (see Table 4.3 and Figure 4.7). No single approach or scalp discretization consistently outperforms the others. Position error tolerances are lower than expected based on simulated potentials on spherical models (Finke et al., 2003b), which found a maximum position error tolerance of 5.2 mm in the presence of noise.

As mentioned above, analysis is also performed at 21 and 23 ms post right and left median nerve stimulation of Subjects A, B, and C. Dipole position errors are smaller in approximately half of the stimulation studies at 21 ms post-stimulation when compared to 22 ms but no overall improvement is noted at 23 ms. In fact clearly distinct dipole solutions several centimeters away are found in multiple stimulation studies especially at 23 ms post-stimulation. The greatest improvement in position error at 21 ms is for right median nerve stimulation of Subject B (i.e., approximately 2 mm versus 10 mm, respectively). Recall that no GFP peaks are found in the interval of interest for Subject B and 22 ms post-stimulation is selected as the time point to be analyzed by default.

Forward filtering is used in an attempt at separating the N_{20}-P_{20} SEP from other neural sources with overlapping electrical activity (see Methods). But as with zero-phase shift filtering, this does not produce a GFP peak during the interval of interest for every stimulation study. Furthermore, even for those studies in which a peak is identified, dipole position errors as well as minimum RDM values are larger overall with forward filtering than with zero-phase shift filtering. For right median nerve stimulation of Subject B, the inverse solutions are even located in areas of the brain clearly not related to N_{20}-P_{20} SEP activity for all approaches and scalp discretizations.

Inverse solutions are also calculated for a relative skull conductivity of 1/80 (i.e., 0.33 S/m for the scalp, 0.0042 S/m for the skull, and 0.33 S/m for the brain/CSF volume conductor). With this conductivity value, simplex convergence becomes an issue for certain stimulation studies (i.e., simplex trials not converging to a minimum RDM value in less than 1000 iterations or converging to a wider range of inverse solutions including to clearly distinct dipole positions). The maximum dipole position error tolerance is also significantly increased to 24.2 mm (versus approximately 1 mm for a relative skull conductivity of 1/15).

Although converging inverse solutions still produce reasonably accurate dipole positions in most cases, in general minimum RDM values are marginally higher with a relative skull conductivity of 1/80 than with the newer relative skull conductivity of 1/15. The maximum dipole position error is now also approximately double at 29.2 mm for the RC approach (Level 3) for right median nerve stimulation of Subject B. Once again, for a given stimulation study, results for converging inverse solutions are similar overall for all approaches and scalp discretizations.

4.6 Discussion

The single-dipole inverse solutions are accurate whether conventional or reciprocal approaches are used. Potential distributions generated by these solutions are consistent with the N_{20}-P_{20} SEPs recorded following median nerve stimulation in our studies and in the literature at large. Dipole position errors remain small, less than 14 mm and around 5 mm on average, and this for all approaches and scalp discretizations. The accuracy of inverse dipole solutions based on scalp potentials has been reported to be in order of 1 cm in general (Cuffin et al., 1991) and for N_{20}-P_{20} SEPs in particular (Buchner et al., 1994a; Buchner et al., 1995a; Gross et al., 2000). Not much separates the different approaches in terms of inverse solution characteristics. However only a limited number of data sets are studied.

Numerical differences between measured and calculated potentials, reflected by high minimum RDM values, are mostly irrelevant due to the robustness of dipole position error to inaccuracies in forward transfer matrices. The nonlinear nature of the single-dipole inverse solution results in dipole position that is relatively insensitive to volume conductor inaccuracies that mainly affect the linearly determined dipole orientation and amplitude (Finke et al., 2003b). Scalp discretization modifications aimed at reducing these volume conductor inaccuracies, and therefore RDM values, such as increasing the number of elements used (see Table 4.1) and decreasing electrode localization errors (see Table 4.2), do not necessarily translate into improved dipole position error.

As such even more accurate determinations of forward transfer matrices, for example via linear Galerkin (Mosher et al., 1999b) or second-order interpolation (Frijns et al., 2000), or by interpolating projected electrode sites to those assumed in the different approaches, are not expected to improve dipole position further. If however linear solutions consisting of cortical surface potentials or the amplitudes of a fixed layer of cortical dipoles are of interest, then more accurate forward transfer matrices should still improve these types of inverse solutions. Note that a minimum level of precision in volume conductor discretizations and forward transfer matrices is still required for dipole position not to be adversely impacted (Buchner et al., 1995b).

With the reciprocal approaches, electrode sites are used for current injection and withdrawal and thus large potential gradients are generated around these sites. Volume conductor discretizations for reciprocal approaches have therefore typically been refined in the vicinity of electrode sites in order to decrease inaccuracies in the forward transfer matrices resulting from otherwise inadequate modelization of these gradients. Although here only scalp discretizations are modified in this manner, refinement previously included the underlying skull and brain/CSF discretizations as well (Fletcher et al., 1995; Finke and Gulrajani, 2001; Finke et al., 2003b). However, considering that neither refinement around electrode sites on the scalp surface (Level 2 and 3) nor higher-order potential interpolation at these sites (Level Q) improve dipole position error because of its inherent robustness, it is likely that additional selective refinement of the skull and brain/CSF surfaces would also yield limited returns.

With a relative skull conductivity value of 1/15, all simplex trials converge in less than 1000 iterations and almost all converge around the global RDM minima. This minimum RDM criterion used to pick the inverse dipole solution amongst converging simplex trials is correct to within a small position error tolerance largely determined by measurement noise and inaccuracies in the volume conductor model including skull conductivity error. As such dipole position error tolerance (i.e., the difference between the minimum RDM position error and the absolute minimum position error) is more closely related to RDM than dipole position error itself, but still remains reasonable at approximately 1 mm or less even with high minimum RDM values. In fact position error tolerances are lower than expected based on simulated potentials on spherical models (Finke et al., 2003b).

Inverse solutions with the more recent higher relative skull conductivity value of 1/15 yield smaller position errors in general than with a conductivity of 1/80. This latter presumably less realistic conductivity ratio also corresponds to an overall increase in convergence related difficulties, minimum RDM values, and position error tolerances. Although reciprocal approaches had shown some degree of relative invariance to conductivity errors in forward transfer matrices (Finke and Gulrajani, 2001), this does not translate to improved dipole position error in inverse solutions. A similar conclusion was reached for simulated data on spherical models in the presence of noise (Finke et al., 2003b). The fact that reasonably accurate inverse solutions are obtained in most cases with two widely different skull conductivity values is again attributable to the nonlinear relationship between dipole position and forward transfer matrices.

The accuracy of inverse solutions is dependent on the exact time point analyzed. Selecting time points based on GFP peaks is not possible in every study and in some cases different time points produce smaller dipole position errors. In fact those studies that produce the largest dipole position errors are those that do not have a distinct GFP peak (i.e., right and left median stimulation for Subject B). This most likely reflects the presence of significant overlapping electrical activity from non N_{20}-P_{20} SEP related neural sources at the time points analyzed such as the earlier subcortical SEPs. An attempt at separating the N_{20}-P_{20} SEP from other neural sources using forward filtering did not reliably lead to more accurate inverse solutions.

This underlines the fundamental limitation of the single dipole, single time point source model in reproducing realistic EEG data. It suggests that including more than one time point in the analysis, such as in spatio-temporal dipole solutions, or including more than one source model, such as in multiple-dipole solutions, may improve dipole position further at the cost of increased solution parameter space. However this is still contingent on analyzing the appropriate time points and modeling the appropriate number and type of sources. To this end multiple signal classification (MUSIC) (Mosher et al., 1992) and independent component analysis (ICA) (Richards, 2004) are also options. Although analysis is only performed here for a single dipole at a single time point, both reciprocal and conventional approaches are applicable to these alternative formulations and the robustness of dipole position error may still hold true in these cases. However this remains to be validated.

Although generation of forward transfer matrices initially calculated only in part takes longer for reciprocal approaches than for conventional approaches (Finke and Gulrajani, 2001), inverse solutions take significantly less time for reciprocal approaches (i.e., less than approximately one third of the time required by the CV approach and 1/12th of the time required by the CC approach). Furthermore, storage requirements for these partially predetermined matrices are also significantly smaller for reciprocal approaches (i.e., less than approximately 1/25th of the memory required by the CV approach and 1/100th of the memory required by the CC approach). For a given volume conductor discretization, partial transfer matrix generation is only required once initially after which inverse solutions can be repeatedly calculated for different potential distributions, time points, and source models.

Note that modifications to both the conventional and reciprocal approaches that may further reduce computational requirements are possible. For the former approach, with an additional step in the generation of forward transfer matrices, potentials can be calculated exclusively at electrode sites on the scalp surface (Fletcher et al., 1995). For the latter approach in which derivatives of the surface potential with respect to source location are available, minimization techniques that exploit these derivatives to accelerate convergence, such as Levenberg-Marquardt (Marquardt, 1963), can be employed. These variants, however, are not typically used in BEM-based dipole source localization and require further validation.

In terms of choosing between the two reciprocal approaches, the RV approach requires less partial matrix generation time and storage space since, for a given discretization, the number of nodes is approximately half the number of elements and, therefore, the RV approach solves for and stores half the number of unknowns. On the other hand the RV approach necessitates discretization modification around each electrode site (see Methods), which represents an additional step than for the RC approach that can use unmodified Level 1 scalp discretizations. Overall decreased time and storage requirements with similar dipole position accuracy for the reciprocal approaches facilitates their application to a larger number of studies, as well as their comparison to other imaging modalities including MEG, functional MRI, and PET or a combination of the above (Buchner et al., 1994b).

Finally dipole position error calculations are fundamentally limited by their reliance on anatomical landmarks identified on MRI. Essentially the electrical origins of measured potentials on the scalp, in the form of inverse dipole solutions, are compared to cortical structures presumed to contain these neural sources. The true relationship between functional and anatomical localization is unclear for any given stimulation study and some degree of inter-subject and inter-observer variability is to be expected (Sobel et al., 1993; Kennedy et al., 1998). As there exists no ideal single, non-invasive localization strategy for the primary sensory hand area, greater confidence in its correct identification can be obtained from the convergence of multiple independent techniques including EEG inverse solutions. Further validation of single-dipole inverse solution accuracy can also be obtained from comparisons with actual intra-cerebral recordings.

4.7 Conclusion

Both reciprocal and conventional approaches for single-dipole inverse solutions are validated for N_{20}-P_{20} SEPs. Reciprocal approaches have similar solution profiles including small dipole position errors when compared to the nearest point of the primary sensory hand area identified on MRI. Position error for single-dipole inverse solutions is inherently robust to inaccuracies in forward transfer matrices but intrinsically dependent on the overlapping activity of other underlying neural sources. Smaller time and storage requirements remain the principal advantages of the reciprocal approaches and they are equally applicable to alternative inverse solutions such as spatio-temporal and/or multiple dipole localization, MUSIC, and ICA. Future work involves comparing reciprocal and conventional approaches on a larger number of stimulation studies and with intra-cerebral electrode recordings, as well as other imaging modalities including MEG, functional MRI, and PET or a combination of the above.

Chapter 5 Discussion

The forward problem (Chapter 2) is discussed in Section 5.1 while the inverse problem (Chapters 3 and 4) is discussed in Section 5.2. Finally, areas where further research is required are discussed in Section 5.3.

5.1 Forward Solutions

Boundary-element method (BEM) equations for the conventional centroid (CC), conventional vertex (CV), reciprocal centroid (RC), and reciprocal vertex (RV) approaches to the EEG forward problem are derived using a weighted-residual formulation, and details of their numerical implementation are described for a fairly general volume conductor geometry. These approaches are validated on a three-concentric-spheres head model consisting of planar triangles assuming either a constant (CC and RC) or linear (CV and RV) potential variation on those triangles as well as flux variation for the reciprocal approaches. Similar surface discretizations with selective refinement around electrode sites are used for all four approaches, but an additional curvilinear quadrilateral with quadratic interpolation is inserted at each electrode for the RV approach. Calculated scalp potentials are compared with simulated, analytic potentials using the relative-difference measure (RDM) for radial and tangential dipoles of varying eccentricity and two very different skull conductivity values. Both conventional and reciprocal approaches exhibit large errors for highly eccentric dipoles, whereas the CV approach is more accurate for less eccentric dipoles when using the more realistic skull conductivity value of 1/15. Reciprocal approaches demonstrate less variation in forward solution accuracy with alterations in skull conductivity values.

5.1.1 Skull Conductivity

Since the low relative conductivity of the skull is known to attenuate surface potentials on the scalp rendering them susceptible to numerical errors, improved accuracy in scalp potentials is to be expected when increasing skull conductivity from the usually employed value of 1/80 to the value of 1/15 suggested by more recent work. This is indeed the case for the CV approach. However, for the CC approach, scalp potential accuracy is unexpectedly diminished with this increase in skull conductivity. Whereas the assumption of a constant potential on each triangle is sufficient to model the attenuated scalp potentials resulting from a low skull conductivity of 1/80, the greater spatial variability of the surface potentials on the scalp produced by the higher skull conductivity of 1/15 renders this assumption less valid especially for radial dipoles. A finer discretization is used for the CV approach than for the CC approach (see Section 5.1.2), which also allows a more accurate modelization of the greater variation in scalp potentials produced by the higher skull conductivity.

In contrast to the conventional approaches, the RDM curves for the reciprocal approaches are relatively unaffected by the above change in skull conductivity. Errors in scalp potentials produced by the reciprocal approaches inherently remain proportional to the larger scalp potential magnitude associated with this increase in skull conductivity. This apparent stability also holds true for RC approach where the assumption of a constant potential and the smaller number of discretization elements do not limit the accuracy of scalp potentials produced using the higher skull conductivity value of 1/15 as it did for the CC approach. Note that all approaches still produce large errors in scalp potentials for very eccentric dipoles even with the newer, higher skull conductivity. The CC, CV, RC, and RV approaches all improve with increasing discretization and, as eccentricities increase, higher order interpolation and an even finer discretization should improve potentials still further by achieving a more accurate match of their variation on the scalp, especially for a skull conductivity of 1/15.

5.1.2 Numerical Considerations

As expected, the accuracy in scalp potential calculations for all approaches improves with increasing discretization. This is especially true for eccentric, radial dipoles that tend to produce the largest RDM values, but these values still remain elevated even for a large number of discretization elements (i.e., over 7500 total). Although not the focus of this thesis, prior work (Finke, 1998) demonstrated diminishing returns, as the number of discretization elements was increased further and further. For eccentric, radial dipoles in particular, less variation in accuracy with increasing discretization was found for the reciprocal approaches than for the conventional approaches. This may be due at least in part to the transfer of source currents with the reciprocal approaches from unknown dipole positions to known electrode sites where the discretization may be selectively refined. No attempt is made here at determining the optimal number of discretization elements for a given source model, head model, and forward solution approach, but rather comparable levels of discretization to those found in the current literature are chosen.

In a triangular discretization the total number of triangle vertices is approximately half the total number of triangles or triangle centroids. So when comparing the respective centroid and the vertex approaches for a similar number of unknowns (i.e., potentials for the conventional approaches and potentials and fluxes on the inner surfaces for the reciprocal approaches), then the vertex approaches can be used on a head model with approximately twice as many discretization elements. Alternatively, if we compare approaches using similar volume conductor discretizations, then the vertex approaches solve for approximately half the number of unknowns for both the conventional and reciprocal approaches, respectively. Considering conventional and reciprocal approaches separately, centroid and vertex approaches can therefore be compared for either a similar number of unknowns or a similar number of discretization elements.

Furthermore, the number of unknowns for which the reciprocal approaches solve is almost twice as high as for their conventional counterparts (i.e., centroid and vertex approaches, respectively). Potentials and fluxes are determined with the reciprocal approaches as opposed to potentials only with the conventional approaches, except on the outermost scalp surface where the fluxes are known for the reciprocal approaches (i.e., unit current is injected and withdrawn at the electrode sites with all other sources assumed to be zero). So for a fixed number of discretization elements, the approximate relationship between the number of unknowns for the different approaches is as follows: RC ≈ 2 x RV ≈ 2 x CC ≈ 4 x CV. Conversely, if an attempt is made to match the number of unknowns, then the relationship between the number of elements that may be used by each approach is as follows: CV ≈ 2 x CC ≈ 2 x RV ≈ 4 x RC.

For our results using potential simulations on spheres, the centroid and vertex approaches are compared for a similar number of unknowns but using different discretizations. However, comparing them in this manner does not allow us to distinguish between differences in accuracy solely due to interpolation order versus discretization level. In terms of comparing conventional and reciprocal approaches, no attempt is made at compensating for the difference in the number of unknowns. When more realistic BEM head models are considered, then generating multiple discretizations in an attempt at matching the number of unknowns for the different approaches becomes increasing problematic. Conventional and reciprocal centroid and vertex approaches on these more realistic volume conductors are compared for a similar number of discretization elements and hence solve for a different number of unknowns. This difference is the principle determinant of computational time requirements for the generation of forward transfer matrices, requirements that therefore follow the relationship between the number of unknowns for the different approaches given above: RC ≈ 2 x RV ≈ 2 x CC ≈ 4 x CV.

In previous work (Finke, 1998) with a skull conductivity of 1/80, when the CC and the CV approaches were compared on spherical models using the same number of triangles, scalp potential accuracy improved even further for the CC approach when compared to the CV approach. This is not surprising considering that the relative number of triangles used with the CV approach was essentially decreased and the CC approach already outperformed the CV approach when the latter was using twice as many triangles. With a skull conductivity of 1/15 for which the CV approach is more accurate than the CC approach, it is expected that this difference in accuracy between the two approaches will decrease. Comparing centroid and vertex reciprocal approaches with a skull conductivity of 1/80, very little difference was found for eccentric dipoles when using a similar number of discretization elements versus adjusting for the number of unknowns. Adjusting the number of discretization elements for the difference in the number of unknowns between conventional and reciprocal approaches, some quantitative differences were found but the relative order of the different approaches in terms of accuracy remained unchanged.

Whether comparing approaches for a similar number of unknowns or a similar number of discretization elements, the centroid approaches generally outperform the vertex approaches with a skull conductivity of 1/80 for the conventional approaches and with both conductivity values for the reciprocal approaches except at high eccentricities. This is counterintuitive as a higher order of interpolation (i.e., linear and quadratic versus constant) is expected to improve scalp potential accuracy. One possible explanation is that, for both centroid approaches (i.e., CC and RC), the simulated, analytic potential at a triangle centroid is determined by averaging the analytic potentials at the three vertices of that triangle. Since the centroid is actually lying inside the surface being modeled, this approximation systematically underestimates the absolute potential magnitude. This error factor is increased when the number of elements is decreased and/or when the potential gradients are increased (i.e., when the dipole is more eccentric and radial, when the skull conductivity is higher, etc.).

This error in the calculation of analytic potentials on spherical models exclusively affects the centroid approaches and can either improve or worsen RDM values when comparing analytic to numerical potentials depending on the exact source and head model. If for example the overall effect of numerical inaccuracies in our forward calculations leads to either a net over- or underestimation of scalp potentials, this will result in either relative worsening or improvement, respectively, of the RDM for the centroid approaches. The unexpected, relatively lower RDM values for the centroid approaches in the cases mentioned previously may indeed be due in part to this error in simulated potentials. Ferguson and Stroink (1997) suggested that the volume we are modeling should actually be entirely contained within the surface discretizations to improve results. However, this is difficult to do in practice since surfaces are generally discretized using triangle vertices. Note that this error is intrinsic to simulated potentials on spheres and not to the centroid approaches themselves, and as such is not present when numerical potentials are compared to measured potentials instead of analytic potentials.

The auto solid angle calculation is also a potential source of numerical error for the vertex approaches as it is not as easily determined as for the centroid approaches. However, attempts at improving scalp potentials for the CV approach by modifying auto solid angle calculations (Meijs et al., 1989; Heller, 1990; Wischmann et al., 1996) were beneficial mostly when a relatively low number of discretization elements where used (Finke, 1998). In fact, even then the only improvements seen were on the innermost cortical surface for eccentric dipoles. Again, this corresponds to large potential gradients unattenuated by skull conductivity modeled by relatively few discretization elements. These results on the innermost surface of the three-concentric-spheres model can be compared to those of Ferguson and Stroink (1997) for a single-homogenous-sphere model (see Section 5.1.3) that also demonstrated some improvement. Straightforward implementation of these suggested corrections is not possible with the RV approach owing to the presence of quadrilaterals in the discretization. Furthermore, these modified auto solid angle calculations are intended for spherical models only and may actual worsen results for head models for which they are not intended (Ferguson and Stroink, 1997).

Even though the centroid approaches appear more accurate in certain cases, the assumption of a constant potential (and flux for reciprocal approaches) becomes less adequate when scalp potential gradients increase. First of all, with the conventional approaches, if we consider a skull conductivity of 1/80 for which the CC approach is generally more accurate than the CV approach, the difference between the two approaches is the least pronounced for eccentric, radial dipoles. With a skull conductivity of 1/15, the CV approach is more accurate than the CC approach in general. For the reciprocal approaches, the RC approach is more accurate than the RV approach except for highly eccentric dipoles whether a skull conductivity of 1/80 or 1/15 is used. Furthermore, regardless of the approach considered, RDM values are high for eccentric dipoles especially if they are radial. Since a higher skull conductivity of 1/15 is considered more realistic and most clinical applications involve eccentric dipoles, forward solution accuracy in the case of significant scalp potential gradients is of particular interest.

The BEM volume conductors' ability to model greater variation in surface potential can be improved by increasing the number of discretization elements and/or increasing the order of interpolation on those elements. In general the greater the number of elements used, the lower the order of interpolation required and vice versa. Therefore increasing the order of interpolation is mostly of interest when attempting to compensate for a level of discretization that is inadequate for a given potential gradient. As previously mentioned, this becomes an issue especially when the potential gradients are high (i.e., for the innermost cortical surface, for eccentric, radial dipoles, for a higher skull conductivity). Several modifications to the BEM interpolation order are possible (Mosher et al., 1999b; Pullen, 1996; Fischer et al., 1999; Gençer and Tanzer, 1999; Frijns et al., 2000), but they generally come at the expense of a greater number of nodes per element and, hence, a greater number of unknowns and longer computation times. For example, curvilinear quadrilaterals with quadratic interpolation (i.e., nine nodes per element) may be used throughout the surface discretizations rather than just over the electrode sites. An analytic expression for quadratic potential interpolation on a triangle (i.e., six nodes per element) also exists (de Munck, 1992).

Discretization Refinement

In our results for spherical head models, local discretization refinement of all three surfaces in the vicinity of the scalp electrodes is used for all four approaches. Although this type of refinement is specifically aimed at exploiting the reciprocal formulation, locally refined discretizations are used for all approaches as to minimize any biases that differing discretizations may introduce when comparing their accuracy (compensating for the different number of unknowns between the centroid and vertex approaches aside). However, smaller planar triangles are used for the CC, CV, and RC approaches with either constant or linear interpolation of surface potentials and fluxes, while curvilinear quadrilaterals with a higher order, quadratic interpolation are used as well for the RV approach. It is expected that this local refinement will especially affect the reciprocal approaches, where current is injected and withdrawn at the electrode sites and hence produce very high potential gradients. No attempt is made here at determining the optimal configuration of discretization elements around the electrode sites for a given source model, head model, and forward solution approach, but it is expected that a greater local density of elements and/or a higher order of interpolation on those elements will again improve results, especially for the reciprocal approaches.

Indeed, the RV approach, using curvilinear quadrilaterals with quadratic interpolation at the electrode sites, has previously been found to improve accuracy for highly eccentric dipoles. These results were obtained with a skull conductivity of 1/80, when comparing results with either those of the CV approach (Fletcher et al., 1995) or the CC, CV, and RC approaches (Finke, 1998) on evenly discretized spheres (i.e., no selective refinement). The approaches were also compared with dipoles along different axes including an axis intersecting the head model surfaces in an area of relative discretization refinement. Accuracy for highly eccentric dipoles is improved by both the RV approach with selective discretization refinement around the electrode sites, and the use of local discretization refinement along the dipole axis. Even in the latter case, the RV approach remained more accurate for highly eccentric dipoles. Not much difference was found between the CV and RV approaches for less eccentric dipoles, but in Finke (1998) the centroid approaches (CC and RC) were found to be more accurate in this case (see above).

In our results here, the centroid approaches (CC and RC) are also more accurate for less eccentric dipoles with a skull conductivity of 1/80. Again not much difference is found between the CV and RV approaches at these eccentricities. With a skull conductivity of 1/15, the CV and RC approaches are more accurate for less eccentric dipoles. But, contrary to previous findings, no clear improvement is found for the RV approach for highly eccentric dipoles with either skull conductivity, except when comparing accuracy between reciprocal approaches (RC and RV). For all approaches, including the RV approach with quadratic, curvilinear quadrilaterals at the electrode sites, RDM values remain large for highly eccentric dipoles. As already mentioned, and again contrary to previous studies, similar discretizations with selective refinement around electrode sites are used for all approaches in order to minimize any biases related to the use of differing discretizations.

Somewhat surprising is the relatively accurate results obtained with the RC approach, even without local refinement around the electrode sites (Finke, 1998), especially considering the current injection and withdrawal at these sites. This unexpected accuracy is due to the factors described above for the centroid approaches and disappears as the dipoles become highly eccentric. Even when both the RC and RV approaches are compared with local refinement around electrode sites, the RC approach is still less accurate than RV approach for highly eccentric dipoles suggesting that interpolation may still be important in this case. It remains unclear, however, whether this difference in accuracy is due to local interpolation at the electrode sites as opposed to the overall interpolation throughout the discretization. Regardless, the effect of local refinement and interpolation around electrode sites appears less dramatic in our work than anticipated based on theoretical considerations and previous results.

There are multiple factors that explain the differences between our results here and those previously shown for highly eccentric dipoles (see Section 5.1.3). For one, in Fletcher et al. (1995) and in our previous work (Finke, 1998), local electrode refinement was exclusively used for the RV approach. This does not allow us to distinguish between the effects of selective electrode refinement specifically and, for example, those resulting from the use of an overall greater number of discretization elements. Furthermore, in our previous work (Finke, 1998), dipoles were displaced along an axis that intersected an electrode site and, hence, an area of greater discretization for the RV approach. As selective electrode refinement was present on all three surfaces, eccentric dipoles were essentially located just below an area of increased discretization and interpolation for the RV approach. This improves results regardless of the approach and it becomes difficult to distinguish between the effects of selective electrode refinement and those resulting from the local refinement of the discretization along the dipole axis. The axis along which the dipole is moved in the results shown here is chosen to intersect the outside sphere approximately equidistant from four contiguous electrodes in an area of intermediate discretization (i.e., at 45º) in order to avoid this special case.

To reduce computational requirements, we generally try and limit the number of discretization elements and the order of interpolation used. The modifications described above are mostly of interest when attempting to compensate for a level of discretization that is inadequate for a given source and head model (i.e., for a given potential gradient). For the number of discretization elements used in our studies, interpolation does indeed have an impact especially for highly eccentric dipoles. Increasing the overall number of discretization elements will always improve results, but increasing the order of interpolation and/or selectively refining the discretization may also similarly improve accuracy but potentially at a lower computational cost. Refining surface discretizations exclusively in the vicinity of the source dipole has been shown to improve scalp potential accuracy (Meijs et al., 1989; Fletcher et al., 1995; Schlitt et al., 1995; Yvert et al., 1995; Finke, 1998; Fuchs et al., 1998a), but this is often not possible in the inverse problem when dipole position is usually not known a priori. It remains unclear in our work whether or not selective discretization refinement in the vicinity of electrode sites truly improves scalp potential accuracy for the reciprocal approaches as it was previously suggested. The optimal BEM configuration of element number, interpolation, and local versus overall discretization refinement in terms of computational cost and scalp potential accuracy is unknown, and it is inherently dependent on the exact source model, skull conductivity, and forward solution approach under consideration.

Other Factors

Otherwise, no attempt is made to use equilateral or nearly equilateral triangles in our spherical models, although this has been shown to improve accuracy (Ferguson and Stroink, 1997), so as to better mimic the realistic BEM head model situation where such optimization may not be possible. Similarly, no attempt is made at aligning the vertices of the different surface discretizations with one another. Finally, accuracy was improved only marginally when analytic expressions for solid angle calculations were used instead of numerical integration (Finke, 1998). This is partially due to the large number of integrations points considered (i.e. 13 for triangles and 144 for quadrilaterals). To reduce computational time requirements, we generally try and limit number of integration points used, as well as the number of discretization elements and the order of interpolation for those elements, and analytic expressions for solid angle calculations are therefore preferred. Note that in the reciprocal approaches, analytic expressions for certain calculations, including flux and the electric field, are not available and numerical integration is still required in these cases.

5.1.3 Scalp Potential Accuracy

The CC approach produces smaller errors in scalp potentials than the CV approach with a relative skull conductivity of 1/80 except at high eccentricities (see

Section 5.1.2), which supports the observations of others (Schlitt et al., 1995; Mosher et al., 1999b). In contrast, if we consider the potentials on the innermost cortical surface in the three-concentric-spheres head model, then the CC approach yielded larger errors than the CV approach (Finke, 1998). This is also supported by the literature (Schlitt et al., 1995). Ferguson and Stroink (1997) found that the CV approach was more accurate on single-surface volume conductors but, considering the low skull conductivity, their single surface corresponds more to the innermost sphere in the three-concentric-spheres model than the outermost sphere. Whereas the assumption of a constant potential on each triangle is sufficient to model the attenuated scalp potentials resulting from a low skull conductivity of 1/80, the greater spatial variability of the surface potentials on the cortex renders this assumption less valid especially for eccentric dipoles. Even though cortical potentials are important in certain applications such as magnetic field calculations (Schlitt et al., 1995), the inverse problem in electroencephalography only requires potentials on the outermost scalp surface of the volume conductor. Note that these findings no longer necessarily hold true with a skull conductivity of 1/15 or for the reciprocal approaches.

Fletcher et al. (1995) reported much smaller error values for scalp potentials using a normalized median-error measure than those we find using the relative-difference measure (RDM). In our own simulations, using such a measure of error generally results in values that are, on average, half of those of the more usual RDM and considerably less than half for highly eccentric dipoles. To explain this difference, consider the case of an eccentric dipole where only the few electrodes close to the dipole exhibit large errors. The median-error measure reflects the relatively smaller error at one of the other electrode sites whereas the RDM is a reflection of error at all electrodes including the significant contribution from those electrodes nearest to the dipole. In our previous work (Finke, 1998), a normalized maximum-error measure was used and this may also explain, to some extent, the differences in results between our work here and previous findings. Even though these three error measures produce quantitatively different results, they remain comparable qualitatively including with respect to the relative accuracy of the different approaches, except for highly eccentric dipoles. Note that the RDM is the more commonly used error measure in the literature for both forward and inverse solutions.

Several other factors may influence scalp potential accuracy when comparing our results with those of previous studies (see Section 5.1.2), especially for highly eccentric dipoles. Curvilinear quadrilaterals with quadratic interpolation at electrode sites aside, curvilinear quadrilaterals with linear interpolation were used throughout the surface discretizations in Fletcher et al. (1995) instead of planar triangles with linear interpolation as in our studies. It has also been previously shown that some variability in RDM curves is to be expected as the axis along which the dipole is moved changes (Fletcher et al., 1995; Schlitt et al., 1995; Ferguson and Stroink, 1997). In our simulations, this change in axis results in some quantitative variation but no qualitative changes to our findings for both forward and inverse solutions. Obviously there are also differences between studies in terms of the exact electrode sites considered and the relative sizes and distribution of the discretization elements used in the local refinement around these electrodes. Higher dipole eccentricities are considered in our work when compared to Fletcher et al. (1995) (8.65 cm or 99.4% versus 8.61 cm or 99%, respectively), leading to seemingly larger RDM values at higher eccentricities. A smaller number of discretization elements were also used for the RV approach in Fletcher et al. (1995), corresponding to less than half the total number of nodes when compared to our head models. As previously mentioned, a smaller number of discretization elements may increase the reliance of forward solution accuracy on interpolation order and, potentially, on selective electrode refinement for reciprocal approaches, especially when surface gradients are high (e.g., for highly eccentric dipoles).

With a low skull conductivity of 1/80, Hämäläinen and Sarvas (1989) demonstrated that the skull attenuated scalp potentials to such an extent that standard, conventional forward solutions were rendered inaccurate. They suggested a two-step isolated-problem implementation in which cortical potentials were initially calculated assuming the skull to be perfect insulator, and then adding a correction factor to these isolated cortical potentials so as to obtain the surface potentials with the low skull conductivity in place. This led to much more accurate scalp potentials especially for eccentric dipoles. This isolated-problem implementation is used by us but does not appear to have been used by Fletcher et al. (1995). In fact their utilization of an accelerated conventional approach that only solves for scalp potentials at electrode sites seems to preclude the use of this two-step implementation. This significantly impacts the relative accuracy of our respective conventional approaches when comparing them to reciprocal approaches, as is indeed the case for highly eccentric dipoles. While increasing the skull conductivity from 1/80 to 1/15 renders the use of the isolated-problem implementation less critical, our preliminary results (not shown here) indicate that it is still required for accurate scalp potential calculations. Regardless, since a skull conductivity of 1/80 mandates the use of the isolated-problem implementation, this implementation is also used with the higher skull conductivity of 1/15 as to allow an unbiased comparison. Issues surrounding the isolated-problem implementation are discussed further in Section 5.3.

Straightforward interpretation of the effects of highly eccentric dipoles on the reciprocal approaches is impossible. Not only must the large potential gradients be taken into account but also the flux on the discretization surfaces although this is likely less critical (i.e., flux is related to the potential gradient). The RV approach outperforms the RC approach for highly eccentric dipoles, but it remains unclear whether this improvement is the result of increased interpolation order throughout the discretization, or the result of local refinement and interpolation exclusively around the electrode sites. Surface potentials and fluxes are initially calculated assuming unit current injection and withdrawal at the electrodes sites and, hence, selective discretization refinement and interpolation is expected to improve our ability to model the resulting large gradients around those sites. But the electric field at the dipole position in question is then calculated using only the potential and flux on the innermost cortical surface. Indeed, for an eccentric dipole position close to that surface, local discretization refinement and interpolation in the vicinity of the dipole may still potentially affect accuracy as it does with the conventional approaches. The reciprocal approach is essentially a completely different formulation to the forward problem making its results difficult to predict. One unexpected byproduct of this formulation is the reciprocal approach's relative invariance in accuracy with two very different skull conductivity values. Even with the conventional approaches, interpretation of the effects of highly eccentric dipoles is complicated by the use of a two-step isolated-problem implementation. Note that there exists a different reciprocal solution (Riera and Fuentes, 1998) in terms of current fluxes at the BEM elements that gives the electric field without recourse to the gradient of the potential.

However, this alternative solution, as well as the quantification of the relative influences of local versus overall discretization refinement, is not the focus of this thesis.

Interpretation of forward solution accuracy is also limited by the use the RDM, which does not allow the distinction between errors in surface potential amplitude and those related to topography. Although not shown in this thesis, topographical maps for both conventional and reciprocal approaches are similar to those produced by the corresponding analytic solutions. RDM values mostly reflect errors in potential amplitude instead of errors in form or symmetry especially for highly eccentric dipoles where these values exceed 100%. The relative errors in amplitude are most significant for those electrodes nearest to the dipole under consideration where the absolute potential values are largest. However even in these cases the topography is relatively preserved. Greater insight could be gained by comparing conventional and reciprocal approaches, as well as the different skull conductivities, specifically in terms of topographical distributions. For example, the form and symmetry of the calculated surface potentials can be compared to the analytic surface potentials numerically using a correlation coefficient. Subtle differences between approaches, especially for highly eccentric dipoles where differences are expected, may be brought to light that are otherwise not apparent by simply considering the RDM. As previously mentioned, the RDM is the error measure typically found in the literature when estimating EEG forward solution accuracy. The RDM is considered here, as it is also the error measure frequently minimized in EEG inverse solutions, which is of principal interest in this thesis. Although it could be argued that since forward solution errors are predominantly in potential amplitude instead of topography, it should not be surprising that inverse solution errors are mostly in dipole amplitude instead of dipole position, the nonlinear nature of the single-dipole inverse problem still limits this type of prediction (see Section 5.2). Another aspect that limits the interpretation of forward solution accuracy is the number of electrodes used in the simulations on spherical models. Although the sampling provided by 42 electrode sites is consistent with the number of electrodes typically used in the literature at the time and is adequate for most test dipoles, it may be less so for highly eccentric dipoles that result in potential distributions with higher spatial frequency components. Again, small differences between approaches and skull conductivity values may become apparent for these dipoles if a greater number of electrodes are used. Regardless, considering the equivalency of approaches in terms of inverse solution accuracy, the selection of an alternative measure of forward solution accuracy or a greater number of surface electrodes is unlikely to modify the final conclusions presented here.

In the next section, the effects of highly eccentric dipoles and the resulting large RDM values, the effects of BEM head model discretization and interpolation, and, finally, the effects of the reciprocal approaches themselves, particularly with respect to skull conductivity, are examined in terms of inverse solutions.

5.2 Inverse Solutions

In numerical simulations on a BEM three-concentric-spheres head model, single-dipole EEG inverse solutions are obtained for the CC, CV, RC, and RV approaches. Surface discretizations consist of planar triangles assuming either a constant (CC and RC) or linear (CV and RV) potential variation on those triangles as well as flux variation for the reciprocal approaches. Similar surface discretizations with selective refinement around electrode sites are used for all four approaches, but an additional curvilinear quadrilateral with quadratic interpolation is inserted at each electrode for the RV approach. Inverse dipole solutions are calculated using simplex minimization of the RDM for radial and tangential dipoles of varying eccentricity and two different values of skull conductivity. Analytic scalp potentials are also determined with 10% and 20% white Gaussian noise and with a skull conductivity of 1/15±25%. Inverse solution accuracy is compared in terms of dipole amplitude, orientation, and position. Both conventional and reciprocal approaches yield inverse solutions of comparable accuracy and position errors are low even for highly eccentric dipoles that result in large RDM values. Conventional and reciprocal approaches are also found to be equally robust to skull conductivity errors in the presence of noise.

Single-dipole inverse solutions are also performed on real EEG data for the CC, CV, RC, and RV approaches. Bilateral median nerve stimulation is performed on three subjects and inverse solutions for the N_{20}-P_{20} somatosensory evoked potentials (SEPs) are then obtained by simplex minimization. Inverse dipole position is validated against the primary sensory hand area identified on MRI. Solutions are presented for different time points, filtering strategies, skull conductivity values, and BEM discretizations. Realistically shaped head models including scalp, skull, and brain/CSF surfaces are generated from individual MRIs with the 129 electrode sites considered projected onto the scalp surface. Similar scalp surface discretizations consisting of planar triangles with and without selective refinement around electrode sites on the scalp are used for the CC (constant potential), CV (linear potential), and RC (constant potential and flux) approaches, but an additional curvilinear quadrilateral with quadratic interpolation is inserted at each electrode for the RV approach (linear/quadratic potential and flux). Discretizations for skull and brain/CSF surfaces are identical for all approaches. Both conventional and reciprocal approaches produce similarly small dipole position errors. Indeed, position errors for single-dipole inverse solutions are inherently robust to inaccuracies in forward solutions (i.e., scalp potentials), but dependent on the overlapping activity of other neural sources. Significantly smaller time and storage requirements are the principal advantages of the reciprocal approaches.

5.2.1 Skull Conductivity

In our numerical simulations, whether or not noise is present, inverse dipole solutions with the more realistic skull conductivity of 1/15 yield marginally lower position errors than with a conductivity of 1/80. Presumably, dipole position accuracy improves because the larger, less attenuated scalp potentials resulting from a higher skull conductivity of 1/15 penalize even smaller errors in source dipole position than with a conductivity of 1/80 (see Section 5.2.3). Overall, amplitude and orientation errors are minimally affected. For all four approaches, relative differences in scalp potential accuracy between the two skull conductivity values are not necessarily reflected in dipole position accuracy. Even though forward RDM values somewhat increase for the CC approach when skull conductivity is raised from 1/80 to 1/15, position errors for the corresponding inverse dipole solutions still improve with the same conductivity modification. Indeed, the previous considerations on, for example, the effects of interpolation and discretization on forward solutions in terms of skull conductivity (see Section 5.1.1) are no longer applicable with respect to inverse solutions. On the one hand, attenuated scalp potentials resulting from the lower skull conductivity of 1/80 renders them more susceptible to numerical errors. On the other hand, the larger potential gradients resulting from a higher skull conductivity of 1/15 increases the reliance of forward solution accuracy on interpolation and discretization. Inverse dipole positions, however, remain accurate with both skull conductivities and all approaches even for highly eccentric dipoles. Furthermore, the aforementioned relative invariance of reciprocal forward solutions to skull conductivity alterations does not translate to a greater invariance of inverse solution accuracy with reciprocal approaches than with conventional ones.

Our preliminary work (Finke et al., 2002) suggested that tangential dipole position errors with the RV approach are resistant to ±10% errors in skull conductivity. This is likely due to intrinsic properties of the reciprocal formulation combined with the particular discretization and interpolation used in the RV approach (see Section 5.1). This invariance to conductivity errors no longer holds true when ±25% errors in skull conductivity are considered or when noise is present. On the whole, large skull conductivity errors, with or without noise, affect dipole position error equally for all four approaches. The special case of the RV approach for tangential dipoles and ±10% changes in skull conductivity in the absence of noise is of limited practical value. The largest variation in position error with conductivity error is for eccentric radial dipoles and tangential dipoles of intermediate eccentricity. While skull conductivity errors generally increase position error in the above cases, the latter is actually improved for tangential dipoles of intermediate eccentricity with a conductivity error of -25%. It is encouraging to note that dipole position error variability remains limited (i.e., less than 5 mm) even for large skull conductivity errors (i.e., 1/15±25%) and two very different skull conductivity values. For the purposes of comparison, a skull conductivity of 1/80 corresponds to a conductivity of 1/15-81.25%.

Inverse solutions for the N_{20}-P_{20} SEPs are also calculated for a relative skull conductivity of 1/80 (0.33 S/m for the scalp, 0.0042 S/m for the skull, and 0.33 S/m for the brain/CSF volume conductor) and 1/15 (0.33 S/m for the scalp, 0.022 S/m for the skull, and 0.33 S/m for the brain/CSF volume conductor). Although converging inverse solutions still produce reasonably accurate dipole positions in most cases with a skull conductivity of 1/80, solutions with the more realistic, higher conductivity value of 1/15 yield smaller position errors overall. The maximum dipole position error is also approximately double at 29.2 mm with a skull conductivity of 1/80 versus 13.5 mm with a conductivity of 1/15. Even though the effects of conductivity on forward solution RDM values are variable for the different approaches, in general inverse solution minimum RDM values (i.e., the difference between measured potentials and those produced by inverse dipole solutions) are marginally higher with a skull conductivity of 1/80 than with a conductivity of 1/15. For a given stimulation study, dipole position errors of converging inverse solutions are similar overall for all approaches and scalp discretizations with both conductivity values. Again, as for simulated data on spherical models, the relative invariance of reciprocal approaches to conductivity changes in forward scalp potentials does not improve dipole position error for inverse solutions.

Our interest in the robustness of a given approach to errors in skull conductivity stems from the real world situation where accurate estimation of this conductivity is fraught with difficulties (see Chapter 1). The low conductivity of the skull in particular is known to be a major determinant of scalp potential accuracy (i.e., forward solutions) and therefore, potentially, of dipole solution accuracy (i.e. inverse solutions). While the relative skull conductivity value has long been accepted as 1/80 (Rush and Driscoll, 1968), subsequent work has since supported the use of the much larger value of 1/15 (Oostendorp et al., 2000). Regardless of the skull conductivity selected, assigning one identical value to the entire skull compartment in head models for all individuals neglects the skull conductivity's heterogeneity and anisotropy as well as any inter-subject variability. Furthermore, even if the best possible approximation is made considering the above limitations, there is still no guarantee that this value is indeed the best effective conductivity value for a given head model (see Introduction). Hence, an approach's stability in the face of all these inevitable sources of error is obviously of great interest. Although reciprocal forward solutions demonstrate a greater invariance in accuracy with skull conductivity alterations, reciprocal inverse solutions are not more robust to the same skull conductivity alterations or to skull conductivity errors especially when these are large or in the presence of noise. In fact, reassuringly, dipole position error for all approaches remains relatively stable in the face of this uncertainty in skull conductivity, most likely due to the nonlinear nature of the single-dipole inverse problem (see Section 5.2.3).

Another important issue surrounding simplex minimization of the RDM is that of reliable convergence to the correct solution. In our numerical simulations, over 80% of all simplex trials converge in less than 1000 iterations for all approaches and both conductivity values. Note that the presence of noise actually facilitates convergence both in terms of the total number of converging simplex trials and the number of iterations required for convergence (see Section 5.2.2). Position error tolerance is defined as the greatest improvement in dipole position error by a converging simplex trial with a non-minimum RDM solution when compared to the minimum RDM solution for a given approach, BEM discretization, etc., and is essentially a measure of how well RDM minimization yields the most accurate dipole position. For noiseless inverse solutions calculated with skull conductivity errors of ±25%, the maximum position error tolerance is 2.4 mm compared to 2 mm in the absence of skull conductivity errors. The presence of noise also increases the maximum position error tolerance to 5.2 mm. Thus, how well the minimum RDM solution yields the best possible dipole position depends on the extent of noise in the data and the accuracy of the skull conductivity used in the volume conductor head model.

For N_{20}-P_{20} SEP inverse solutions with a skull conductivity of 1/15, all simplex trials converge in much less than 1000 iterations and the vast majority of those trials converge around the global RDM minima and produce similar dipole positions for a given approach, BEM discretization, and stimulation study. With a skull conductivity of 1/80, simplex convergence becomes an issue for certain stimulation studies (i.e., simplex trials not converging to a minimum RDM value in less than 1000 iterations or converging to a wider range of inverse solutions including to local RDM minima with clearly distinct dipole positions). The maximum dipole position error tolerance is also significantly increased to 24.2 mm versus approximately 1 mm for a skull conductivity of 1/15. These results, as well as dipole position accuracy for measured potentials on realistic head models, support the use of the presumably more realistic skull conductivity of 1/15.

5.2.2 Numerical Considerations

For numerical simulations on spherical head models, the centroid and vertex approaches are compared for a similar number of unknowns but using different discretizations (see Section 5.1.2). Matching the number of unknowns solved for in forward solutions allows the use of almost twice as many discretization elements with the vertex approaches as with the centroid approaches (i.e., approximately 6,500 to 7,500 for the former and 4,500 elements for the latter). Interestingly, very little separates centroid and vertex approaches in terms of inverse solution accuracy and convergence for all dipoles, skull conductivity values and errors, and noise levels. However, comparing them in this manner does not allow us to distinguish between the effects of interpolation order and those related specifically to the level of discretization. When more realistic BEM head models are considered, then centroid and vertex approaches are compared for a similar number of discretization elements (i.e., approximately 7,500 to 10,000) and hence solve for a different number of unknowns. Once again there is little to choose between approaches in terms of dipole position error. Thus, whether comparing centroid and vertex approaches for a similar number of unknowns or a similar number of discretization elements, inverse solutions are comparable. Furthermore, position errors remain low even for highly eccentric dipoles that generate large errors in scalp potentials. This suggests that the level of discretization used in our work is sufficient to produce accurate dipole positions, even in the presence of noise and skull conductivity uncertainty.

Although the number of unknowns for which the reciprocal forward solutions solve is approximately twice as high as for their conventional counterparts (i.e., centroid and vertex approaches, respectively), no attempt is made at compensating for this difference when comparing conventional and reciprocal approaches. Generating multiple discretizations in an attempt at matching the number of unknowns for the different approaches is problematic, particularly when several individual, realistic BEM head models are considered. Conventional and reciprocal approaches are therefore compared for a similar number of discretization elements and hence solve for a different number of unknowns. So, for a fixed number of discretization elements, the approximate relationship between the number of unknowns for the different approaches is as follows:

RC ≈ 2 x RV ≈ 2 x CC ≈ 4 x CV (see Section 5.1.2). Again, the relative equivalency in dipole position errors that remain low for the different approaches, even with this discrepancy in the number of unknowns, suggests that the level of discretization used is adequate for the source and head models under consideration. Contrary to forward solutions for highly eccentric dipoles, increasing the overall number of discretization elements - either in general or to exploit a relatively smaller number of unknowns for a given approach - is not expected to further improve dipole position accuracy. Note that this does not necessarily hold true for dipole amplitude and orientation errors (see Section 5.2.3).

As previously discussed, computational time requirements for the generation of forward transfer matrices are principally determined by the number of unknowns for the different approaches and therefore also follow the approximate relationship: RC ≈ 2 x RV ≈ 2 x CC ≈ 4 x CV. However, once these matrices are generated and stored for a given BEM head model and approach, they can be repeatedly used to calculate scalp potentials with different source models, either for the forward problem or iteratively for the inverse problem. Fletcher et al. (1995) indicated that computation times for the reciprocal approach are linearly proportional to BEM head model size (i.e., number of discretization elements), while those of the conventional approach are proportional to its square. Furthermore, for a given BEM head model, only the potentials and normal fluxes on the innermost cortical surface for each electrode pair need to be stored for subsequent calculations with the reciprocal approach. In the conventional approach, storage requirements for forward transfer matrices are again proportional to the square of BEM head model size. Thus, for similar surface discretizations, scalp potential computation times and transfer matrix storage requirements for the different approaches are related as follows: CC > CV > RC > RV. Although generation of forward transfer matrices takes longer for reciprocal approaches than for conventional approaches, this is only performed once for a given volume conductor discretization. Subsequent scalp potential calculations require significantly less storage and time for reciprocal approaches and these are repeatedly performed for inverse solutions (e.g., for ten different simplex trials and an average of 100 iterations per trial with four scalp potential calculations per trial, this corresponds to 4,000 scalp potential calculations for one inverse solution).

Contrary to Fletcher et al. (1995), a two-step isolated-problem implementation (Hämäläinen and Sarvas, 1989) is used by us for conventional approaches with both skull conductivity values (see Chapter 1). This introduces an additional step in both forward transfer matrix generation and scalp potential calculations, as well as increasing storage requirements which now must include a second separate transfer matrix for the innermost cortical surface. The differences in scalp potential calculation times and storage requirements between conventional and reciprocal approaches are therefore increased even further, while the differences in transfer matrix generation times are decreased. When using our realistic BEM head models and excluding transfer matrix generation times, the net result is inverse solutions that take significantly less time for reciprocal approaches (i.e., less than approximately one third of the time required by the CV approach and 1/12th of the time required by the CC approach). As the number of simplex trials required is similar overall for the different approaches, this contrast in time requirements for inverse solutions is mostly due to the factors described above. Furthermore, storage requirements for transfer matrices are also significantly smaller for reciprocal approaches (i.e., less than approximately 1/25th of the memory required by the CV approach and 1/100th of the memory required by the CC approach). The current state of technology has rendered the question of memory and computational time requirements less critical even when using personal computers. However, the reduction in these parameters for the reciprocal approaches is substantial enough to facilitate their application to a larger number of studies, as well as their comparison for different source models, potential distributions, and time points.

In terms of forward solutions on spherical models, scalp potential accuracy is somewhat variable with the different orders of interpolation considered (see Section 5.1.2). Overall, higher order interpolation is mostly of interest when attempting to compensate for a level of discretization that is inadequate for a given potential and/or flux gradient. This becomes an issue especially when the potential gradients are high, namely for the innermost cortical surface, for highly eccentric radial dipoles, and for a higher skull conductivity of 1/15. For the number of discretization elements considered here, RDM values remain elevated for highly eccentric dipoles, especially if they are radial, regardless of the approach considered. Surprisingly, centroid (i.e., constant) and vertex (i.e, linear and quadratic) approaches result in similar inverse solutions in terms of both accuracy and convergence for all dipoles, skull conductivity values and errors, and noise levels. This is also the case for N_{20}-P_{20} SEP inverse solutions with both conductivity values. Even for highly eccentric radial dipoles on spherical models, dipole position errors are unexpectedly low (i.e., less than 5 mm without noise and less than 8 mm with 20% noise). This suggests that even the restrictive assumption of a constant potential and flux on each discretization element is sufficient to produce accurate inverse dipole positions for the source and head models used here. Relatively low position errors for all approaches, even for highly eccentric radial dipoles that produce large errors in forward scalp potentials (i.e., RDM > 100%), are again due to the nonlinear nature of the single-dipole inverse solution with respect to dipole position (see Section 5.2.3). Thus, further modifications to interpolation order, such as linear Galerkin (Mosher et al., 1999b) or second-order interpolation (Frijns et al., 2000), are unlikely to improve dipole position errors. However, increasing interpolation order may still improve inverse dipole amplitude and orientation, since these linearly determined parameters tend to reflect forward solution accuracy, including for highly eccentric dipoles.

Discretization Refinement

In our results for spherical head models, local discretization refinement of all three surfaces in the vicinity of the scalp electrodes is used for all four approaches. The reciprocal approaches transfer source currents from unknown dipole positions to known electrode sites. It has been suggested that selective discretization refinement around these electrodes improves scalp potential accuracy when the overall BEM discretization and interpolation is otherwise inadequate to model certain potential and/or flux gradients (e.g., for highly eccentric dipoles). Contrary to previous findings (Fletcher et al., 1995; Finke, 1998), no clear improvement is found for the reciprocal approaches for highly eccentric dipoles in terms of forward solution accuracy, except when comparing accuracy between reciprocal approaches (RC and RV). As previously mentioned, all approaches result in similar inverse solutions for both skull conductivity values and in the presence of skull conductivity errors and noise, even for highly eccentric dipoles for which position errors remain low. Once again, this is also the case for N_{20}-P_{20} SEP inverse solutions with both conductivity values. In fact, when comparing the RC approach with different local discretization strategies including no selective electrode refinement at all, or comparing the RC approach with its constant potential and flux assumption and the RV approach with quadratic interpolation at the electrode sites, N_{20}-P_{20} SEP dipole position errors are relatively unaffected. This is particularly surprising considering that electrode sites are used for current injection and withdrawal with the reciprocal approaches and large potential gradients are generated around these sites. Even though reciprocal approaches show some degree of relative invariance to skull conductivity alterations in forward solutions (see Section 5.2.1) and selective electrode refinement may be a factor, this again does not translate to improved dipole position stability or error in inverse solutions.

Note that, although selective electrode refinement is usually performed on all three surfaces (Fletcher et al., 1995; Finke, 1998), only scalp discretizations are modified in this manner for our realistic BEM head models. However, considering that neither refinement around electrode sites on the scalp surface nor higher-order potential interpolation at these sites improve dipole position error because of its inherent robustness (see Section 5.2.3), it is likely that additional selective refinement of the skull and brain/CSF surfaces would also yield limited returns. Our results for N_{20}-P_{20} SEPs even suggest that selective discretization refinement in the vicinity of scalp electrodes may not be necessary at all for the use of the reciprocal approach. Although scalp discretization refinement marginally improves minimum RDM values, this does not generally translate to decreases in dipole position errors, whether considering the RC approach or the conventional approaches. Because of the difficulty in calculating the current distribution following injection at a triangle vertex, the RV approach is only used with selective electrode refinement. The surface normal and hence the flux are not strictly defined at triangle vertices and, thus, injecting and withdrawing current at these sites may introduce further inaccuracies in a critical area for the reciprocal approach. Smaller planar triangles with an additional curvilinear quadrilateral are therefore inserted at each electrode site, and the flux at the sites of current injection and withdrawal is then calculated using quadratic interpolation on those quadrilaterals. Since the implementation of the RV approach seems to mandate some type of discretization modification around each electrode site, which represents an additional step in BEM head model generation, the centroid version of the reciprocal approach (i.e., RC approach) appears preferable as it can be accurately implemented on unmodified scalp discretizations. However, it may also be possible to implement the RV approach without selective electrode refinement and still produce reasonable forward solutions (Finke, 1998). Whereas the RC approach defines the flux as ±1 over the triangle area for current withdrawal and injection sites, the same flux for the RV approach can be approximated as ±1 over one third of the sum of all triangle areas adjacent to the electrode site. The impact of this unmodified scalp discretization implementation of the RV approach in terms of inverse solutions remains to be seen. The RV approach aside (see Section 5.3), our unrefined BEM discretizations are indeed adequate for single-dipole N_{20}-P_{20} SEP inverse solutions whether a constant or linear potential is assumed (i.e., for the CC, CV, and RC approaches).

Other Factors

Scalp potentials are simulated on our spherical models assuming no noise and then perturbed by the addition of 10% or 20% white Gaussian noise (corresponding to a signal-to-noise ratio of 20 db and 13.98 db, respectively). These noise levels are selected as being representative of the noise expected during actual EEG measurements (e.g., for single epileptic spikes, the noise level typically equals 20%, but for averaged spikes, it typically equals 10%). Adding 20% noise to the simulated potentials increases dipole position error but this increase is limited (i.e., position errors remain below 15 mm) and the least pronounced for highly eccentric dipoles (i.e., position errors remain below 8 mm). The minimal effect of noise on position error for highly eccentric versus less eccentric dipoles is attributable to the relative increase in signal-to-noise ratio (SNR) as the dipole approaches the BEM surfaces including the electrode sites on the scalp. Results with 10% noise fall between those without noise and those with 20% noise. Accurate dipole positions for our spherical models even in the presence of noise is promising for eventual inverse solutions on real EEG data, and this indeed proves to be the case for averaged N_{20}-P_{20} SEPs where dipole position errors are also low with a skull conductivity of 1/15 (i.e., less than 14 mm). These results are particularly encouraging, considering that N_{20}-P_{20} SEP sources are typically tangential dipoles of intermediate eccentricity (i.e., approximately 65-70%), which correspond to the largest position errors for simulated potentials in the presence of noise on our spherical models. As previously mentioned (see Section 5.2.1), although tangential dipole position errors with the RV approach are invariant to ±10% errors in skull conductivity (Finke et al., 2002), this no longer holds true in the presence of noise.

Simplex solutions also converge more consistently (i.e., in less than 1000 iterations), and with fewer iterations (i.e., approximately half), in the presence of noise than when noise is absent from potential simulations on spherical models. The reason for this is that noise tends to smooth the valleys of the four-dimensional hyperspace formed by the RDM and the three trial-dipole position coordinates. The presence of noise essentially raises the valley floor resulting in much more gradual valley slopes. A simplex trial will only converge when the RDM difference between successive iterations is less than 0.0001, which can only occur if the valley floor is reached. In the absence of noise, because of the narrow valley and steep sides, this convergence can be very slow. On the other hand, once noise is present, the wider valley floor and shallower slopes result in easier and faster simplex convergence. Musha and Okamoto (1999) noted these changes with noise but not their effect on simplex minimization. Not surprisingly then, for measured N_{20}-P_{20} SEPs on realistic head models with a skull conductivity of 1/15, all ten simplex trials for each inverse solution converge to a minimum RDM value in much less than 1000 iterations, and the vast majority of trials converge around the global RDM minima and produce similar dipole solutions. Among simplex trials converging around the global RDM minima, the maximum RDM value difference is 0.1%, the maximum dipole position difference is 2 mm, the maximum dipole orientation difference is 1°, and the maximum dipole amplitude difference is 0.1 $\mu A/mm^2$. In passing, with the presumably less realistic skull conductivity of 1/80, simplex convergence becomes an issue for certain stimulation studies (see Section 5.2.1). Note that convergence profiles are similar for all approaches for simulated data, with or without noise and skull conductivity errors, and for real data with both conductivity values. An alternative to the simplex algorithm that makes use of the gradient in the RDM profile to achieve faster convergence, such as Levenberg-Marquardt (Marquardt, 1963), is mostly of interest for the noiseless case where convergence may be an issue and the valley is narrow with steep sides. However, in our numerical simulations including those without noise, over 80% of all simplex trials still converge in less than 1000 iterations.

The downside of this broad valley floor in the presence of noise is the existence of multiple local minima that result in different simplex trials converging to slightly different dipole positions on either side of the correct dipole. This results in a minimum RDM solution that does not always yield the minimum position error. We define position error tolerance as the greatest improvement in dipole position error by a converging simplex trial with a non-minimum RDM solution (i.e., local minimum) when compared to the minimum RDM solution (i.e., global minimum). This tolerance represents the maximum uncertainty in the simplex solution and is essentially a measure of how well RDM minimization yields the most accurate dipole position. In our numerical simulations on spherical models without noise contamination or skull conductivity errors, no converging simplex trial yields a solution with a position error that improves on the minimum RDM solution by more than 2 mm (i.e., the maximum position error tolerance is 2 mm). The presence of noise increases the maximum position error tolerance to 5.2 mm. For noiseless inverse solutions calculated with relative skull conductivity errors of ±25%, the maximum position error tolerance also increases to 2.4 mm (see Section 5.2.1). Thus, how well the minimum RDM solution yields the best possible dipole position depends on the extent of noise in the data and the accuracy of the skull conductivity value used in the volume conductor head model. For N_{20}-P_{20} SEP inverse solutions, position error tolerances are lower than expected at approximately 1 mm or less. However, with the less realistic skull conductivity of 1/80, the maximum position error tolerance significantly increases to 24.2 mm. Essentially, the minimum RDM criterion used to pick the inverse dipole solution amongst converging simplex trials is correct to within a small position error tolerance that is largely determined by measurement noise and inaccuracies in the volume conductor model, including skull conductivity error, which are mostly unavoidable. As such, position error tolerance is more closely related to forward solution inaccuracies than dipole position error itself, but still remains reasonable even with high minimum RDM values. In general, all four approaches produce similar position error tolerances for a given discretization and potential distribution.

For a given scalp discretization in our realistic head models, the projected electrode sites do not exactly correspond to the modeled electrode sites for certain approaches. This difference between projected electrode sites and modeled electrode sites is referred to as the electrode localization error. Since our BEM surfaces are discretized by matching projected electrode sites on the scalp with triangle vertices, electrode localization errors for the CV approach are typically zero while those for the CC and RC approaches are not. However, scalp discretizations with selective electrode refinement are generated in which the difference between projected electrode sites and triangle centroids are minimized and, hence, electrode localization errors for the CV approach are nonzero in this case. Scalp discretizations with selective electrode refinement are also generated in which the projected electrode sites correspond to triangle vertices or quadrilateral centers. Note that electrode localization errors for unmodified discretizations tend to be larger than those for scalp discretizations with selective electrode refinement (i.e., approximately 5 mm versus 1.5 mm or less on average) since the triangles around the electrode sites are smaller in the latter case. N_{20}-P_{20} SEP inverse solutions are therefore calculated on at least one scalp discretization that minimizes electrode localization errors for each approach. However, although minimum RDM values marginally increase with larger electrode localization errors, this does not generally translate to increases in dipole position errors for any of the four approaches. One practical advantage of the vertex approaches is that electrode sites are more easily made to correspond to triangle vertices than to triangle centroids. Interpolating measured potentials from projected electrode sites to modeled electrode sites on the scalp is possible, but considering the negligible impact of electrode localization errors on inverse solutions, this is unlikely to affect our results and is not attempted here. To record the small fields of the early SEPs, an inter-electrode distance of less than 3 cm is required for accurate spatial sampling (Gevins et al., 1990; Spitzer et al., 1989). SEPs are recorded from 128 scalp electrodes against a common reference electrode Cz at the apex of the head which corresponds to an inter-electrode distance is approximately 2 cm (Gevins and Bressler, 1988). Although only 42 electrode sites, regularly distributed at the intersections of lines of latitude and longitude, are considered for our spherical models, the relative dipole position accuracy is similar for both the simulated and real data (i.e., less than 1.5 mm and 1.4 mm, respectively).

The time point corresponding to the largest instantaneous global activity (i.e., 22 ms post-stimulation), defined on the basis of a peak in the global field power (GFP) (Lehmann, 1987), is selected for source analysis in the interval of interest for our N_{20}-P_{20} SEPs. The GFP is an assessment of the spatial variation of the potentials measured on the scalp at each point in time and therefore essentially reflects the degree of dispersion in a given potential distribution. Since the GFP takes only differences between measured potentials into account, it is independent of the reference electrode used and is therefore a reference-independent measure of the evoked potential activity. The accuracy of inverse solutions is dependent on the exact time point analyzed. Selecting time points based on GFP peaks is not possible in all of our stimulation studies and in some cases different time points produce smaller dipole position errors. In fact, those stimulation studies that produce the largest dipole position errors are those that do not have a distinct GFP peak. This most likely reflects the presence of significant overlapping electrical activity from non N_{20}-P_{20} SEP related neural sources at the time points analyzed such as the earlier subcortical SEPs (see Section 5.2.3). Even with these limitations, GFP peaks are typically used in the identification of time points for source analysis (Buchner et al., 1995b).

It is generally accepted that most of the energy of the early SEPs is contained in the 20-250 Hz frequency band (Lüders et al., 1986). Further digital filtering is required in order to reduce the overlap of low frequency EEG components that, if not filtered, can lead to substantial source localization error. In general, a zero-phase shift type filter is used because this results in minimal phase distortion of the EEG data and better suppression of frequencies outside the selected frequency band. However, according to Scherg et al. (1999), a forward type filter should be used to analyze the early, weak N_{20}-P_{20} SEP activity. The concern is that because a zero-phase shift low cutoff filter has symmetric sidelobes in time, the stronger later SEP activity around 24-35 ms may be projected into the earlier phase of 13-22 ms. Therefore, inverse dipole solutions are not only calculated on EEG data filtered with the zero-phase shift type (i.e., 20 Hz high-pass), but also on data filtered with the forward type (Buchner et al., 1995b). However, this attempt at separating the N_{20}-P_{20} SEP from other neural sources with overlapping electrical activity did not reliably lead to more accurate inverse solutions. As with zero-phase shift filtering, forward filtering does not produce a GFP peak during the interval of interest for every stimulation study. Furthermore, even for those studies in which a peak is identified, dipole position errors as well as minimum RDM values are larger overall with forward filtering than with zero-phase shift filtering. Certain inverse solutions are even located in areas of the brain clearly not related to N_{20}-P_{20} SEP activity. Further attempts at identifying optimal filtering strategies either in terms of GFP peaks or inverse solution accuracy are beyond the scope of this thesis.

5.2.3 Source Dipole Accuracy

Dipole Position

In numerical simulations on spherical head models, dipole position errors are small and only minimally increase for highly eccentric dipoles in the absence of noise (i.e., position errors remain below 5 mm). Adding noise to the simulated potentials increases position error but the impact is still limited (i.e., position errors remain below 15 mm). Results are similar for radial and tangential dipoles except at intermediate eccentricities where tangential dipoles produce marginally larger position errors. So, in the presence of noise, while radial dipoles exhibit a maximum error for centric dipoles, tangential dipoles exhibit a maximum error for dipoles of intermediate eccentricity. Position errors for highly eccentric dipoles are the least affected by noise and remain below 8 mm for both radial and tangential dipoles. Dipole amplitude and orientation errors, however, do tend to increase at high eccentricities, in some cases dramatically. As previously mentioned (see Section 5.2.1), increasing the skull conductivity from 1/80 to 1/15 slightly improves position error for all dipoles. The largest variation in position error with skull conductivity error is for eccentric radial dipoles and tangential dipoles of intermediate eccentricity, but again this variability is limited (i.e., less than 5 mm).

For each median nerve stimulation study, potential distributions generated by N_{20}-P_{20} SEP inverse solutions are consistent with eccentric tangential dipoles measured over the contralateral parietal area as expected based on the literature (Hari et al., 1984; Kaukoranta et al., 1986; Hari, 1991; Suk et al., 1991; Gallen et al., 1993; Hari et al., 1993; Yang et al., 1993; Kristeva-Feige et al., 1994; Kristeva-Feige et al., 1995; Nakamura et al., 1998; Henderson et al., 1975; Buchner et al., 1995a; Kristeva-Feige et al., 1997), and concur with the corresponding measured distributions. With a skull conductivity of 1/15, dipole position errors are small when compared to the nearest point of the primary sensory hand area identified on MRI (i.e., less than 14 mm and around 5 mm on average). The accuracy of inverse dipole solutions based on scalp potentials has been reported to be in order of 1 cm in general (Cuffin et al., 1991) and for N_{20}-P_{20} SEPs in particular (Buchner et al., 1994a; Buchner et al., 1995a; Gross et al., 2000). Overall, position error is equally distributed in the axial, sagittal, and coronal planes. Inverse solutions tend to be located in the postcentral gyrus within or posterior to the primary sensory hand area, except for one stimulation study that produces dipoles in the precentral gyrus. Once again, inverse solutions with the more recent, higher skull conductivity of 1/15 generally yield smaller position errors than with a conductivity of 1/80, and the maximum dipole position error is also approximately double with the latter skull conductivity.

The N_{20}-P_{20} SEP inverse solutions are also comparable to those found for simulated potentials on spherical models with similar sources, where a position error of approximately 1 cm is produced for tangential dipoles of intermediate eccentricity in the presence of noise. Still, although the N_{20}-P_{20} SEP position errors range for 0 to 14 mm, they average around 5 mm, which is somewhat lower than expected based on inverse solutions for simulated potentials. However, these latter results are with 20% noise, which typically corresponds to non-averaged EEG data. For averaged EEG data, a fairer comparison would be with simulated potentials in the presence of 10% noise (not shown), for which results fall between those without noise and those with 20% noise. N_{20}-P_{20} SEP position error calculations are also fundamentally limited by their reliance on anatomical landmarks identified on MRI (see Section 5.3). Whereas dipole positions are compared to points in simulations, they are compared to volumes (i.e., 750 voxels or mm^3 on average) with our real data. Furthermore, the true relationship between functional and anatomical localization is unclear and some degree of inter-subject and inter-observer variability is to be expected (Sobel et al., 1993; Kennedy et al., 1998). Note that there are no obvious landmarks to delimit the vertical extent of Brodmann area 3b in the posterior bank of the central sulcus. The postcentral gyrus at the apex of the central sulcus may in part correspond to Brodmann area 1 and the nadir to Brodmann area 3a. Including its full vertical extent in the primary sensory hand area potentially underestimates position error for certain stimulation studies.

The relative-difference measure (RDM), which compares calculated and measured or simulated potentials numerically, is often used as an indirect indicator of inverse solution accuracy. As previously mentioned (see Section 5.1), forward solution RDM values are variable for different approaches, discretizations, and skull conductivity values, and substantially increase for highly eccentric dipoles, especially radial dipoles (i.e., > 100%), reflecting large differences between calculated and simulated potentials in these cases. Inverse solution RDM values, namely the difference between simulated or measured potentials and those produced by inverse dipole solutions, represent the minimum RDM solutions as determined by simplex minimization and are presumed to correspond to the most accurate dipole positions possible. In potential simulations, inverse solution minimum RDM values are therefore always equal to or less than forward solution RDM values and, while dipole positions are exact for forward solutions, dipole position errors corresponding to inverse RDM solutions are typically non-zero. For N_{20}-P_{20} SEPs, inverse solutions, minimum RDM values are still high overall, ranging from 12% to 60%, again indicating quite large numerical differences between measured and calculated potentials. As with forward solution RDM values, small variations in inverse RDM values are also noted for different approaches, discretizations, and skull conductivity values. When discussing scalp potential accuracy, there is often an implicit assumption that lower forward solution RDM values will not only lead to lower inverse RDM values but also to smaller dipole position errors.

This assumption, however, does not appear to hold true in our results. When considering simulated potentials on spherical head models in the absence of noise, although forward solution RDM values are elevated for highly eccentric dipoles, especially for radial dipoles (i.e., > 100%), still reasonably accurate inverse dipole positions are obtained in these cases (i.e., position errors are below 5 mm). Even in the presence of 20% noise, position errors remain below 8 mm for highly eccentric dipoles and, in fact, are smaller in these cases than for less eccentric dipoles that correspond to lower forward solution RDM values. Furthermore, the relative scalp potential accuracy of the different approaches as depicted by forward solution RDM values is not reflected in inverse dipole position errors that remain comparable for these approaches. Similarly, increasing skull conductivity from 1/80 to 1/15 has variable effects on forward solution RDM values for the different approaches, but this increase tends to improve dipole position errors regardless of the approach considered. Thus, even the aforementioned relative invariance of reciprocal forward solution accuracy to skull conductivity changes does not translate to a greater invariance of inverse dipole position accuracy with the same skull conductivity alterations or with skull conductivity errors in most cases.

For N_{20}-P_{20} SEP inverse solutions, dipole position errors remain small (i.e., below 14 mm) even when associated with high minimum RDM values (i.e., above 50%). The observed marginal improvement in minimum RDM values due to scalp discretization refinement and lower electrode localization error does not generally translate to decreased dipole position errors. Even if the general trend is for higher minimum RDM values to produce larger position errors, stimulation studies that produce the lowest RDM values do not necessarily produce the smallest position errors and vice versa. Although reciprocal approaches generate inverse solutions with the lowest minimum RDMs, the conventional approaches result in the smallest dipole position errors overall, even though this difference is minimal. Some correspondence is found with skull conductivity alterations, as both inverse solution minimum RDM values and dipole position errors slightly improve when increasing skull conductivity from 1/80 to 1/15. However, as with simulated potentials where reciprocal approaches show some degree of relative invariance to conductivity alterations in forward potential accuracy, this does not translate to decreased dipole position error for inverse solutions. Essentially forward solution RDM values, as well as inverse solution minimum RDM values in most cases, are poor predictors of single dipole position accuracy.

Numerical differences between calculated and simulated or measured scalp potentials, reflected by high RDM values, are mostly irrelevant due to the apparent robustness of inverse dipole position to inaccuracies in forward solutions. A single RDM value essentially gives a snap shot view of the accuracy of scalp potentials produced by a particular dipole. It does not, however, communicate any information concerning RDM values for dipoles even a short distance away. For example, even if forward solution RDM values are high when the true dipole is considered, a different dipole may still produce much lower RDM values. When the minimum RDM value corresponds to a dipole solution only a short distance away from the true dipole position, then this results in a small dipole position error even if the forward solution RDM value is elevated. Furthermore, even if the minimum RDM value as determined by simplex minimization is elevated, this may still correspond to an inverse dipole solution near the true dipole position. Basically, what matters is not the RDM value per say, but rather that the minimum RDM solution corresponds to an inverse dipole position that is reasonably accurate. The existence of a minimum RDM value for a particular inverse dipole solution near the true dipole position is not predicted by either the value of that minimum RDM solution or the forward solution RDM value when the true dipole is known. The lack of correlation between scalp potential accuracy and dipole position accuracy is due to the nonlinear nature of the single-dipole inverse problem. A secondary factor contributing to position errors is the presence of a positional constraint limiting dipoles to within the brain/CSF volume conductor, but this constraint is only actively involved in inverse solutions for certain highly eccentric tangential dipoles in simulations. Although a single RDM value does not necessarily predict dipole position accuracy, the RDM still remains an appropriate choice for simplex minimization. The minimum RDM criterion used to determine inverse solutions produces accurate dipole positions reliably to within a low position error tolerance (see Section 5.2.2). Furthermore, the use of the RDM limits the magnitude range of the function to be minimized, allowing the selection of a fixed stopping point for the simplex algorithm that is independent of the source dipole under consideration.

Dipole Moment

While simplex minimization of the RDM is used to select the best possible inverse dipole position, the best dipole moment for a given trial dipole position is calculated directly by the so-called normal equations (Forsythe and Moler, 1967). So, contrary to the nonlinearly determined inverse dipole positions, the linearly determined inverse dipole moments are affected by inaccuracies in calculated scalp potentials. In simulations on spherical head models, inverse solution amplitude and orientation errors tend to increase, in some cases dramatically, for highly eccentric dipoles that produce large RDM values, while the impact on position error is less pronounced. To further illustrate this difference in behavior between inverse dipole position and moment, consider the particular case of a highly eccentric radial dipole. This type of source produces a large, relatively localized peak in the potential distribution on the scalp directly above the dipole that involves relatively few electrode sites. The forward solution RDM is very elevated in this case (i.e., > 100%), since numerical inaccuracies are compounded by the large potential gradients generated by a radial dipole near the BEM surface (see Section 5.1). As the source dipole is exact in forward solutions, it is unlikely that the calculated potential peak is significantly displaced on the scalp surface, or that the shape of this potential distribution is grossly distorted. Substantial errors in the size of calculated potential distributions are, however, produced by these numerical inaccuracies in forward solutions, errors that can be compensated for by mostly modifying dipole amplitude. Furthermore, as the dipole is close to the surface and scalp potentials are only sampled at discrete electrode sites that may not exactly correspond to the potential peak, even small relative differences in calculated potentials at neighboring electrode sites near the dipole may cause significant changes in orientation. In fact, if the true dipole position is maintained, and the normal equations are used to calculate the best dipole moment for that position, then the resulting moment will potentially be quite different then the true dipole moment. The dipole amplitude and orientation will essentially adjust to produce a best possible fit approximation of the potential distribution for that dipole position. This will result in a much lower RDM value than for the true dipole forward solution without modifying dipole position at all, even if some discrepancy in potentials still remains. Large changes in dipole position that would either displace the potential peaks on the scalp surface if they are in the tangential direction, or either flatten or sharpen the potential distributions if they are in the radial direction, are unlikely to produce potentials that are more accurate. However, slight adjustments to the dipole position, and hence the resulting dipole moment, allow even further reduction in the differences between calculated and simulated or measured potential distributions until a minimum RDM inverse solution is reached that produces a relatively small position error.

Conventional and reciprocal approaches, including centroid and vertex implementations, have similar inverse solution characteristics. In numerical simulations, there is little to choose between the CC, CV, RC, and RV approaches in terms of dipole position and moment. For N_{20}-P_{20} SEPs, calculated potential distributions for the four approaches are nearly identical in appearance for a given stimulation study, and the greatest difference in minimum RDM values between approaches is only 2.6%. To further illustrate the similarities between inverse solutions for a given stimulation study, average dipole position, orientation, and amplitude differences between the various approaches are small (i.e., 1.5 mm, 0.9º, and 0.1 $\mu A/mm^2$, respectively). The maximum difference in dipole position is 5.1 mm, the maximum dipole orientation difference is 3.3º, and the maximum difference in dipole amplitude is 0.5 $\mu A/mm^2$. Note that also included in these above differences are various scalp discretizations, with or without selective refinement around electrode sites, and still inverse solutions for the conventional and reciprocal approaches remain comparable. Even though reciprocal approaches demonstrate some degree of relative invariance in forward solution accuracy to skull conductivity alterations, this does not translate to increased position error stability with the same alterations. Nor does it lead to improved dipole positions with skull conductivity errors, especially in the presence of noise, or real EEG data. In fact, inverse solutions produce accurate dipole positions in the face of skull conductivity uncertainty, whether conventional or reciprocal approaches are used. Quite simply, the nonlinear nature of the single-dipole inverse solution nullifies any beneficial effect of the invariance of the reciprocal approach to skull conductivity, just as it did the deleterious effect of inaccuracies in forward solutions for highly eccentric dipoles. Although the validity of position error calculations based on anatomical landmarks identified on MRI may be questioned (see Section 5.3), this is unlikely to modify our overall conclusions considering the small relative differences between approaches. Convergence profiles, as well as position error tolerance, are also nearly identical for both simulated and real data. Clearly, not much separates the different approaches in terms of inverse solutions. However, only a limited number of data sets are studied here.

As mentioned above, the nonlinear nature of the single-dipole inverse solution results in dipole position that is relatively insensitive to forward solution inaccuracies, represented by high RDM values, which are mainly reflected in the linearly determined dipole orientation and amplitude. Therefore, modifications specifically aimed at decreasing these RDM values, such as discretization refinement, higher order interpolation, or decreased electrode localization errors, do not improve dipole position errors. However, increasing the number of discretization elements, either overall or exclusively around electrode sites, or increasing the interpolation order on those elements may still improve dipole amplitude and orientation errors. Also, if linear solutions consisting of cortical surface potentials or the amplitudes of a fixed layer of cortical dipoles are of interest, then more accurate forward solutions should still improve these types of inverse solutions. Thus, potential advantages of the reciprocal approaches, such as the transfer of source currents from unknown dipole positions to known electrode sites that can be selectively refined in order to improve scalp potentials, or the relative invariance of forward solution accuracy to skull conductivity alterations, may still prove to be of value in these cases. Note that a minimum level of precision in volume conductor discretizations is still necessary for dipole position not to be adversely affected (Buchner et al., 1995b). Determining the lower limits of discretization required for accurate inverse solutions is not the focus of this thesis and no further attempts at varying the number of discretization elements are made here.

Other Factors

There are, however, other factors that do influence dipole position accuracy. The stronger the potentials on the scalp, whether or not these lead to more accurate forward solutions, the more inverse dipole position is restricted. In other words, the distance a trial dipole can be displaced from its true position without causing increased scalp potential errors and, therefore, increased RDM values, is more limited. Thus, inverse solutions with a skull conductivity of 1/15 in simulations yield marginally lower position errors than with a skull conductivity of 1/80, since the higher skull conductivity produces larger, less attenuated scalp potentials. Similarly, the minimal effect of noise on position error for highly eccentric dipoles when compared to less eccentric dipoles is attributable to the relative increase in SNR as the dipole approaches the electrode sites on the scalp. Note, again, that increasing dipole eccentricity has the exact opposite effect on forward solution RDM values.

The accuracy of inverse solutions is also dependent on the exact time point analyzed, and selecting time points based on GFP peaks is not always possible (see

Section 5.2.2). Stimulation studies that produce the largest dipole position errors are those that do not have a distinct GFP peak, which likely reflects the presence of significant overlapping electrical activity from non N_{20}-P_{20} SEP related sources (Valeriani et al., 2001). An attempt at separating the N_{20}-P_{20} SEP from these other neural sources using forward filtering did not reliably lead to more accurate inverse solutions. This underlines the fundamental limitation of the single dipole, single time point source model in reproducing realistic EEG data. It suggests that including more than one time point in the analysis, such as in spatio-temporal dipole solutions, or including more than one source model, such as in multiple-dipole solutions, may improve dipole position further at the cost of increased solution parameter space. However, this is still contingent on analyzing the appropriate time points and modeling the appropriate number and type of sources. To this end multiple signal classification (MUSIC) (Mosher et al., 1992; Kobayashi et al., 2002a; Kobayashi et al., 2002b; Chang et al., 2005) and independent component analysis (ICA) (Kobayashi et al., 2001; Kobayashi et al., 2002a; Kobayashi et al., 2002b; Richards, 2004) are also options. Although analysis is only performed here for a single dipole at a single time point, both reciprocal and conventional approaches are applicable to these alternative formulations and the robustness of dipole position error may still hold true in these cases although this remains to be validated.

5.3 Future Work

Modifications to both the conventional and reciprocal approaches that may further reduce computational requirements are possible. For the conventional approaches, potentials can be calculated exclusively at electrode sites on the scalp surface with an additional step in the generation of forward transfer matrices (Fletcher et al., 1995). This modification not only reduces storage requirements, but also renders computational times linearly proportional to the number of discretization elements in the head model, which is similar to the reciprocal approaches, as opposed to its square. However, the utilization of this accelerated conventional approach seems to preclude the use of the isolated-problem implementation (see Section 5.1.3). For the reciprocal approach, an expression exists for the electric field, and hence the lead field, defined as a function of source dipole location (see Chapter 2). It is therefore possible to also derive expressions for the derivatives of scalp potentials with respect to this location (Fletcher at al., 1995). Alternative minimization techniques that exploit the gradient in the RDM profile via these derivatives, such as Levenberg-Marquardt (Marquardt, 1963), can thus be used to possibly achieve faster convergence than with the simplex algorithm that searches for a minimum RDM without this information. Note, however, that the speed of convergence is not a major issue in our results and, as such, these alternatives are mostly of interest for noiseless simulated potentials where the narrow valley floor and steep sides of the RDM function to be minimized may affect convergence times (see Section 5.2.2). But even in this case, the vast majority of simplex trials converge in a reasonable number of iterations. Note that these variants are not typically used in BEM-based dipole source localization and their exact impact on relative computational requirements for the conventional and reciprocal approaches remains to be established.

Single-dipole inverse solutions for N_{20}-P_{20} SEPs suggest that selective discretization refinement in the vicinity of scalp electrodes may not be necessary at all for the use of the reciprocal approach (see Section 5.2.2). This is particularly surprising considering that electrode sites are used for current injection and withdrawal with the reciprocal approaches and large potential gradients are generated around these sites. However, only the RC approach is attempted without selective electrode refinement because of the difficulty in calculating the current distribution following injection at a triangle vertex with the RV approach. As previously mentioned, it may also be possible to implement the RV approach without selective electrode refinement and still produce reasonable forward solutions (Finke, 1998). Since modifications of the discretization around electrode sites represents an additional step in BEM head model generation, the use of unmodified scalp discretizations is always preferable as long as inverse solution accuracy remains unaffected. Although this remains to be verified for the RV approach, it would support its use over the RC approach considering that generation times and storage requirements for forward transfer matrices are approximately halved for the RV approach when compared to the RC approach. Inverse solution calculation times are similar for both the RC and RV approaches. Obviously, using the RV approach without discretization refinement would only increase its computational advantages over the conventional approaches even further.

The low conductivity of the skull mandates the use of a two-step isolated-problem implementation for accurate scalp potential calculations with the conventional approaches (see Section 5.1.3). While increasing the skull conductivity from 1/80 to 1/15 renders the use of the isolated-problem implementation less critical, forward solution RDM values are still significantly higher when the isolated-problem implementation is not utilized, especially for eccentric dipoles. However, considering the relative insensitivity of inverse dipole position to inaccuracies in forward solutions in our results, it is far from certain that these increased RDM values in the absence of the isolated-problem implementation would translate to increased dipole position error. This question is particular relevant with the presumably more realistic, higher skull conductivity of 1/15. Not having to use the isolated-problem implementation would eliminate a step in both forward transfer matrix generation and scalp potential calculations, as well as decreasing storage requirements since a second, separate transfer matrix for the innermost cortical surface now no longer has to be stored. Furthermore, the use of the accelerated conventional approach would now also be possible (see above). These changes would certainly reduce the differences in computational times and storage requirements between conventional and reciprocal approaches. Note also that if a fourth surface is to be added to the BEM head model, for example CSF between the brain and the skull, then both the CC and CV approaches can still be used instead of just the CC approach if the isolated-problem approach is required (Finke, 1998; Akalin-Acar and Gençer, 2004; Gençer and Akalin-Acar, 2005).

Although the reciprocal approaches do not produce more accurate dipole positions than the conventional approaches because of the nonlinear nature of these inverse solutions, they may still lead to increased precision in linearly determined inverse parameters. Indeed, dipole amplitude and orientation, cortical potentials or the amplitudes of a fixed layer of cortical dipoles, all may benefit from a reciprocal formulation that transfers source currents from unknown dipole positions to known electrode sites that can be selectively refined, or from the relative invariance of reciprocal forward solution accuracy to skull conductivity alterations. Furthermore, modifications specifically aimed at improving scalp potential accuracy, and hence decreasing forward solution RDM values, such as discretization refinement, higher order interpolation, or decreased electrode localization errors, may also improve this type of inverse solutions. Additional work in this area is required but obviously the possibility of exploiting reciprocal approaches beyond their computational advantages is of great interest. Note, however, that even if reciprocal approaches are unable to improve inverse solution accuracy in these cases, they still offer significantly reduced computational time and storage requirements.

As previously mentioned (see Section 5.2.3), the accuracy of inverse solutions is dependent on the exact time point analyzed and selecting the optimal time point for a particular source, whether based on GFP peaks or otherwise, is not always possible. Including additional time points in the source analysis as with spatio-temporal dipole solutions may therefore further improve inverse dipole positions at the cost of increased solution parameter space and computation times. Dipole position accuracy in inverse solutions is also affected by the presence of overlapping electrical activity from unmodeled neural sources. One approach to separating the activity originating from various sources underlying EEG data involves using filtering strategies. Including more than one source model as with multiple-dipole inverse solutions may improve dipole positions as well, but again involves additional dipole parameters and longer computation times. However, increased inverse solution accuracy is contingent on analyzing the appropriate time points or intervals and modeling the appropriate number and type of sources. To this end multiple signal classification (MUSIC) (Mosher et al., 1992; Kobayashi et al., 2002a; Kobayashi et al., 2002b; Chang et al., 2005) and independent component analysis (ICA) (Kobayashi et al., 2001; Kobayashi et al., 2002a; Kobayashi et al., 2002b; Richards, 2004) are also options. Both reciprocal and conventional approaches are applicable to these alternative formulations and the robustness of dipole position error may still hold true in these cases although this remains to be validated. Smaller time and storage requirements with similar inverse solution accuracy make reciprocal approaches the ideal choice for these more computational expensive strategies. Furthermore, the optimal source analysis strategy for a given application is not known a priori and a trial-and-error approach using various strategies is usually required. This again favors the faster reciprocal approaches.

Finally, dipole position error calculations are fundamentally limited by their reliance on anatomical landmarks identified on MRI. Essentially the electrical origins of measured potentials on the scalp, in the form of inverse dipole solutions, are compared to cortical structures presumed to contain these neural sources. The true relationship between functional and anatomical localization is unclear for any given stimulation study and some degree of inter-subject and inter-observer variability is to be expected (Sobel et al., 1993; Kennedy et al., 1998). As there exists no ideal single, non-invasive localization strategy for the primary sensory hand area, greater confidence in its correct identification can be obtained from the convergence of multiple independent techniques including EEG inverse solutions. These also include magnetoencephalography (MEG) (Hari et al., 1984; Kaukoranta et al., 1986; Hari, 1991; Suk et al., 1991; Gallen et al., 1993; Hari et al., 1993; Yang et al., 1993; Kristeva-Feige et al., 1994; Kristeva-Feige et al., 1995; Nakamura et al., 1998), functional magnetic resonance imaging (fMRI) (Hammeke et al., 1994; Rao et al., 1995; Sakai et al., 1995; Puce et al., 1995; Lin et al., 1996; Pujol et al., 1996; Kurth et al., 1998; Gotman et al., 2004; Bagshaw et al., 2006; Gotman et al., 2006; Gotman and Pittau, 2011), and positron emission tomography (PET) (Fox et al., 1987; Nyberg et al., 1996; Bittar et al., 1999), or a combination of the above (Buchner et al., 1994b; Dhawan et al., 1995; Sipilä et al., 2000; George et al., 2000; Bast et al., 2007). To this end, vibrotactile functional MRI studies are also performed on the same three subjects tested with median nerve stimulation in Chapter 4. Although this work is still ongoing and is not the focus of this thesis, preliminary results demonstrate concordance with anatomical localizations and N_{20}-P_{20} SEP inverse solutions. However, considering the similarities in dipole positions with the different conventional and reciprocal approaches (see Section 5.2.3), it is unlikely that this fMRI data will modify the conclusions presented here. Still, these results may provide additional validation of our N_{20}-P_{20} SEP inverse solutions overall. Further validation of N_{20}-P_{20} SEP solutions can also be obtained with more subjects and, once again, decreased time and storage requirements for the reciprocal approaches facilitates their application to a larger number of studies.

Other areas of interest include different evoked potentials (Lopes da Silva, 2004), epileptic spikes, or the early stages of an epileptic seizure (Ebersole and Wade, 1990; Boon and D'Havé, 1995; Boon et al., 1996; Merlet and Gotman, 1999; Boon et al., 2000; Ebersole, 2000; Gross et al., 2000; Gotman, 2003; Lantz et al., 2003; Ebersole and Hawes-Ebersole, 2007; Plummer et al., 2008; Rose and Ebersole, 2009; Plummer et al., 2010; Wang et al., 2011), in which current dipoles may also be adequate models for the electrical sources of these brain events. The possibility of obtaining actual intra-cerebral recordings in these latter cases would provide us with the most reliable estimations of inverse solution accuracy for our different approaches (Homma et al., 2001; Kobayashi et al., 2001; Merlet and Gotman, 2001; Tao et al., 2005; Bénar et al, 2006; Baumgärtner et al., 2010; Pittau et al., 2011). Finally, comparing our programs in terms of accuracy and computational requirements with commercially applications such as BESA and CURRY would also be of interest. For example, using the same N_{20}-P_{20} SEP data set, a subsequent paper could compare our results with those produced by BESA and CURRY for both anatomical and functional localizations of the primary sensory hand area (i.e., MRI and fMRI data, respectively) and employing differing source analysis strategies (e.g., multiple-dipole modeling, spatio-temporal dipole modeling, MUSIC, etc.). Again the findings of such a study, although they may validate our N_{20}-P_{20} SEP inverse solutions further, are unlikely to modify the conclusions of this thesis and therefore have not been included here.

Chapter 6 Conclusion

Boundary-element method (BEM) equations for the conventional centroid (CC), conventional vertex (CV), reciprocal centroid (RC), and reciprocal vertex (RV) approaches to the EEG forward problem are derived using a weighted-residual formulation, and details of their numerical implementation are described for a fairly general volume conductor geometry. These approaches are validated on a three-concentric-spheres head model consisting of planar triangles assuming either a constant (CC and RC) or linear (CV and RV) potential variation on those triangles as well as flux variation for the reciprocal approaches. The performance of the conventional and reciprocal approaches is evaluated for radial and tangential dipoles of varying eccentricities and two widely different skull conductivities.

While the conventional vertex or CV approach yields the most accurate forward solutions for skull conductivities close to recently measured values, the reciprocal approaches offer the least variation in accuracy for different skull conductivities. Contrary to previous results, both conventional and reciprocal approaches exhibit large errors in scalp potentials for highly eccentric dipoles. In terms of single-dipole inverse solutions, conventional and reciprocal approaches demonstrate comparable accuracy. Localization errors are low even for highly eccentric dipoles on account of the nonlinear nature of the single-dipole inverse solution. Both approaches are also found to be equally robust to skull conductivity errors in the presence of noise.

More realistic head models are obtained using Magnetic Resonance Imaging (MRI) from which the scalp, skull, and brain/CSF surfaces are extracted. The two approaches are validated on this type of model using actual Somatosensory Evoked Potentials (SEPs) following median nerve stimulation in three healthy subjects. Conventional and reciprocal approaches have similar solution profiles including small dipole position errors when compared to the nearest point of the primary sensory hand area identified on MRI. Position errors for single-dipole inverse solutions are inherently robust to inaccuracies in forward solutions but intrinsically dependent on the overlapping activity of other underlying neural sources. Smaller time and storage requirements remain the principal advantages of the reciprocal approach.

Reduced computational requirements and similar dipole position accuracy support the use of reciprocal approaches over conventional approaches for N_{20}-P_{20} SEP source localization and facilitates their application to a larger number of studies. Both reciprocal and conventional approaches are equally applicable to alternative inverse solutions such as spatio-temporal and/or multiple dipole localization, MUSIC, and ICA, and the robustness of dipole position error may still hold true in these cases. Although the reciprocal approaches do not produce more accurate dipole positions, they may still lead to increased precision in linearly determined inverse parameters such as dipole amplitude and orientation, cortical potentials, or the amplitudes of a fixed layer of cortical dipoles. Future work also involves comparing results for reciprocal and conventional approaches with intra-cerebral electrode recordings, as well as other imaging modalities including MEG, functional MRI, and PET or a combination of the above.

Bibliography

Abboud, S., Eshel, Y., Levy, S., and Rosenfeld, M. (1994). Numerical calculation of the potential distribution due to dipole sources in a spherical head model. *Comp Biomed Res*, 27, 441-455.

Abboud, S., Rosenfeld, M., and Luzon, J. (1996). Effect of source localization on the scalp potential distribution due to dipole sources in a spherical model of the head. *IEEE Trans Biomed Eng*, 43, 690-696.

Achim, A., Richer, F., and Saint-Hilaire, J. (1991). Methodoloigical considerations for the evaluation of spatio-temporal source models. *Electroenceph Clin Neurophysiol*, 79, 227-240.

Akalin-Acar, Z. and Gençer, N.G. (2004). An advanced boundary element method (BEM) implementation for the forward problem of electromagnetic source imaging. *Phys Med Biol*, 49, 5011-5028.

Allison, T. (1982). Scalp and cortical recordings of initial somatosensory cortex activity to median nerve stimulation in man. *Ann N Y Acad Sci*, 112, 671-677.

Allison, T., McCarthy, G., Wood, C.C., Darcey, T.M., Spencer, D.D., and Williamson, P.D. (1989). Human cortical potentials evoked by electrical stimulation of the median nerve. *J Neurophysiol*, 62, 694-710.

Ary, J.P., Klein, S.A., and Fender, D.H. (1981). Location of sources of evoked scalp potentials: Corrections for skull and scalp thickness. *IEEE Trans Biomed Eng*, 28, 447-452.

Awada, K., Jackson, D., Williams, J., Wilton, D., Baumann, S., and Papanicolaou, A.

(1997). Computational aspects of finite element modeling in EEG source localization. *IEEE Trans Biomed Eng*, 44, 736-752.

Awada, K., Jackson, D., Baumann, S., Williams, J., Wilton, D., Fink, P., and Prasky, B. (1998). Effect of conductivity uncertainties and modeling errors on EEG source localization using a 2-D model. *IEEE Trans Biomed Eng*, 45, 1135-1145.

Babiloni, F., Babiloni, C., Carducci, F., Fattorini, L., Anello, C., Honorati, P., and Urbano, A. (1997). High resolution EEG: a new model-dependent spatial deblurring method using a realistically-shaped MR-constructed subject's head model. *Electroenceph Clin Neurophysiol*, 102, 69-80.

Babiloni, F., Carducci, F., Babiloni, C., and Urbano, A. (1998). Improved realistic Laplacian estimate of highly-sampled EEG potentials by regularization techniques. *Electroenceph Clin Neurophysiol*, 106, 336-343.

Bagshaw, A.P., Kobayashi, E., Dubeau, F., Pike, G.B., and Gotman, J. (2006). Correspondance between EEG-fMRI and EEG dipole localization of interictal discharges in focal epilepsy. *Neuroimage*, 30, 417-425.

Baillet, S. and Garnero, L. (1997). A Bayesian approach to introducing anatomo-functional priors in the EEG/MEG inverse problem. *IEEE Trans Biomed Eng*, 44, 374-385.

Balish, M., Kovar, D., Roth, B., and Sato, S. (1993). Influence of noise on dipole localization using the the-sphere head model (3SM) and the realistically shaped head model (RSHM). In: *Proceedings, 45th Annual Meeting of the American Academy of Neurology*.

Barkley, G.L. and Baumgartner, C. (2003). MEG and EEG in epilepsy. *J Clin Neurophysiol*, 20, 163-178.

Barkley, G.L. (2004). Controversies in neurophysiology. MEG is superior to EEG in localization of interictal epileptiform activity: Pro. *Clin Neurophysiol*, 115, 1001-1009.

Barnard, A.C.L., Duck, I.M., Lynn, M.S., and Timlake, W.P. (1967). The application of electromagnetic theory to electrocardiology. II. Numerical solution of the integral equations. *Biophys J*, 7, 463-491.

Bast, T., Wright, T., Boor, R., Harting, I., Feneberg, R., Rupp, A., Hoechstetter, K., Rating, D., and Baumgärtner, U. (2007). Combined EEG and MEG analysis of early somatosensory evoked activity in children and adolescents with focal epilepsies. *Clin Neurophysiol*, 118, 1721-1735.

Baumgartner, C., Barth, D.S., Levesque, M.F., and Sutherling, W.W. (1991). Functional anatomy of human hand sensorimotor cortex from spatiotemporal analysis of electrocorticography. *Electroenceph Clin Neurophysiol*, 78, 56-65.

Baumgartner, C. (2004). Controversies in neurophysiology. MEG is superior to EEG in localization of interictal epileptiform activity: Con. *Clin Neurophysiol*, 115, 1010-1020.

Baumgärtner, U., Vogel, H., Ohara, S., Treede, R.D., and Lenz, F.A. (2010). Dipole source analyses of early median nerve SEP components obtained from subdural grid recordings. *J Neurophysiol*, 104, 3029-3041.

Bénar, C.G., Gunn, R.N., Grova, C., Champagne, B., and Gotman, J. (2005). Statistical maps for EEG dipolar source localization. *IEEE Trans Biomed Eng*, 52, 401-413.

Bénar, C.G., Grova, C., Kobayashi, E., Bagshaw, A.P., Aghakhani, Y., Dubeau, F., and Gotman, J. (2006). EEG-fMRI of epileptic spikes: concordance with EEG source localization and intracranial EEG. *Neuroimage*, 30, 1161-1170.

Berger, M.S., Kincaid, J., Ojemann, G.A., and Lettich, E. (1989). Brain mapping techniques to maximize resection, safety, and seizure control in children with brain tumors. *Neurosurgery*, 25, 786-792.

Bittar, R.G., Olivier, A., Sadikot, A.F., Andermann, F., Comeau, R.M., Cyr, M., Peters, T.M., and Reutens, D.C. (1999). Localization of somatosensory function by using positron emission tomography scanning: a comparison with intraoperative cortical stimulation. *J Neurosurg*, 90, 478-483.

Blum, D. (1998). Computer-based electroencephalography: technical basics, basis for new applications, and potential pitfalls. *Electroenceph Clin Neurophysiol*, 106, 118-126.

Boling, W., Olivier, A., Bittar, R.G., and Reutens, D. (1999). Localization of hand motor activation in Broca's pli de passage moyen. *J Neurosurg*, 91, 903-910.

Boon, P. and D'Havé, M. (1995). Interictal and ictal dipole modeling in patients with refractory partial epilepsy. *Acta Neuro Scand*, 92, 7-18.

Boon, P., D'Havé, M., Vonck, K., Baulac, T., Vandekerckhove, T., and de Reuck, J. (1996). Dipole modeling in epilepsy surgery candidates. *Epilepsia*, 38, 208-218.

Boon, P., D'Have, M., Van Hoey, G., Vanrumste, B., Vonck, K., Adam, C., and Vandekerckhove, T. (2000). Interictal and ictal source localization in neocortical versus medial temporal lobe epilepsy. *Adv Neurol*, 84, 365-375.

Brebbia, C.A. and Dominguez, J. (1992). *Boundary Elements: An Introductory Course*. 2nd ed., Southampton, U.K.: WIT Press, Chap. 2.

Brigell, M., Rubboli, G., and Celesia, G. (1993). Identification of the hemisphere activated by hemifield visual stimulation using a single equivalent dipole model. *Electroenceph Clin Neurophysiol*, 87, 291-299.

Brinkmann, B.H., O'Brien, T.J., Dresner, M.A., Lagerlund, T.D., Sharbrough, F.W., and Robb, R.A. (1998). Scalp-recorded EEG localization in MRI volume data. *Brain Topogr*, 10, 245-253.

Broca, P. (1888). Description elémentaires des circonvolutions cérébrales de l'homme. *Mémoires d'Anthropologie*. Memo Paris: C. Reinwald, 707-804.

Brody, D., Terry, F., and Ideker, R. (1973). Eccentric dipole in a spherical medium: Generalized expression for surface potentials. *IEEE Trans Biomed Eng*, 20, 141-143.

Bronzino, J.D. (1995). Principles of electroencephalography. In: Bronzino, J.D., ed. *The Biomedical Engineering Handbook*. Florida: CRC Press, 201-212.

Buchner, H., Adams, L., Knepper, A., Rüger, R., Laborde, G., Gilsbach, J.M., Ludwig, I., Reul, J., and Scherg, M. (1994a). Preoperative localization of the central sulcus by dipole source analysis of early somatosensory evoked potentials and three-dimensional magnetic resonance imaging. *J Neurosurg*, 80, 849-856.

Buchner, H., Fuchs, M., Wischmann, H.A., Dössel, O., Ludwig, I., Knepper, A., and Berg, P. (1994b). Source analysis of median nerve and finger stimulated somatosensory evoked potentials: multichannel simultaneous recording of electric and magnetic fields combined with 3D-MR tomography. *Brain Topogr*, 6, 299-310.

Buchner, H., Adams, L., Müller, A., Ludwig, I., Knepper, A., Thron, A., Niemann, K., and Scherg, M. (1995a). Somatotopy of human hand somatosensory cortex revealed by dipole source analysis of early somatosensory evoked potentials and 3D-NMR tomography. *Electroenceph Clin Neurophysiol*, 96, 121-134.

Buchner, H., Waberski, T.D., Fuchs, M., Wischmann, H.-A., Wagner, M., and Drenckhahn, R. (1995b). Comparison of realistically shaped boundary-element and spherical head models in source localization of early somatosensory evoked potentials. *Brain Topogr*, 8, 137-143.

Buchner, H., Knoll, G., Fuchs, M., Rienäcker, A., Beckmann, R., Wagner, M., Silny, J., and Pesch, J. (1997). Inverse localization of electric dipole current sources in finite element models of the human head. *Electroenceph Clin Neurophysiol*, 102, 267-278.

Burchiel, K.J., Clarke, H., Ojemann, G.A., Dacey, R.G., and Winn, H.R. (1989). Use of stimulation mapping and corticography in the excision of arteriovenous malformations in sensorimotor and language-related neocortex. *Neurosurgery*, 24, 322–327.

Butler, S., Georgiou, G., Glass, A., Hancox, R., Hopper, I., and Smith, K. (1987). Cortical generators of the CI component of the pattern-onset visual evoked potential. *Electroenceph Clin Neurophysiol*, 68, 256-267, 1987.

Caceci, M.S. and Cacheris, W.P. (1984). Fitting curves to data. The simplex algorithm is the answer. *Byte*, 9, 340-362.

Cardenas, V., Yingling, C., Jewett, D., and Fein, G. (1995). A multi-channel, model-free method for estimation of event-related potential amplitudes and its comparison with dipole source localization. *J Med Eng Tech*, 19, 88-98.

Chang, N., Gulrajani, R., and Gotman, J. (2005). Dipole localization using simulated intracerebral EEG. *Clin Neurophysiol*, 116, 2707-2716.

Cohen, D. and Cuffin, B.N. (1983). Demonstration of useful differences between magnetoencephalogram and electroencephalogram. *Electroenceph Clin Neurophysiol*, 56, 38-51.

Cohen, D., Cuffin, B., Yunokuchi, K., Maniewski, R., Purcell, C., Cosgrove, G., Ives, J., Kennedy, J., and Schomer, D. (1990). MEG versus EEG localization test using implanted sources in the human brain [see comments]. *Ann Neurol*, 28, 811-817.

Cuffin, B. (1985). A comparison of moving dipole inverse solutions using EEG's and

MEG's. *IEEE Trans Biomed Eng*, 32, 905-910.

Cuffin, B. (1991). Eccentric spheres models of the head. *IEEE Trans Biomed Eng*, 38, 871-878.

Cuffin, B., Cohen, D., Yunokuchi, K., Maniewski, R., Purcell, C., Cosgrove, G.R., Ives, J., Kennedy, J., and Schomer, D. (1991). Tests of EEG localization accuracy using implanted sources in the human brain. *Ann Neurol*, 29, 132-138.

Cuffin, B. (1993). Effects of local variations in skull and scalp thickness on EEG's and MEG's. *IEEE Trans Biomed Eng*, 40, 42-48.

Cuffin, B. (1995). A method for localizing EEG sources in realistic head models. *IEEE Trans Biomed Eng*, 42, 68-71.

Cuffin, B.N., Schomer, D.L., Ives, J.R., and Blume, H. (2001). Experimental tests of EEG source localization accuracy in realistically shaped volume conductors. *Clin Neurophysiol*, 112, 2288-2291.

De Munck, J.C. (1988). The potential distribution in a layered anisotropic spheroidal volume conductor. *J Appl Phys*, 64, 464-470.

De Munck, J.C., van Dijk, B.W., and Spekreijse, H. (1988a). An analytic method to determine the effect of source modeling errors on the apparent location and direction of biological sources. *J Appl Phys*, 63, 944-956.

De Munck, J.C., van Dijk, B.W., and Spekreijse, H. (1988b). Mathematical dipoles are adequate to describe realistic generators of human brain activity. *IEEE Trans Biomed Eng*, 35, 960-966.

De Munck, J.C. (1990). The estimation of time varying dipoles on the basis of evoked potentials. *Electroenceph Clin Neurophysiol*, 77, 156-160.

De Munck, J.C., Vijn, P., and Spekreijse, H. (1991). A practical method for determining electrode positions on the head. *Electroenceph Clin Neurophysiol*, 78, 85-87.
De Munck, J.C. (1992). A linear discretization of the volume conductor boundary integral equation using analytically integrated elements. *IEEE Trans Biomed Eng*, 39, 986-990.

Dhawan, A., Arata, L., Levy, A., and Mantil, J. (1995). Iterative principal axis registration method for analysis of MR-PET brain images. *IEEE Trans Biomed Eng*, 42, 1079-1087.

Diekmann, V., Becker, W., Jürgens, R., Grözinger, B., Kleiser, B., Richter, H., and Wollinsky, K. (1998). Localization of epileptic foci with electric, magnetic and combined electromagnetic models. *Electroenceph Clin Neurophysiol*, 106, 297-313.

Ebersole, J.S. and Wade, P.B. (1990). Spike voltage topography and equivalent dipole localization in complex partial epilepsy. *Brain Topogr*, 3, 21-34.

Ebersole, J.S. (1997). Defining epileptogenic foci: past, present, future. *J Clin Neurophysiol*, 14, 470-483.

Ebersole, J.S. (1999). Editorial. The last word. *J Clin Neurophysiol*, 16, 297-302.

Ebersole, J.S. (2000). Noninvasive localization of epileptogenic foci by EEG source modeling. *Epilepsia*, 41, S24-33.

Ebersole, J.S. and Hawes-Ebersole, S. (2007). Clinical application of dipole models in the localization of epileptiform activity. *J Clin Neurophysiol*, 24, 120-129.

Eshel, Y., Witman, S., Rosenfeld, M., and Abboud, S. (1995). Correlation between skull thickness asymmetry and scalp potential estimated by a numerical model of the head.

IEEE Trans Biomed Eng, 42, 242-249.

Fender, D.H. (1987). Source localization of brain electric activity. In: Gevins, A.S. and Remond, A., eds. *Handbook of Electroencephalography and Clinical Neurophysiology*. New York: Elsevier, 355-403.

Fender, D.H. (1991). Models for the human brain and the surrounding media: their influence on the reliability of source localization. *J Clin Neurophysiol*, 8, 381-390.

Ferguson, A.S. and Stroink, G. (1997). Factors affecting the accuracy of the boundary element method in the forward problem - I. Calculating surface potentials. *IEEE Trans Biomed Eng*, 44, 1139-1155.

Ferree, T. and Tucker, D. (1999). Development of high-resolution EEG devices. *Int J Bioelectromag*, 1, 4-10.

Finke, S. (1998). Évaluation de la méthode conventionnelle et de la méthode réciproque pour la résolution du problème direct en électroencéphalographie. *Mémoire de M.Sc.A. (Génie Biomédical)*. École Polytechnique de Montréal, Montreal, Canada.

Finke, S. and Gulrajani, R.M. (1999). Comparative accuracy of EEG forward solutions. In: *Proceedings, 1st Joint Biomedical Engineering Society and IEEE Engineering in Medicine and Biology Society Meeting*, 435.

Finke, S. and Gulrajani, R.M. (2000). An evaluation of the reciprocal approach for computing scalp EEG potentials. In: *Proceedings, 3rd International Conference on Bioelectromagnetism*, 129-130.

Finke, S. and Gulrajani, R.M. (2001). Conventional and reciprocal approaches to the forward problem of electroencephalography. *Electromagnetics*, 21, 513-530.

Finke, S., Gulrajani, R.M., and Gotman, J. (2001). The reciprocal approach to the inverse problem of electroencephalography. In: *Proceedings, 23rd Annual International Conference of the IEEE Engineering in Medicine and Biology Society*, 980-983.

Finke, S., Gulrajani, R.M., and Gotman, J. (2002). Skull conductivity errors and the inverse problem of electroencephalography. In: *Proceedings, 4th International Conference on Bioelectromagnetism*, 4, 221-222.

Finke, S., Gulrajani, R.M., and Gotman, J. (2003a). Simplex minimization and the inverse dipole localization problem of electroencephalography. In: *Proceedings, 25th Annual International Conference of the IEEE Engineering in Medicine and Biology Society*, CD-ROM.

Finke, S., Gulrajani, R.M., and Gotman, J. (2003b). Conventional and reciprocal approaches to the inverse dipole localization problem of electroencephalography. *IEEE Trans Biomed Eng*, 50, 657-666.

Fischer, G., Tilg, B., Wach, P., Modre, R., Leder, U., and Nowak, H. (1999). Application of high-order boundary elements to the electrocardiographic inverse problem. *Comp Methods Prog Biomed*, 58, 119-131.

Fletcher, D.J., Jewett, D., Zhang, Z., and Amir, A. (1993). The effects of skull shape on single and multiple dipole source localizations. In: *Proceedings, 15th Annual International Conference* of *IEEE Engineering in Medicine and Biology Society*.

Fletcher, D.J., Amir, A., Jewett, D.L., and Fein, G. (1995). Improved method for computation of potentials in a realistic head shape model. *IEEE Trans Biomed Eng*, 42, 1094-1104.

Forsythe, G.E. and Moler, C.B. (1967). *Computer Solution of Linear Algebraic Systems*. Englewood Cliffs, NJ: Prentice-Hall, 16.

Foster, K.R. and Swan, H.P. (1989). Dielectric properties of tissues and biological materials: A critical review. *Crit Rev Biomed Eng*, 17, 25-104.

Fox, P.T., Burton, H., and Raichle, M.E. (1987). Mapping human somatosensory cortex with positron emission tomography. *J Neurosurg*, 67, 34-43.

Frank, E. (1952). Electric potential produced by two point current sources in a homogenous conduction sphere. *J Appl Phys*, 23, 1225-1228.

Franssen, H., Stegeman, D.F., Moleman, J., and Schoobaar, R.P. (1992). Dipole modeling of median nerve SEPs in normal subjects and patients with small subcortical infarcts. *Electroenceph Clin Neurophysiol*, 84, 401-417.

Freeman, W. (1980). Use of spatial deconvolution to compensate for distortion of EEG by volume conduction. *IEEE Trans Biomed Eng*, 27, 421-429.

Frijns, J.H.M., de Snoo, S.L., and Schoonhoven, R. (2000). Improving the accuracy of the boundary element method by the use of second-order interpolation functions. *IEEE Trans Biomed Eng*, 47, 1336-1346.

Fuchs, M., Drenckhahn, R., Wischmann, H., and Wagner, M. (1998a). An improved boundary element method for realistic volume-conductor modeling. *IEEE Trans Biomed Eng*, 45, 980-997.

Fuchs, M., Wagner, M., Wischmann, H., Köhler, T., Theissen, A., Drenckhahn, R., and Buchner, H. (1998b). Improving source reconstructions by combining bioelectric and biomagnetic data. *Electroenceph Clin Neurophysiol*, 107, 93-111.

Fuchs, M., Wagner, M., Köhler, T., and Wischmann, H. (1999). Linear and nonlinear current density reconstructions. *J Clin Neurophysiol*, 16, 267-295.

Fuchs, M., Wagner, M., and Kastner, J. (2001). Boundary element method volume conductor models for EEG source reconstruction. *Clin Neurophysiol*, 112, 1400-1407.

Fuchs, M., Kastner, J., Wagner, M., Hawes, S., and Ebersole, J.S. (2002). A standardized boundary element method volume conductor model. *Clin Neurophysiol*, 113, 702-712.

Fuchs, M., Ford, M.R., Sands, S., and Lew, H.L. (2004). Overview of dipole source localization. *Phys Med Rehabil Clin N Am*, 15, 251-262.

Fuchs, M., Wagner, M., and Kastner, J. (2007). Development of volume conductor and source models to localize epileptic foci. *J Clin Neurophysiol*, 24, 101-119.

Gabriel, S., Lau, R., and Gabriel, C. (1996). The dielectric properties of biological tissues: I. Measurements in the frequency range 10 Hz to 20 GHz. *Phys Med Biol*, 41, 2251-2269.

Gallen, C.C., Sobel, D.F., Waltz, T., Aung, M., Copeland, B., Schwartz, B.J., Hirschkoff, E.C., and Bloom, F.E. (1993). Noninvasive presurgical neuromagnetic mapping of somatosensory cortex. *Neurosurgery*, 33, 260-268.

Gaumond, R., Lin, J., and Geselowitz, D. (1983). Accuracy of dipole localization with a spherical homogeneous model. *IEEE Trans Biomed Eng*, 30, 29-34.

Geddes, L. and Baker, L. (1967). The specific resistance of biological material – a compendium of data for the biomedical engineer and physiologist. *Med Biol Eng*, 5, 271-293.

Geman, S. and Geman, D. (1984). Stochastic relaxation, Gibbs distribution and the Bayesian restoration of images. *IEEE Trans Pattern Anal Mach Intell*, 6, 721-741.

Gençer, N.G. and Williamson, S. (1998). Differential characterization of neural sources with the bimodal truncated SVD pseudo-inverse for EEG and MEG measurements. *IEEE Trans Biomed Eng*, 45, 827-838.

Gençer, N.G. and Tanzer, I.O. (1999). Forward problem solution of electromagnetic source imaging using a new BEM formulation with high-order elements. *Phys Med Biol*, 44, 2275-2287.

Gençer, N.G. and Akalin-Acar, Z. (2005). Use of the isolated problem approach for multi-compartment BEM models of electro-magnetic source imaging. *Phys Med Biol*, 50, 3007-3022.

George, J., Aine, C., Mosher, J., Schmidt, D., Ranken, D., SChlitt, H., Wood, C., Lewine, J., Sanders, J., and Belliveau, J. (2000). Mapping function in the human brain with magnetoencephalography, anatomical magnetic resonance imaging, and functional magnetic resonance imaging. *J Clin Neurophysiol*, 12, 406-431.

Gerson, J., Cardenas, V., and Fein, G. (1994). Equivalent dipole parameter estimation using simulated annealing. *Electroenceph Clin Neurophysiol*, 92, 161-168.

Geselowitz, D.B. (1967). On bioelectric potentials in an homogenous volume conductor. *Biophys J*, 7, 1-11.

Geva, A., Pratt, H., and Zeevi, Y. (1995). Spatio-temporal multiple source localization by wavelet-type decomposition of evoked potentials. *Electroenceph Clin Neurophysiol*, 96, 278-286.

Gevins, A.S. and Bressler, S.L. (1988). Functional topography of the human brain. In: Pfurtscheller, G. and Lopes da Silva, F.H., eds. *Functional Brain Imaging*. Bern: Hans Huber, 99-116.

Gevins, A.S., Bricked, P., Costales, B., Le, J., and Reuter, B. (1990). Beyond topographic mapping: towards functional-anatomical imaging with 124-channel EEGs and 3-D MRIs. *Brain Topogr*, 3, 53-64.

Gevins, A.S., Le, J., Martin, N., Bricked, P., Desmond, J., and Reutter, B. (1994). High resolution EEG: 124-channel recording, spatial deblurring and MRI integration methods. *Electroenceph Clin Neurophysiol*, 90, 337-358.

Gevins, A.S. (1998). The future of electroencephalography is assessing neurocognitive functioning. *Electroenceph Clin Neurophysiol*, 106, 165-172.

Gevins, A.S., Le, J., Leong, H., McEvoy, L., and Smith, M. (1999). Deblurring. *J Clin Neurophysiol*, 16, 204-213.

Gonçalves, S., de Munck, J.C., Heethaar, R.M., Lopes da Silva, F.H., and van Dijk, B.W. (2000). The application of electrical impedance tomography to reduce systematic errors in the EEG inverse problem – a simulation study. *Physiol Meas*, 21, 379–393.

Gorodnitsky, I., George, J., and Rao, B. (1995). Neuromagnetic source imaging with FOCUSS: a recursive weighted minimum norm algorithm. *Electroenceph Clin Neurophysiol*, 95, 231-251.

Gotman, J. (2003). Noninvasive methods for evaluating the localization and propagation of epileptic activity. *Epilepsia*, 44, 21-29.

Gotman, J., Bénar, C.G., and Dubeau, F. (2004). Combining EEG and fMRI in epilepsy: methodological challenges and clinical results. *J Clin Neurophysiol*, 21, 229-240.

Gotman, J., Kobayashi, E., Bagshaw A.P., Bénar, C.G., and Dubeau, F. (2006). Combined EEG and fMRI: a multimodal tool for epilepsy research. *J Magn Reson Imaging*, 23, 906-920.

Gotman, J. and Pittau, F. (2011). Combined EEG and fMRI in the study of epileptic discharges. *Epilepsia*, 52, 38-42.

Grave de Peralta Menendez, R. and Gonzalez Andino, S.L. (1994). Single dipole localization: Some numerical aspects and apractical rejection criterion for the fitted parameters. *Brain Topogr*, 6, 277-282.

Grech, R., Cassar, T., Muscat, J., Camilleri, K.P., Fabri, S.G., Zervakis, M., Xanthopoulos, P., Sakkalis, V., and Vanrumste, B. (2008). Review on solving the inverse problem in EEG source analysis. *J Neuroeng Rehabil*, 5, 25.

Greenblatt, R. (1993). Probabilistic reconstruction of multiple sources in the bioelectromagnetic inverse problem. *Inv Prob*, 271-284.

Gross, D.W., Merlet, I., Boling, W., and Gotman, J. (2000). Relationships between the epileptic focus and hand area in central epilepsy: combining dipole models and anatomical landmarks. *J Neurosurg*, 92, 785-792.

Gulrajani, R.M., Roberge, F., and Savard, P. (1984). Moving dipole inverse ECG and EEG solutions. *IEEE Trans Biomed Eng*, 31, 903-910.

Gulrajani, R.M. (1998). *Bioelectricity and Biomagnetism*. New York: Wiley, Chap. 5.

Gulrajani, R.M., Finke, S., and Gotman, J. (2001). Reciprocal transfer-coefficient matrices and the inverse problem of electroencephalography. In: *Proceedings, 3rd International Symposium on Noninvasive Functional Source Imaging within the Human Heart and Brain, Biomedizinische Technik*, 46, 13-15.

Hallez, H., Vanrumste, B., Van Hese, P., D'Asseler, Y., Lemahieu, I., and Van de Walle, R. (2005). A finite difference method with reciprocity used to incorporate anisotropy in electroencephalogram dipole source localization. *Phys Med Biol*, 50, 3878-3806.

Hallez, H., Vanrumste, B., Grech, R., Muscat, J., De Clercq, W., Vergult, A., D'Asseler, Y., Camilleri, K.P., Fabri, S.G., and Lemahieu, I. (2007). Review on solving the forward problem in EEG source analysis. *J Neuroeng Rehabil*, 4, 46.

Hämäläinen, M.S. and Sarvas, J. (1989). Realistic conductivity geometry model of the human head for interpretation of neuromagnetic data. *IEEE Trans Biomed Eng*, 36, 165-171.

Hammeke, T.A., Yetkin, F.Z., Mueller, W.M., Morris, G.L., Haughton, V.M., Rao, S.M., and Binder, J.R. (1994). Functional magnetic resonance imaging of somatosensory stimulation. *Neurosurgery*, 35, 677-681.

Hara, J., Musha, T., and Shankle, W.R. (1999). Approximating dipoles from human EEG activity: The effect of dipole source configuration on dipolarity using single dipole models. *IEEE Trans Biomed Eng*, 46, 125-129.

Hari, R., Reinikainen, K., Kaukoranta, E., Hämäläinen, M., Ilmoniemi, R., Penttinen, A., Saluonen, J., and Teszner, D. (1984). Somatosensory evoked cerebral magnetic fields from SI and SII in man. *Electroenceph Clin Neurophysiol*, 57, 254-263.

Hari, R. (1991). On brain magnetic responses to sensory stimuli. *J Clin Neurophysiol*, 8, 157-169.

Hari, R., Karhu, J., Hämäläinen, M., Knuutila, J., Salonen, O., Sams, M., and Vilkman, V. (1993). Functional organization of the human first and second somatosensory cortices: a neuromagnetic study. *Eur J Neurosci*, 5, 724-734.

Haueisen, J., Ramon, C., Eiselt, M., Brauer, H., and Nowak, H. (1997). Influence of tissue resistivities on neuromagnetic fields and electric potentials studied with a finite element model of the head. *IEEE Trans Biomed Eng*, 44, 727-735.

Hayashi, N., Endo, S., Kurimoto, M., Nishijo, H., Ono, T., and Takaku, A. (1995). Functional image-guided neurosurgical stimulation system using computerized three-dimensional graphics and dipole tracing. *Neurosurgery*, 37, 694-703.

He, B., Musha, T., Okamoto, Y., Homma, S., Nakajima, Y., and Sato, T. (1987). Electric dipole tracing in the brain by means of the boundary element method and its accuracy. *IEEE Trans Biomed Eng*, 34, 406-414.

He, B. and Musha, T. (1989). Effects of cavities on EEG dipole localization and their relations with surface electrode positions. *Int J Biomed Comput*, 24, 269-282.

He, B., Wang, Y., and Wu, D. (1999). Estimating cortical potentials from Scalp EEG's in a realistically shaped inhomogeneous head model by means of the boundary element method. *IEEE Trans Biomed Eng*, 46, 1264-1268.

He, B., Zang. X., Lian, J., Sasaki, H., Wu, D., and Towle, V.L. (2002). Boundary element method based cortical potential imaging of somatosensory evoked potentials using subjects' magnetic resonance images. *Neuroimage*, 16, 564-576.

Heinonen, T., Eskola, H., Dastidar, P., Laarne, P., and Malmivuo, J. (1997). Segmentation of T1 MR scans for reconstruction of resistive head models. *Comp Met Prog Biomed*, 54, 173-181.

Heinonen, T., Lahtinen, A, and Häkkinen, V. (1999). Implementation of three-dimensional EEG brain mapping. *Comput Biol Res*, 32, 123-131.

Heller, L. (1990). Computation of the return current in encephalography: The auto solid angle. In: *Proceedings, SPIE, Digital Image Synthesis and Inverse Optics*, 1351, 376-390.

Helmholtz, H. (1853). Über einige Gesetze der Vertheilung elektrischer Ströme in körperlichen Leitern mit Anwendung auf die thierisch-elektrischen Versuche [Some laws concerning the distribution of electrical currents in conductors with applications to experiments on animal electricity]. *Annalen der Physik und Chemie*, 89, 211-233.

Henderson, C.J., Butler, S.R., and Glass, A. (1975). The localization of equivalent dipoles of EEG sources by the application of electrical field theory. *Electroenceph Clin Neurophysiol*, 39, 117-130.

Herrendorf, G., Steinhoff, B.J., Kolle, R., Baudewig, J., Waberski, T.D., Buchner, H., and Paulus, W. (2000). Dipole-source analysis in a realistic head model in patients with focal epilepsy. *Epilepsia*, 41, 71-80.

Hirsch, J., Ruge, M.I., Kim, K.H.S., Correa, D.D., Victor, J.D., Relkin, N.R., Labar, D.R., Krol, G., Bilsky, M.H., Souweidane, M.M., DeAngelis, L.M., and Gutin, P.H. (2000). An integrated functional magnetic resonance imaging procedure for preoperative mapping of cortical areas associated with tactile, motor, language, and visual functions. *Neurosurgery*, 47, 711-722.

Hjorth, B. (1975). An on-line transformation of EEG scalp potentials into orthogonal source derivations. *Electroenceph Clin Neurophysiol*, 39, 526-530

Hjorth, B. (1991). Principles for transformation of scalp EEG from potential field into source distribution. *J Clin Neurophysiol*, 8, 391-396.

Homma, S., Musha, T., Nakajima, Y., Okamoto, Y., Blom, S., Flink, R., Hagbarth, K., and Moström, U. (1994). Location of electric current sources in the human brain estimated by the dipole tracing method of the scalp-skull-brain (SSB) head model.

Electroenceph Clin Neurophysiol, 91, 374-382.

Homma, S., Musha, T., Nakajima, Y., Okamoto, Y., Blom, S., Flink, R., and Hagbarth, K. (1995). Conductivity ratios of the scalp-skull-brain head model in estimating equivalent dipole sources in human brain. *Neurosci Res*, 22, 51-55.

Homma, I., Masaoka, Y., Hirasawa, K., Yamane, F., Hori, T., and Okamoto, Y. (2001). Comparison of source localization of Interictal epileptic spike potentials in patients estimated by the dipole tracing method with the focus directly recorded by the depth electrodes. *Neurosci Lett*, 304, 1-4.

Hosek, R.S., Sances, A.I., Jodat, R.W., and Larson, S.I. (1978). The contributions of intracerebral currents to the EEG and evoked potentials. *IEEE Trans Biomed Eng*, 25, 405-413.

Huiskamp, G., Vroeijenstijn, M., van Dijk, R., Wieneke, G., and van Huffelen, A. (1999). The need for correct realistic geometry in the inverse EEG problem. *IEEE Trans Biomed Eng*, 46, 1281-1287.

Huppertz, H., Otte, M., Grimm, C., Kristeva-Feige, R., Mergner, T., and Lücking, C. (1998). Estimation of the accuracy of a surface matching technique for registration of EEG and MRI data. *IEEE Trans Biomed Eng*, 106, 409-415.

Ioannides, A. (1991). Comparison of magnetoencephalography with other functional imaging techniques. *Clin Phys Physiol Meas*,12, 23-28.

Iwasaki, S., Nakagawa, H., Fukusumi, A., Kichikawa, K., Kitamura, K., Otsugi, H., Uchida, H., Ohishi, H., Yaguchi, K., Sumie, H., and Kuru, Y. (1991). Identification of pre- and postcentral gyri on CT and MR images on the basis of the medullary pattern of cerebral white matter. *Radiology*, 179, 207-213.

Jasper, H. (1958). Report of the committee on methods of clinical examination in electroencephalography. *Electroenceph Clin Neurophysiol*, 10, 370-371.

Jayakar, P., Duchowny, M., Resnick, T., and Alvarez, L. (1991). Localization of seizure foci: pitfalls and caveats. *J Clin Neurophysiol*, 8, 414-431.

Johnson, C. (1995). Numerical methods for bioelectric field problems. In: Bronzino, J.D., ed. *The Biomedical Engineering Handbook*. Florida: CRC Press, 162-180.

Kaukoranta, E., Hämäläinen, M., Sarvas, J., and Hari, R. (1986). Mixed and sensory nerve stimulations activate different cytoarchitectonic areas in the human primary somatosensory cortex SI. *Exp Brain Res*, 63, 60-66.

Kearfott, R., Sidman, R., Major, D., and Hill, C. (1991). Numerical tests of a method for simulating electrical potentials on the cortical surface. *IEEE Trans Biomed Eng*, 38, 294-299.

Kennedy, D.N., Lange, N., Makris, N., Bates, J., Meyer, J., and Caviness, V.S. Jr. (1998). Gyri of the human neocortex: an MRI-based analysis of volume and variance. *Cereb Cortex*, 8, 372-384.

Khosla, D., Singh, M., and Don, M. (1997). Spatio-temporal EEG source localization using simulated annealing. . *IEEE Trans Biomed Eng*, 44, 1075-1091.

Khosla, D., Don, M., and Kwong, B. (1999). Spatial mislocalization of EEG electrodes – effects on accuracy of dipole estimation. *Clin Neurophysiol*, 110, 261-271.

Kido, D.K., Lemay, M., Levinson, A.W., and Benson, W.E. (1980). Computed tomographic localization of the precentral gyrus. *Radiology*, 135, 373-377.

King, R.B. and Schell, G.R. (1987). Cortical localization and monitoring during cerebral operations. *J Neurosurg*, 67, 210-219.

Kirkpatrick, S., Gelatt, C.D. Jr., and Vecchi, M.P. (1983). Optimization by simulated annealing. *Science*, 220, 671-680.

Kobayashi, K., James, C., Yoshinga, H., Ohtsuka, Y., and Gotman, J. (2000). The electroencephalogram through a software microscope: non-invasive localization and visualization of epileptic seizure activity from inside the brain. *Clin Neurophysiol*, 111, 134-149.

Kobayashi, K., Merlet, I., and Gotman, J. (2001). Separation of spikes from background by independent component analysis with dipole modeling and comparison to intracranial recording. *Clin Neurophysiol*, 112, 405-413.

Kobayashi, K., Akiyama, T., Nakahori, T., Yoshinaga, H., and Gotman, J. (2002a). Systematic source estimation of spikes by a combination of independent component analysis and RAP-MUSIC. I: Principles and simulation study. *Clin Neurophysiol*, 113, 713-724.

Kobayashi, K., Akiyama, T., Nakahori, T., Yoshinaga, H., and Gotman, J. (2002b). Systematic source estimation of spikes by a combination of independent component analysis and RAP-MUSIC. II: Preliminary clinical application. *Clin Neurophysiol*, 113, 725-734.

Kobayashi, K., Yoshinaga, H., Oka, M., Ohtsuka, Y., and Gotman, J. (2003). A simulation study of the error in dipole source localization for EEG spikes with a realistic head model. *Clin Neurophysiol*, 114, 1069-1078.

Kobayashi, K., Yoshinaga, H., Ohtsuka, Y., and Gotman, J. (2005). Dipole modeling of epileptic spikes can be accurate or misleading. *Epilepsia*, 46, 397-408.

Koles, Z.J. (1998). Trends in EEG source localization. *Electroenceph Clin Neurophysiol*, 106, 127-137.

Korvenoja, A, Kirveskari, E., Aronen, H.J., Avikainen, S., Brander, A., Huttunen, J., Ilmoniemi, R.J., Jääskeläinen, J.E., Kovala, T., Mäkelä, J.P., Salli, E., and Seppä, M. (2006). Sensorimotor cortex localization: comparison of magnetoencephalography, functional MR imaging, and intraoperative cortical mapping. *Radiology*, 241, 213-222.

Kosterich, J.D., Foster, K.R., and Pollack, S.R. (1984). Dielectric properties of fluid saturated bone: Effect of variation in conductivity of immersion fluid. *IEEE Trans Biomed Eng*, 31, 369-372.

Krings, T., Chiappa, K., Cuffin, B., Cochius, J., Connolly, S., and Cosgrove, G. (1999). Accuracy of EEG dipole source localization using implanted sources in the human brain. *Clin Neurophysiol*, 110, 106-114.

Kristeva-Feige, R., Walter, H., Lütkenhöner, B., Hampson, S., Ross, B., Knorr, U., Steinmetz, H., and Cheyne, D. (1994). A neuromagnetic study of the functional organization of the sensorimotor cortex. *Eur J Neurosci*, 6, 632-639.

Kristeva-Feige, R., Rossi, R., Pizzella, S., Tecchio, F., Romani, G.L., Erne, S., Edrich, J., Orlacchio, A., and Rossini, P.-M. (1995). Neuromagnetic fields of the brain evoked by voluntary movement and electrical stimulation of the index finger. *Brain Res*, 681, 22-28.

Kristeva-Feige, R., Grimm, C.H., Huppertz, H.-J., Otte, M., Schreiber, A., Jäger, D., Feige, B., Büchert, M., Hennig, J., Mergner, T., and Lücking, C.H. (1997). Reproducibility and validity of electric source localization with high-resolution electroencephalography. *Electroenceph Clin Neurophysiol*, 103, 652-660.

Kurth, R., Villringer, K., and Mackert, B.M., Schwiemann, J., Braun, J., Curio, G., Villringer, A., and Wolf, K.J. (1998). fMRI assessment of somatotopy in human Brodmann area 3b by electrical finger stimulation. *Neuroreport*, 9, 207-212.

Laarne, P. (2000). Implementation of a realistic conductivity model for the head. *Ph.D. Dissertation*. Tampere University of Technology, Tampere, Finland.

Laarne, P., Hyttinen, J., Dodel, S., Malmivuo, J., and Eskola, H. (2000). Accuarcy of two dipolar inverse algorithms applying reciprocity for forward calculation. *Comp Biomed Res*, 33, 172-185.

Lantz, G., Holub, M., Ryding, E., and Rosén, I. (1996). Simultaneous intracranial and extracranial recording of interictal epileptiform activity in patients with drug resistant partial epilepsy: patterns of conduction and results from dipole reconstructions. *Electroenceph Clin Neurophysiol*, 99, 69-78.

Lantz, G., Spinelli, L., Seeck, M., de Peralta Menendez, R.G., Sottas, C.C., and Michel, C.M. (2003). Propagation of interictal epileptiform activity can lead to erroneous source localizations: a 128-channel EEG mapping study. *J Clin Neurophysiol*, 20, 311-319.

Law, S.K. and Nunez, P.L. (1991). Quantitative representation of the upper surface of the human head. *Brain Topogr*, 3, 365-371.

Law, S.K. (1993). Thickness and resistivity variations over the upper surface of the human skull. *Brain Topogr*, 6, 99-109.

Law, S.K., Nunez, P.L., and Wijesinghe, R. (1993). High-resolution EEG using spline generated surface Laplacians on spherical and ellipsoidal surfaces. *IEEE Trans Biomed Eng*, 40, 145-153.

Le, J. and Gevins, A. (1993). Method to reduce blur distortion from EEG's using a realistic head model. *IEEE Trans Biomed Eng*, 40, 517-528

Le, J., Menon, V., and Gevins, A. (1994). Local estimate of surface Laplacian derivation on a realistically shaped scalp surface and its performance on noisy data. *Electroenceph Clin Neurophysiol*, 92, 433-441.

Leahy, R., Mosher, J., Spencer, M., Huang, M., and Lewine, J. (1998). A study of dipole localization accuracy for MEG and EEG using a human skull phantom. *Electroenceph Clin Neurophysiol*, 107, 159-173.

Lehmann, D. (1987). Principles of spatial analysis. In: Gevins, A.S. and Remond, A., eds. *Methods of analysis of brain electrical and magnetic signals. EEG handbook.* Amsterdam: Elsevier, 309-354.

Lemieux, L. and Leduc, A. (1992). Equivalent source estimation based on the calculation of the electric field from depth EEG data. *IEEE Trans Biomed Eng*, 39, 805-817

Lemieux, L., McBride, A., and Hand, J. (1996). Calculation of electrical potentials on the surface of a realistic head model by finite differences. *Phys Med Biol*, 41, 1079-1091.

Lin, W., Kuppusamy, K., Haacke, E.M., and Burton, H. (1996). Functional MRI in human somatosensory cortex activated by touching textured surfaces. *J Magn Reson Imag*, 6, 565-572.

Lopes da Silva, F.H. (2004). Event-related potentials: Methodology and quantification. In: Niedermeyer, E. and Lopes da Silva, F.H., eds. *Electroencephalography: Basic Principles, Clinical Applications and Related Fields*. Baltimore: Lippincott Williams & Wilkins, 991-1002.

Lüders, H., Dinner, D.S., Lesser, R.P., and Morris, H.H. (1986). Evoked potentials in cortical localization. *J Clin Neurophysiol*, 3, 75-84.

Lütkenhöner, B. (1998). Dipole source localization by means of maximum likelihood estimation I. Theory and simulations. *Electroenceph Clin Neurophysiol*, 106, 314-321.

Lynn, M.S. and Timlake, W.P. (1968). The use of multiple deflations in the numerical solution of singular systems of equations, with applications to potential theory. *SIAM J Numer Anal*, 5, 303-322.

Malmivuo, J. and Plonsey, R. (1995). *Bioelectromagnetism. Principles and Applications of Bioelectric and Biomagnetic Fields*. New York: Oxford University Press.

Malmivuo, J., Suihko, V., and Eskola, H. (1997). Sensitivity distributions of EEG and MEG measurements [published erratum appears in *IEEE Trans Biomed Eng*, 44, 430]. *IEEE Trans Biomed Eng*, 44, 196-208.

Marin, G., Guerin, C., Baillet, S., Garnero, L., and Meunier, G. (1998). Influence of skull anisotropy for the forward and inverse problem in EEG: simulation studies using FEM on realistic head models. *Hum Brain Mapp*, 6, 250-269.

Marquardt, D.W. (1963). An algorithm for least-squares estimation of non-linear parameters. *J Soc Ind Appl Math*, 11, 431-441.

Mauguière, F., Allison, T., Babiloni, C., Buchner, H., Eisen, A.A., Goodin, D.S., Jones, S.J., Kakigi, R., Matsuoka, S., Nuwer, M., Rossini, P.M., and Shibasaki, H. (1999). Somatosensory Evoked Potentials. In: Deuschl, G. and Eisen, A., eds. *Recommendations for the practice of clinical neurophysiology: Guidelines of the International Federation of Clinical Physiology (EEG Suppl)*. Amsterdam: Elsevier Science BV, 52, 79-90.

Mauguière, F. (2005). Somatosensory evoked potentials: normal responses, abnormal waveforms, and clinical applications in neurological diseases. In: Niedermeyer, E. and Lopes da Silva, F.H., eds. *Electroencephalography: basic principles, clinical applications, and related fields*. Philadelphia: Lippincott, Williams & Wilkins, 1067-1120.

Meijs, J.W.H. and Peters, M. (1987). The EEG and MEG, using a model of eccentric spheres to describe the head. *IEEE Trans Biomed Eng*, 34, 913-920.

Meijs, J.W.H., Boom, H., Peters, M., and van Oosterom, A. (1987). Application of the Richardson extrapolation in simulation studies of EEGs. *Med Biol Eng Comput*, 25, 222-226.

Meijs, J.W.H., Weier, O.W., Peters, M.J., and van Oosterom, A. (1989). On the numerical accuracy of the boundary element method. *IEEE Trans Biomed Eng*, 36, 1038-1049.

Merlet, I. and Gotman, J. (1999). Reliability of dipole models of epileptic spikes. *Clin Neurophysiol*, 110, 1013-1028.

Merlet, I. and Gotman, J. (2001). Dipole modeling of scalp electroencephalogram epileptic discharges: correlation with intracerebral fields. *Clin Neurophysiol*, 112, 414-430.

Michel, C., Grave de Peralta, R., Lantz, G., Gonzalez Andino, S., Spinelli, L., Blanke, O., Landis, T., and Seeck, M. (1999). Spatiotemporal EEG analysis and distributed source estimation in presurgical epilepsy evaluation. *J Clin Neurophysiol*, 16, 239-266.

Mine, S., Oka, N., Yamaura, A., and Nakajima, Y. (1998). Presurgical functional localization of primary somatosensory cortex by dipole tracing method of scalp-skull-brain head model applied to somatosensory evoked potential. *Electroenceph Clin Neurophysiol*, 108, 226-233.

Mosher, J.C., Lewis, P.S., and Leahy, R.M. (1992). Multiple dipole modeling and localization from spatio-temporal MEG data. *IEEE Trans Biomed Eng*, 39, 541-557.

Mosher, J.C., Spencer, M., Leahy, R., and Lewis, P. (1993). Error bounds for EEG and MEG dipole source localization. *Electroenceph Clin Neurophysiol*, 86, 303-321.

Mosher, J.C. and Leahy, R. (1998). Recursive MUSIC: a framework for EEG and MEG source localization. *IEEE Trans Biomed Eng*, 45, 1342-1354.

Mosher, J.C., Baillet, S., and Leahy, R.M. (1999a). EEG source localization and imaging using multiple signal classification approaches. *J Clin Neurophysiol*, 16, 225-238.

Mosher, J.C., Leahy, R.M., and Lewis, P.S. (1999b). EEG and MEG: Forward solutions for inverse methods. *IEEE Trans Biomed Eng*, 46, 245-259.

Musha, T. and Okamoto, Y. (1999). Forward and inverse problems of EEG dipole localization. *Crit Rev Biomed Eng*, 27, 189-239.

Nakamura, A., Yamada, T., Goto, A., Kato, T., Ito, K., Abe, Y., Kachi, T., and Kakig, R. (1998). Somatosensory homunculus as drawn by MEG. *Neuroimage*, 7, 377-386.

Nelder, J.A. and Mead, R. (1965). A simplex method for function minimization. *Comp J*, 7, 308-313.

Nicolas, P. and Deloche, G. (1976). Convolution computer processing of the brain electrical image transmission. *Int J Bio-Med Comput*, 7, 143-159.

Niedermeyer, E. (1996). Dipole theory and electroencephalography. *Clin Electroenceph*, 27, 121-131.

Nishijo, H., Hayashi, N., Fukuda, M., Endo, S., Musha, T., and Ono, T. (1994). Localization of dipole by boundary element method in three dimensional reconstructed monkey brain. *Brain Res Bull*, 33, 225-230.

Nunez, P.L. (1981). *Electric Fields of the Brain: The Neurophysics of EEG*. New York: Oxford University Press.

Nunez, P.L. (1987). A method to estimate local skull resistance in living subjects. *IEEE Trans Biomed Eng*, 34, 902-904.

Nunez, P.L. (1990). Localization of brain activity with electroencephalography. In: Sato, S. ed. *Magnetoencephalography. Advances in Neurology*. New York: Raven Press, 54, 39-65.

Nunez, P.L. and Pilgreen, K. (1991). The spline-Laplacianin clinical neurophysiology: a method to improve EEG spatial resolution. *J Clin Neurophysiol*, 8, 397-413.

Nunez, P.L. (1995). *Neocortical Dynamics and Human EEG Rhythms*. New York: Oxford University Press.

Nuwer, M. (1998). Fundamentals of evoked potentials and common clinical applications today. *J Clin Neurophysiol*, 106, 142-148.

Nyberg, G., Andersson, J., Antoni, G., Lilja, A., Pellettieri, L., Valind, S., and Långström, B. (1996). Activation PET scanning in pretreatment evaluation of patients with cerebral tumours or vascular lesions in or close to the sensorimotor cortex. *Acta Neurochir*, 138, 684-694.

Ollikainen, J., Vauhkonen, M., Karjalainen, P., and Kaipio, J. (1999). Effects of local skull inhomogeneities on EEG source estimation. *Med Eng Phys*, 21, 143-154.

Oostendorp, T. and van Oosetrom, A. (1989). Source parameter estimation in inhomogeneous volume conductors of arbitrary shape. *IEEE Trans Biomed Eng*, 36, 382-391.

Oostendorp, T.F. and van Oosterom, A. (1991). The potential distribution generation by surface electrodes in inhomogeneous volume conductors of arbitrary shape. *IEEE Trans Biomed Eng*, 38, 409-417.

Oostendorp, T.F., Delbeke, J., and Stegeman, D.F. (2000). The conductivity of the human skull: Results of in vivo and in vitro measurements. *IEEE Trans Biomed Eng*, 47, 1487-1492.

Pascual-Marqui, R.D., Michel, C., and Lehmann, D. (1994). Low resolution electromagnetic tomography: a new method for localizing electrical activity in the brain. *Int J Psychophys*, 18, 49-65.

Pascual-Marqui, R.D. (1999). Review of methods for solving the EEG inverse problem. *Int J Bioelectromag*, 1, 75-86.

Penfield, W. and Boldrey, E. (1937). Somatic motor and sensory representation in the cerebral cortex of man as studied by electrical stimulation. *Brain*, 60, 389-443.

Perrin, F., Pernier, J., Bertrand, O., Giard, M., and Echallier, J. (1987). Mapping of scalp potentials by surface spline interpolation. *Electroenceph Clin Neurophysiol*, 66, 75-81.

Peters, M.J., Stinstra, J.G., and Leveles, I. (2004). The electrical conductivity of living tissue: a parameter in the bioelectrical inverse problem. In: He, B., ed. *Modeling and Imaging of Bioelectrical Activity – Principles and Applications*. New York: Kluwer Academic/Plenum Publishers, Chap. 9.

Phillips, J., Leahy, R., Mosher, J., and Timsari, B. (1997). Imaging neural activity using MEG and EEG. *IEEE Eng Med Biol Mag*, 16, 34-42.

Pittau, F., Levan, P., Moeller, F., Gholipour, T., Hægelen, C., Zelmann, R., Dubeau, F., and Gotman J. (2011). Changes preceding interictal epileptic EEG abnormalities: comparison between EEG/fMRI and intracerebral EEG. *Epilepsia*, 52, 1120-1129.

Plonsey, R. (1969). *Bioelectric Phenomena*. New York: McGraw-Hill, Chap. 5.

Plonsey, R. (1995). Volume conductor theory. In: Bronzino, J.D., ed. *The Biomedical Engineering Handbook*. Florida: CRC Press, 201-212.

Plummer, C., Harvey, A.S., and Cook, M.J. (2008). EEG source localization in focal epilepsy: where are we now? *Epilepsia*, 49, 201-218.

Plummer, C., Wagner, M., Fuchs, M., Harvey, A.S., and Cook, M.J. (2010). Dipole versus distributed EEG source localization for single versus averaged spikes in focal epilepsy. *J Clin Neurophysiol*, 27, 141-162.

Pohlmeier, R., Buchner, H., Knoll, G., Rienacker, A., Beckmann, R., and Pesch, J. (1997). The influence of skull-conductivity misspecification on inverse source localization in realistically shaped finite element head models. *Brain Topogr*, 9, 157-162.

Press, W.H., Teukolsky, S.A., Vetterling, W.T., and Flannery, B.P. (1992). *Numerical Recipes in Fortran*. 2nd ed., New York: Cambridge University Press, Chap. 10.

Puce, A., Constable, R.T., Luby, M.L., McCarthy, G., Nobre, A.C., Spencer, D.D., Gore, J.C., and Allison, T. (1995). Functional magnetic resonance imaging of sensory and motor cortex: comparison with electrophysiological localization. *J Neurosurg*, 83, 262-270.

Pujol, J., Conesa, G., Deus, J., Vendrell, P., Isamat, F., Zannoli, G., Martí-Vilalta, J.L., and Capdevila, A. (1996). Presurgical identification of the primary sensorimotor cortex by functional magnetic resonance imaging. *J Neurosurg*, 84, 7-13.

Pullan, A. (1996). A high-order coupled finite element/boundary element torso model. *IEEE Trans Biomed Eng*, 43, 292-298.

Radich, B. and Buckley, K. (1995). EEG dipole localization bounds and MAP algorithms for head models with parameter uncertainties. *IEEE Trans Biomed Eng*, 42, 233-241.

Rao, S.M., Binder, J.R., Hammeke, T.A., Bandettini, P.A., Bobholz, J.A., Frost, J.A., Mykelbust, B.M., Jacobson, R.D., and Hyde, J.S. (1995). Somatotopic mapping of the human primary motor cortex with functional magnetic resonance imaging. *Neurology*, 45, 919-924.

Raz, J., Biggins, C., Turetsky, B., and Fein, G. (1993). Frequency domain dipole localization: extensions of the method and applications to auditory and visual evoked potentials. *IEEE Trans Biomed Eng*, 40, 909-918.

Richards, J.E. (2004). Recovering dipole sources from scalp-recorded event-related-potentials using component analysis: principal component analysis and independent component analysis. *Int J Psychophysiol*, 54, 201-220.

Riera, J.J. and Fuentes, M.E. (1998). Electric lead field for a piecewise homogeneous volume conductor model of the head. *IEEE Trans Biomed Eng*, 45, 746-753.

Robillard, P.N. and Poussart, Y. (1977). Specific-impedance measurements of brain tissues. *Med Biol Eng Comput*, 15, 438-445.

Rojo, P., Caicoya, A.G., Martin-Loeches, M., Sola, R.G., and Pozo, M.A. (2001). Localization of the epileptogenic zone by analysis of electroencephalographic dipole. *Rev Neurol*, 32, 315-320.

Rose, S. and Ebersole, J.S. (2009). Advances in spike localization with EEG dipole modeling. *Clin EEG Neurosci*, 40, 281-287.

Rosell, J., Colominas, J., Riu, P., Pallas-Areny, R., and Webster, J.G. (1988). Skin Impedance From 1 Hz to 1 MHz. *IEEE Trans Biomed Eng*, 35, 649-651.

Rosenfeld, M., Tanami, R., and Abboud, S. (1996). Numerical solution of the potential due to dipole sources in volume conductors with arbitrary geometry and conductivity. *IEEE Trans Biomed Eng*, 43, 679-689.

Roth, B., Balish, M., Gorbach, A., and Sam, S. (1993). How well does a three-sphere model predict positions of dipoles in a realistically shaped head? *Electroenceph Clin Neurophysiol*, 87, 175-184.

Rush, S. and Driscoll, D.A. (1968). Current distribution in the brain from surface electrodes. *Anesth Analg*, 47, 717-723.

Rush, S. and Driscoll, D.A. (1969). EEG electrode sensitivity – an application of reciprocity. *IEEE Trans Biomed Eng*, 16, 15-22.

Russell, G., Srinivasan, R., and Tucker, D. (1998). Bayesian estimates of error bounds for EEG source imaging [letter]. *IEEE Trans Biomed Eng*, 17, 1084-1089.

Sakai, K., Watanabe, E., Onodera, Y., Itagaki, H., Yamamoto, E., Koizumi, H., and Miyashita, Y. (1995). Functional mapping of the human somatosensory cortex with echo-planar MRI. *Magn Reson Med*, 33, 736-743.

Saleheen, H. and Ng, K. (1997). New finite difference formulations for general inhomogeneous anisotropic bioelectric problems. *IEEE Trans Biomed Eng*, 44, 800-809.

Salu, Y., Cohen, L.G., Rose, D., Sxato, S., Kufta, C., and Hallett, M. (1990). An improved method for localizing electric brain dipoles. *IEEE Trans Biomed Eng*, 37, 699-705.

Sarvas, J. (1987). Basic mathematical and electromagnetic concepts of the biomagnetic inverse problem. *Phys Med Bio*, 32, 11-22.

Scheler, G., Fischer, M.J., Genow, A., Hummel, C., Rampp, S., Paulini, A., Hopfengärtner, R., Kaltenhäuser, M., and Stefan, H. (2007). Spatial relationship of source localizations in patients with focal epilepsy: Comparison of MEG and EEG with a three spherical shells and a boundary element volume conductor model. *Hum Brain Mapp*. 28, 315-322.

Scherg, M. and Van Cramon, D. (1985a). Two bilateral sources of the late AEP as identified by a spatio-temporal dipole model. *Electroenceph Clin Neurophysiol*, 62, 32-34.

Scherg, M. and Van Cramon, D. (1985b). A new interpretation of the generators of BAEP waves I-V: Results of spatio-temporal dipole model. *Electroenceph Clin Neurophysiol*, 62, 290-299.

Scherg, M. and Van Cramon, D. (1986). Evoked dipole source potentials of the human auditory cortex. *Electroenceph Clin Neurophysiol*, 65, 344-360.

Scherg, M. and Berg, P. (1991). Use of prior knowledge in brain electromagnetic source analysis. *Brain Topogr*, 4, 143-150.

Scherg, M. and Picton, T. (1991). Separation and identification of event-related potential components by brain electric source analysis. *Electroenceph Clin Neurophysiol*, 42, 24-37.

Scherg, M. (1992). Functional imaging and localization of electromagnetic brain activity. *Brain Topogr*, 5, 103-111.

Scherg, M. and Ebersole, J. (1993). Models of brain sources. *Brain Topogr*, 5, 419-423.

Scherg, M. (1994). From EEG source localization to source imaging. *Acta Neuro Scand*, 152, 29-30.

Scherg, M. and Ebersole, J. (1994). Brain source imaging of focal and multifocal epileptiform EEG activity. *Neurophysiologie Clinique*, 24, 51-60.

Scherg, M., Bast, T., and Berg, P. (1999). Multiple source analysis of interictal spikes: goals, requirements, and clinical value. *J Clin Neurophysiol*, 16, 214-224.

Schlitt, H.A., Heller, L., Aaron, R., Best, E., and Ranken, D.M. (1995). Evaluation of boundary element methods for the EEG forward problem: Effect of linear interpolation. *IEEE Trans Biomed Eng*, 42, 52-58.

Schneider, M.R. (1972). A multistage process for computing virtual dipolar sources of EEG discharges from surface information. *IEEE Trans Biomed Eng*, 19, 1-12.

Schneider, M.R. (1974). Effect of inhomogeneities on surface signals coming from a cerebral current-dipole source. *IEEE Trans Biomed Eng*, 21, 52-54.

Scholz, B. and Schwierz, G. (1994). Probability-based current dipole localization from biomagnetic fields. *IEEE Trans Biomed Eng*, 41, 735-742.

Schwartz, D., Badier, J., Bihoué, P., and Bouliou, A. (1999). Evaluation of a new MEG-EEG spatio-temporal localization approach using a realistic source model. *Brain Topogr*, 11, 279-289.

Sepulveda, N., Walker, C., and Heath, R. (1983). Finite element analysis of current pathways with implanted electrodes. *J Biomed Eng*, 5, 41-48.

Sharbrough, F., Chatrian, G.-E., Lesser, R., Lüders, H., Nuwer, M., and Picton, T. (1991). American Electroencephalographic Society guidelines for standard electrode position nomenclature. *J Clin Neurophysiol*, 8, 200-202.

Shibata, N., Kubota, F., Machiyama, Y., Takahashi, A., and Miyamoto, K. (1998). Mapping of epileptic foci by the dipole tracing method in a brain tumor patient with olfactory seizures: comparison with intraoperative electrocorticograms. *Clin Electroencephal*, 29, 91-95.

Shin, C. (2000). Neurophysiological basis of functional neuroimaging: animal studies. *J Clin Neurophysiol*, 17, 2-9.

Sidman, R. (1991). A method for simulating intracerebral potential fields: the cortical imaging technique. *J Clin Neurophysiol*, 8, 432-441.

Silva C., Almeida, R, Oostendorp, T., Ducla-Soares, E., Foreid, J.P., and Pimentel, T. (1999). Interictal spike localization using a standard realistic head model: simulations and analysis of clinical data. *Clin Neurophysiol*, 110, 846-855.

Simpson, G., Pflieger, M., Foxe, J., Ahlfors, S., Vaughan, H., Hrabe, J, Ilmoniemi, R., and Lantos, G. (1995). Dynamic neuroimaging of brain function. *J Clin Neurophysiol*, 12, 432-449.

Sipilä, O., Nikkinen, P., Savolainen, S., Granström, M.-L., Gaily, E., Poutanen, V.-P., Pohjonen, H., and Liewendahl, K. (2000). Transmission imaging for registration of ictal and interictal SPECT, MRI, and EEG. *Eur J Nucl Med*, 27, 202-205.

Smith, D.B., Sidman, R.D., Flanigin, H., Henke, J., and Labiner, D. (1985). A reliable method for localizing deep intracranial sources of the EEG. *Neurology*, 35, 1702-1707.

Snyder, A. (1991). Dipole source localization in the study of EP generators: a critique. *Electroenceph Clin Neurophysiol*, 80, 321-325.

Sobel, D.F., Gallen, C.C., Schwartz, B.J., Waltz, T.A., Copeland, B., Yamada, S., Hirschkoff, E.C., and Bloom, F.E. (1993). Locating the central sulcus: comparison of MR anatomic and magnetoencephalographic functional methods. *Am J Neuroradiol*, 14, 915-927.

Soong, A. and Koles, Z. (1995). Principal-component localization of the sources of the background EEG. *IEEE Trans Biomed Eng*, 42, 59-67.

Spitzer, A.R., Cohen, L.G., Fabrikant, J., and Hallet, M. (1989). A method for determining optimal interelectrode spacing for cerebral topographic mapping. *Electroenceph Clin Neurophysiol*, 72, 355-361.

Srebro, R., Oguz, R., Hughlett, K., and Purdy, P. (1993). Functional brain imaging: dipole localization and Laplacian methods. *Vis Res*, 33, 2413-2419.

Srebro, R. and Oguz, R. (1997). Estimating cortical activity from VEPS with the shrinking ellipsoid inverse. *Electroenceph Clin Neurophysiol*, 102, 343-355.

Stinstra, J. and Peters, M. (1998). The volume conductor may act as a temporal filter on the ECG and EEG. *Med Biol Eng Comput*, 36, 711-716.

Stok, C. (1987). The influence of model parameters obn EEG/MEG single dipole source estimation. *IEEE Trans Biomed Eng*, 34, 289-296.

Stok, C. and Wognum, P. (1988). A noniterative approximate solution method for volume conductor problems based on the finite difference method. *IEEE Trans Biomed Eng*, 35, 31-35.

Suihko, V. (1998). Modeling direct activation of corticospinal axons using transcranial electrical stimulation. *Electroenceph Clin Neurophysiol*, 109, 238-244.

Suk, J., Ribary, U., Camppell, J., Yamamoto, T., and Llinás, R. (1991). Anatomical localization revealed by MEG recordings of the human somatosensory system. *Electroenceph Clin Neurophysiol*, 78, 185-196.

Suzuki, A. and Yasui, N. (1992). Intraoperative localization of the central sulcus by cortical somatosensory evoked potentials in brain tumor. *J Neurosurg*, 76, 867-870.

Tan, S., Roth, B., and Wikswo, J. (1990). The magnetic field of cortical current sources: the application of a spatial filtering model to the forward and inverse problems. *Electroenceph Clin Neurophysiol*, 76, 73-85.

Tao, J.X., Ray, A., Hawes-Ebersole, S., and Ebersole, J.S. (2005). Intracranial EEG substrates of scalp EEG interictal spikes. *Epilepsia*, 46, 669-676.

Thevenet, M., Bertrand, O., Perrin, F., Dumont, T., and Pernier, J. (1991). The finite element method for a realistic head model of electrical brain activities: preliminary results. *Clin Phys Physiol Meas*, 12, 89-94.

Towle, V.L., Bolanos, J., Suarez, D., Tan, K., Grzeszcuk, R., Levin, D.N., Cakmur, R., Frank, S.A., and Spire, J.-P. (1993). The spatial location of EEG electrodes: locating the best-fitting sphere relative to cortical anatomy. *Electroenceph Clin Neurophysiol*, 86, 1-6.

Tseng, S., Chong, F., Chen, R., and Kuo, T. (1995). Source localization of averaged and single EEG spikes using the electric dipole model. *Med Eng Phys*, 17, 64-70.

Turetsky, B., Raz, J., and Fein, G. (1990). Representation of multi-channel evoked potential data using a dipole component model of intracranial generators: application to the auditory P300. *Electroenceph Clin Neurophysiol*, 76, 540-556.

Valeriani, M., Le Pera, D., and Tonali, P. (2001). Characterizing somatosensory evoked potential sources with dipole models: advantages and limitations. *Muscle Nerve*, 24, 325-339.

Van den Broek, S., Reinders, F., Donderwinkel, M., and Peters, M. (1998). Volume conduction effects in EEG and MEG. *Electroenceph Clin Neurophysiol*, 106, 522-534.

Van Oosterom, A. and Strackee, J. (1983). The solid angle of a plane triangle. *IEEE Trans Biomed Eng*, 30, 125-126.

Van Oosterom, A. (1991). History and evolution of methods for solving the inverse problem. *J Clin Neurophysiol*, 8, 371-380.

Vanrumste, B., Van Hoey, G., Van de Walle, R., D'Havé, M., Lemahieu, I., and Boon, P. (2000). Dipole location errors in electroencephalogram source analysis due to volume conductor model errors. *Med Biol Eng Comput*, 38, 528-534.

Vanrumste, B., Van Hoey, R., Van de Walle, R., D'Havé, M.R.P., Lemahieu, I.A., and Boon P.A.J.M. (2001). The validation of the finite difference method and reciprocity for solving the inverse problem in EEG dipole source analysis. *Brain Topogr*, 14, 83-92.

Vanrumste, B. (2001). EEG dipole source analysis in a realistic head model. *Ph.D. Dissertation*. Ghent University, Ghent, Belgium.

Van Veen, B., van Drongelen, W., Yuchtman, M., and Suzuki, A. (1997). Localization of brain electrical activity via linearly constrained minimum variance spatial filtering. *IEEE Trans on Biomed Eng*, 44, 867-880.

Wang, B., Toro, C., Zeffro, T., and Hallett, M. (1994). Head surface digitization and registration: a method for mapping positions on the head onto magnetic resonance images. *Brain Topogr*, 6, 185-192.

Wang, J., Williamson, S., and Kaufmann, L. (1992). Magnetic source images determined by a lead-field analysis: the unique minimum-norm least-squares estimation. *IEEE Trans Biomed Eng*, 39, 665-675.

Wang, G., Worrell, G., Yang, L., Wilke, C., and He, B. (2010). Interictal spike analysis of high-density EEG in patients with partial epilepsy. *Clin Neurophysiol*, 122, 1098-1105.

Wang, W. and Eisenberg, S. (1994). A three-dimensional finite element method for computing magnetically induced currents in tissues. *IEEE Trans Mag*, 30, 5015-5023.

Wang, Y. and He, B. (1998). A computer simulation study of cortical imaging from scalp potentials. *IEEE Trans Biomed Eng*, 45, 724-735.

Wang, Y., Berg, P., and Scherg, M. (1999). Common spatial subspace decomposition applied to analysis of brain responses under multiple task conditions: a simulation study. *Clin Neurophysiol*, 110, 604-614.

Weinstein, D., Zhukov, L., and Johnson, C. (2000). Lield-field bases for electroencephalography source imaging. *Ann Biomed Eng*, 28, 1059-1065.

Wieringa, H. and Peters, M. (1993). Processing MRI data for electromagnetic source imaging. *Med Biol Eng Comput*, 31, 600-606.

Wikswo, J., Gevins, A., and Williamson, S. (1993). The future of the EEG and MEG. *Electroenceph Clin Neurophysiol*, 87, 1-9.

Wischmann, H.-A., Drenckhahn, R., Wagner, M., and Fuchs, M. (1996). Systematic distribution of the auto solid angle and related integrals onto the adjacent triangles for the node based boundary element method. *Med Biol Eng Comput*, 34, 245-246.

Witwer, J., Trezek, G., and Jewett, D. (1972). The effect of media inhomogeneities upon intracranial electrical fields. *IEEE Trans Biomed Eng*, 19, 352-362.

Wood, C.C., Spencer, D.D., Allison, T., McCarthy, G., Williamson, P.D., and Goff, W.R. (1988). Localization of human sensorimotor cortex during surgery by cortical surface recording of somatosensory evoked potentials. *J Neurosurg*, 68, 99-111.

Woolsey, C.N., Erickson, T.C., and Gilson, W.E. (1979). Localization in somatic sensory and motor areas of human cerebral cortex as determined by direct recording of evoked potentials and electrical stimulation. *J Neurosurg*, 51, 476-506.

Yamazaki, T., van Dijk, B., and Spekreijse, H. (1998). The accuracy of modeling equivalent dipoles and the spatio-temporal correlations of background EEG. *IEEE Trans Biomed Eng*, 45, 1114-1121.

Yan, Y., Nunez, P., and Hart, R. (1991). Finite-element model of the human head: scalp potentials to dipole sources. *Med Biol Eng Comput*, 29, 475-481.

Yang, T.T., Gallen, C.C., Schwartz, B.J., and Bloom, F.E. (1988). Noninvasive somatosensory homunculus mapping in humans by using a large-array biomagnetometer. *Proc Natl Acad Sci USA*, 90, 3098-3102.

Yvert, B., Bertrand, O., Echallier, J., and Pernier, J. (1995). Improved forward EEG calculations using local mesh refinement of realistic head geometries. *Electroenceph Clin Neurophysiol*, 95, 381-392.

Yvert, B., Bertrand, O., Echallier, J., and Pernier, J. (1996). Improved dipole localization using local mesh refinement of realistic head geometries: an EEG simulation study. *Electroenceph Clin Neurophysiol*, 99, 79-89.

Yvert, B., Bertrand, Thévenet, M., O., Echallier, J., and Pernier, J. (1997). A systematic evaluation of the spherical model accuracy in EEG dipole localization. *Electroenceph Clin Neurophysiol*, 102, 452-459.

Yousry, T.A., Schmid, U.D., Alkadhi, H., Schmidt, D., Peraud, A., Buettner, A., and Winkler, P. (1997). Localization of the motor hand area to a knob on the precentral gyrus: a new landmark. *Brain*, 120, 141-157.

Zanow, F. and Peters, M. (1995). Individually shaped volume conductor models of the head in EEG source localization. *Med Biol Eng Comput*, 33, 582-588.

Zhang, Z. and D. Jewett, D.L. (1993). Insidious errors in dipole localization parameters at a single time-point due to model misspecification of number of shells. *Electroenceph Clin Neurophysiol*, 88, 1-11.

Zhang, Z., Jewett, D.L., and Goodwill, G. (1994). Insidious errors in dipole parameter due to shell model misspecification using multiple time-points. *Brain Topogr*, 6, 283-298.

Zhou, H. and van Ooosterom, A. (1992). Computation of the potential distribution in a four-layer anisotropic concentric spherical volume conductor. *IEEE Trans Biomed Eng*, 39, 154-158.